Electrochemical Energy Reviews (2022) 5:263–311
https://doi.org/10.1007/s41918-021-00098-3

REVIEW ARTICLE

Perovskite Cathode Materials for Low-Temperature Solid Oxide Fuel Cells: Fundamentals to Optimization

Zhiheng Li[1,2] · Mengran Li[1] · Zhonghua Zhu[1]

Received: 5 August 2020 / Revised: 13 October 2020 / Accepted: 12 December 2020 / Published online: 9 April 2021

Abstract

Acceleration of the oxygen reduction reaction at the cathode is paramount in the development of low-temperature solid oxide fuel cells. At low operating temperatures between 450 and 600 °C, the interactions between the surface and the bulk of the cathode materials greatly impact the electrode kinetics and consequently determine the overall efficacy and long-term stability of the fuel cells. This review will provide an overview of the recent progress in the understanding of surface-bulk interactions in perovskite oxides as well as their impact on cathode reactivity and stability. This review will also summarize current strategies in the development of cathode materials through bulk doping and surface functionalization. In addition, this review will highlight the roles of surface segregation in the mediation of surface and bulk interactions, which have profound impacts on the properties of cathode surfaces and the bulk and therefore overall cathode performance. Although trade-offs between reactivity and stability commonly exist in terms of catalyst design, opportunities also exist in attaining optimal cathode performance through the modulation of both cathode surfaces and bulk using combined strategies. This review will conclude with future research directions involving investigations into the role of oxygen vacancy and mobility in catalysis, the rational modulation of surface-bulk interactions and the use of advanced fabrication techniques, all of which can lead to optimized cathode performance.

Zhiheng Li, Mengran Li are made equal contributions to this review.

✉ Mengran Li
m.li6@uq.edu.au

✉ Zhonghua Zhu
z.zhu@uq.edu.au

[1] School of Chemical Engineering, The University of Queensland, Brisbane 4072, Australia

[2] School of Chemical Engineering, China University of Petroleum, Qingdao 266555, Shandong, China

Graphic Abstract

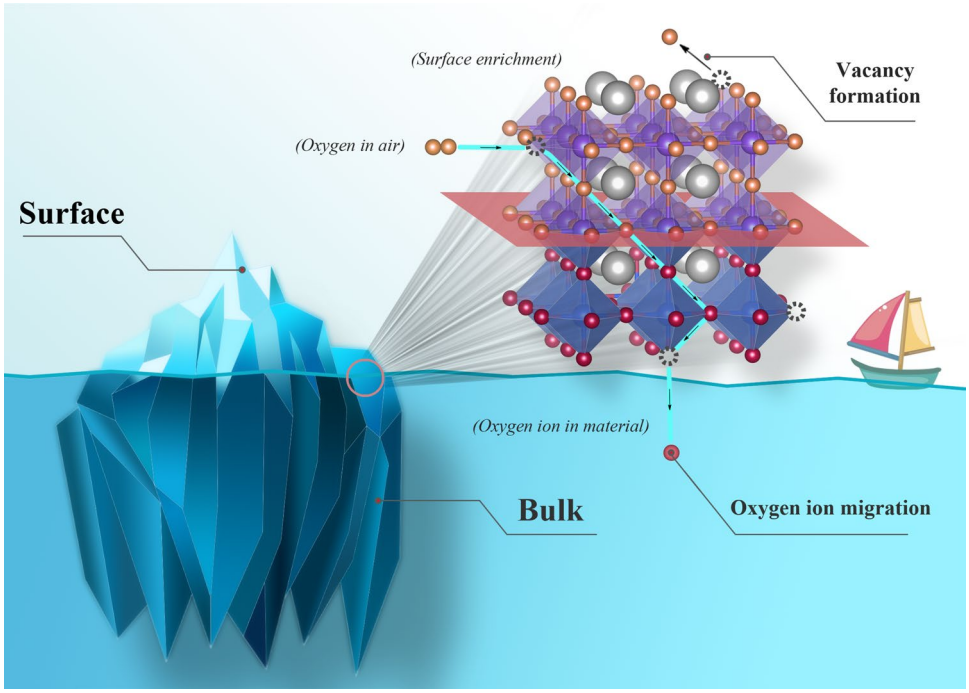

Keywords Oxygen reduction reaction · Solid oxide fuel cell · Perovskite · Cathode · Electrocatalysis

Abbreviations

BSCF	(Ba, Sr)(Co, Fe)$O_{3-\delta}$
LSC	(La, Sr)$CoO_{3-\delta}$
LSM	(La, Sr)MnO_3
LSCF	(La,Sr)(Co, Fe)$O_{3-\delta}$
ASR	Area-specific resistance
ALD	Atomic layer deposition
ABE	Average metal–oxygen energy
BZY	$BaZr_{0.8}Y_{0.2}O_{3-\delta}$
CAED	Chemically assisted electrodeposition
D_2O	Deuterium oxide
EDX	Energy-dispersive X-ray
ETEM	Environmental transmission electron microscopy
GDC	$Gd_{0.1}Ce_{0.9}O_{1.95}$
HAADF-STEM	High-angle annular dark-field scanning transmission electron microscopy
LAO	$LaAlO_3$
ORR	Oxygen reduction reaction
ABO_3	Perovskite oxides
PLD	Pulsed laser deposition
RP	Ruddlesden–Popper
SOFCs	Solid oxide fuel cells
SCT15	$SrCo_{0.85}Ta_{0.15}O_{3-\delta}$
SCNT	$SrCo_{0.8}Nb_{0.1}Ta_{0.1}O_{3-\delta}$
SCN20	$SrCo_{0.8}Nb_{0.2}O_{3-\delta}$
SCT20	$SrCo_{0.8}Ta_{0.2}O_{3-\delta}$
SSNC	$SrSc_{0.175}Nb_{0.025}Co_{0.8}O_{3-\delta}$
STO	$SrTiO_3$
TEM	Transmission electron microscopy
YSZ	Yttria-stabilized zirconia

1 Introduction

Solid oxide fuel cells (SOFCs) are emerging energy conversion devices that can transform chemical energy from various fuels such as hydrogen, ammonia [1] or hydrocarbons [2, 3] into electricity with high efficiency (i.e.,~60% alone and over 85% if combined with heat and power) [4, 5]. Corresponding high operating temperatures (450–1000 °C) also allow for the feasibility of internal fuel reforming inside fuel cells, thus providing SOFC technologies with unparalleled fuel flexibility as compared with other fuel cell technologies such as proton-exchange membrane fuel cells that normally demand strict fuel requirements [6].

Typical solid oxide fuel cells (Fig. 1) consist of three major components, including a cathode, an anode and an electrolyte. Here, the function of the cathode is to electrochemically reduce oxygen molecules into oxygen anions that

are subsequently transported through a dense electrolyte to oxidize fuels at the anode, resulting in the transfer of electrons from the anode to the cathode through an external circuit and do the electrical work along its way.

One significant challenge faced by SOFC technologies involves high operating temperatures that are generally above 800 °C. High operating temperatures lead to significant issues including (1) thermal expansion mismatch between cell components, (2) accelerated degradation of electrode and electrolyte materials and (3) limited material selection [7, 8], all of which degrade the overall cost-effectiveness of high-temperature fuel cell technologies. Thermal expansion mismatch can slow down start-up/shut-down procedures and lower fuel cell thermal-cycling stability. The accelerated material degradation is detrimental to long-term stability, which is a key prerequisite for mature electrochemical application. The limitation of the materials that can tolerate corresponding high temperatures directly translates to higher costs.

To address these challenges, reducing operating temperatures to between 450–600 °C hold promise while maintaining merits such as fuel flexibility and sufficient ion transport kinetics. However, low operating temperatures can also significantly decrease oxygen reduction reaction (ORR) kinetics and render conventional cathodes such as (La, Sr)MnO_3 (LSM) infeasible to catalyze ORR at acceptable rates. Conventional electrode materials for operating temperature above 800 °C are generally pure electronic conductors, which limit catalytically active sites for ORR to three-phase interfaces between the electronic conducting phase (e.g., LSM phase), the ionic conducting phase (e.g., electrolyte such as yttria-doped zirconia) and gaseous oxygen molecules. Therefore, the ORR catalysts at reduced temperature should possess both (1) high surface electrochemical activity toward ORR and (2) rapid oxygen-ion diffusion in the bulk, both of which will help extend the density of ORR active sites from the limited cathode/electrolyte interfaces throughout the cathode surface. Optimal cathodes at reduced temperatures should also possess high porosity and well-matched thermal expansion coefficients as well as good chemical compatibility with contacting components such as current collectors and electrolytes.

Based on these requirements, perovskite oxides (ABO_3) such as $Ba_{0.5}Sr_{0.5}Co_{0.8}Fe_{0.2}O_{3-\delta}$ [9], $PrBa_{0.5}Sr_{0.5}Co_{1.5}Fe_{0.5}O_{5+\delta}$ [10], $SrSc_{0.175}Nb_{0.025}Co_{0.8}O_{3-\delta}$ [11] and $SrCo_{0.8}Nb_{0.1}Ta_{0.1}O_{3-\delta}$ [12] are considered in recent decades to be promising cathode candidates for operation at reduced temperatures. This is because as compared with various simple metal oxides, perovskite oxides typically show much higher mixed ionic and electronic conductivities (MIECs) that can extend active sites throughout electrode surfaces. In addition, perovskite oxides can be combined with ionic conducting materials such as samarium-doped ceria to further improve structural stability and long-term stability [13]. Despite this, highly active perovskite oxides also present new challenges, including (1) the instability of corresponding crystal structures, (2) surface enrichment and (3) susceptibility to contaminants such as CO_2, SO_2 and Cr, all of which are predetermined by the interplay between the cathode bulk and surface [14–16]. The interactions between cathode bulk and surface become more significant at elevated temperatures, which are different from catalysis at room temperature in which cathode surfaces dominate ORR. Because of this, tremendous efforts have been devoted to investigate the interactions between cathode surfaces and bulk, their role in ORR catalysis, and modulation of bulk and surface properties to enhance cathode performance.

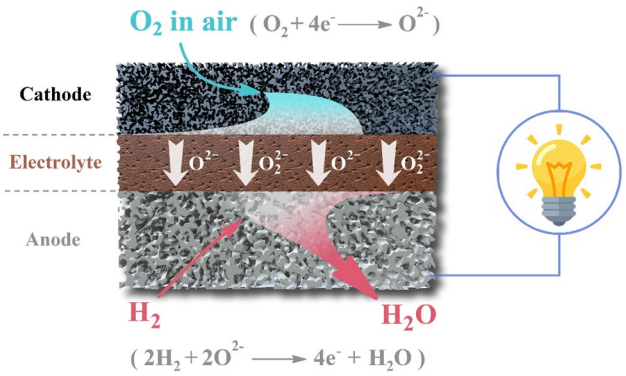

Fig. 1 Microstructural schematic of a typical solid oxide fuel cell with corresponding physical–chemical processes

This review attempts to summarize recent advancements in the understanding of mechanisms for surface-bulk interactions and ORR kinetics as well as strategies to modulate cathode bulk and surface to optimize cathode efficiency and stability. This review consists of two major sections. In Sect. 2–4, the review discusses the mechanisms underlying perovskite surface segregation, ORR kinetics and cathode susceptibility to contaminants. The strategies and approaches to tailor bulk and surface properties are summarized in Sect. 5. This review concludes with a brief summary of recent findings and provide perspective in the development of next-generation cathode materials for LT-SOFCs.

2 Surface and Bulk of Perovskite Oxides

The surface and bulk of perovskites are significantly different in composition in which the formation of perovskite surfaces can be considered to be a result of the cleavage of perovskite bulk at a specific direction. In addition, perovskite surface atoms usually possess lower coordination numbers (i.e., higher surface free energies) than bulk atoms, which will lead to the rearrangement of surface atoms and the

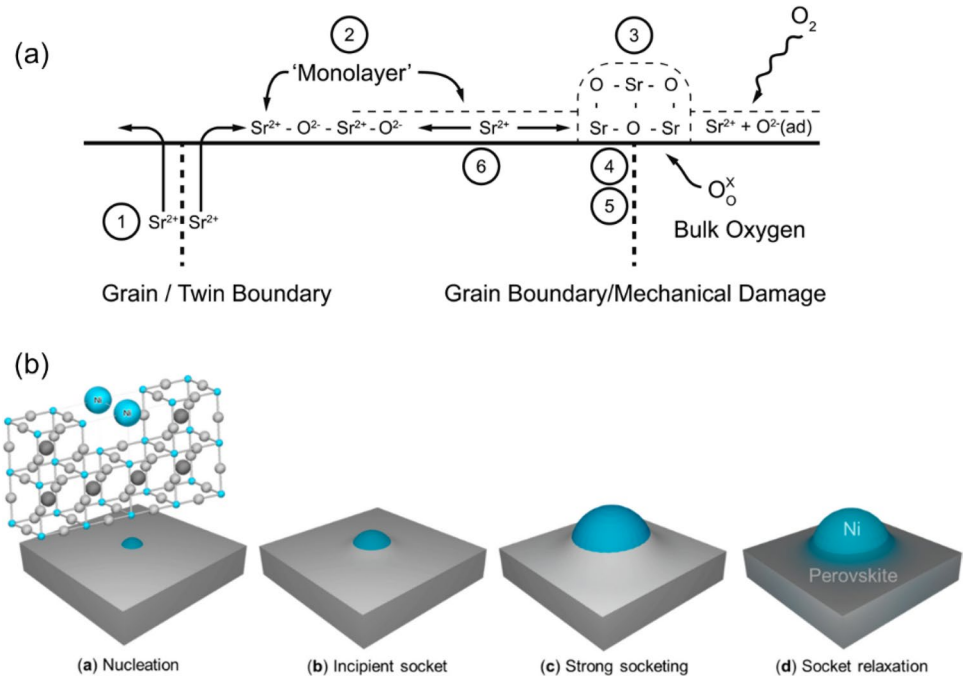

Fig. 2 Proposed mechanisms for **a** A-site cation Sr surface segregation, reproduced with permission from Ref. [30], Copyright 2018, Royal Society of Chemistry, and **b** B-site exsolution of Ni at the perovskite surface. Reproduced with permission from Ref. [32]. Copyright 2019, American Chemical Society

segregation of certain cations from the bulk to the surface [17]. These excess cations as a result of segregation from the bulk will subsequently precipitate onto perovskite surfaces in the form of oxide islands or cation-rich phases. As a result, these surface composition re-distribution and cation segregation processes can dynamically alter the composition and property of corresponding perovskite oxides, including surface and bulk composition [18, 19], surface microstructures [20], crystal structures [21], electrocatalysis-related properties (e.g., oxygen surface exchange kinetics [22, 23]), bulk diffusivities [24] as well as fuel reforming and oxidation [25–27].

Interactions between perovskite bulk and surface as facilitated by cation segregation are prominent at elevated temperatures. The ABO_3 perovskite oxides usually contain more than two cations (i.e., relatively large A cations and smaller B cations), and cation segregation can be categorized into A-site cation (e.g., Sr) segregation and B-site cation (e.g., Co, Ni, Fe) segregation (so-called exsolution). A-site cation segregation is a common phenomenon observed in perovskite oxide cathodes [17], whereas B-site cation exsolution is usually intentionally induced to form nanoparticles at the perovskite anode surface [14]. The former process occurs with relative ease at the top surface of materials and leave sub-surfaces enriched with B-site cations [28] but may not significantly affect the structural integrity and compositions of the bulk [29].

Figure 2a illustrates the mechanism of A-site cation (Sr) surface segregation from $La_{0.6}Sr_{0.4}Co_{0.2}Fe_{0.8}O_{3-\delta}$ perovskite oxide, as proposed by Niania et al. [30] based on results from in situ surface characterization. The exsolution normally occurs within the bulk, driven by reducing conditions, and has profound impacts on bulk crystal structure and composition [31]. Figure 2b provides an illustration of the exsolution of Ni from perovskite as proposed by Neagu et al. [32] based on their in situ observation of the Ni exsolution from $La_{0.43}Ca_{0.37}Ti_{0.94}Ni_{0.06}O_3$ being annealed at 900 °C under high vacuum. Based on these proposed mechanisms, it can be seen that both segregation processes are strongly correlated with (1) perovskite composition and structure, (2) external conditions such as temperature, gas composition and partial pressure, and electrical polarization [33]. The following subsections briefly summarize the various factors governing perovskite bulk-surface interactions.

2.1 Perovskite Composition and Crystal Structure

2.1.1 Cation Size

Perovskite oxides are known for high flexibility with various cation dopants at A- or B-sites. The size mismatch between hosts (e.g., La^{3+} with a Shannon ionic radius of 1.36 Å) [34] and dopants (e.g., Sr^{2+} with an ionic radius of 1.44 Å) can increase the elastic energy of lattices and constitutes the thermodynamic driving force of dopant migration from the bulk to the surface to minimize this elastic energy. Typical examples include alkaline-earth element (i.e., Sr^{2+} and Ba^{2+}) enrichment at the surface of many perovskite oxides such as LSM [35, 36], (La, Sr)$CoO_{3-\delta}$ (LSC) [20, 37] or (Sm, Sr)$CoO_{3-\delta}$ [38]. For example, Lee et al. [29] reported a strong correlation between cation surface segregation and the ionic size of alkaline-earth dopants such as Sr and Ba.

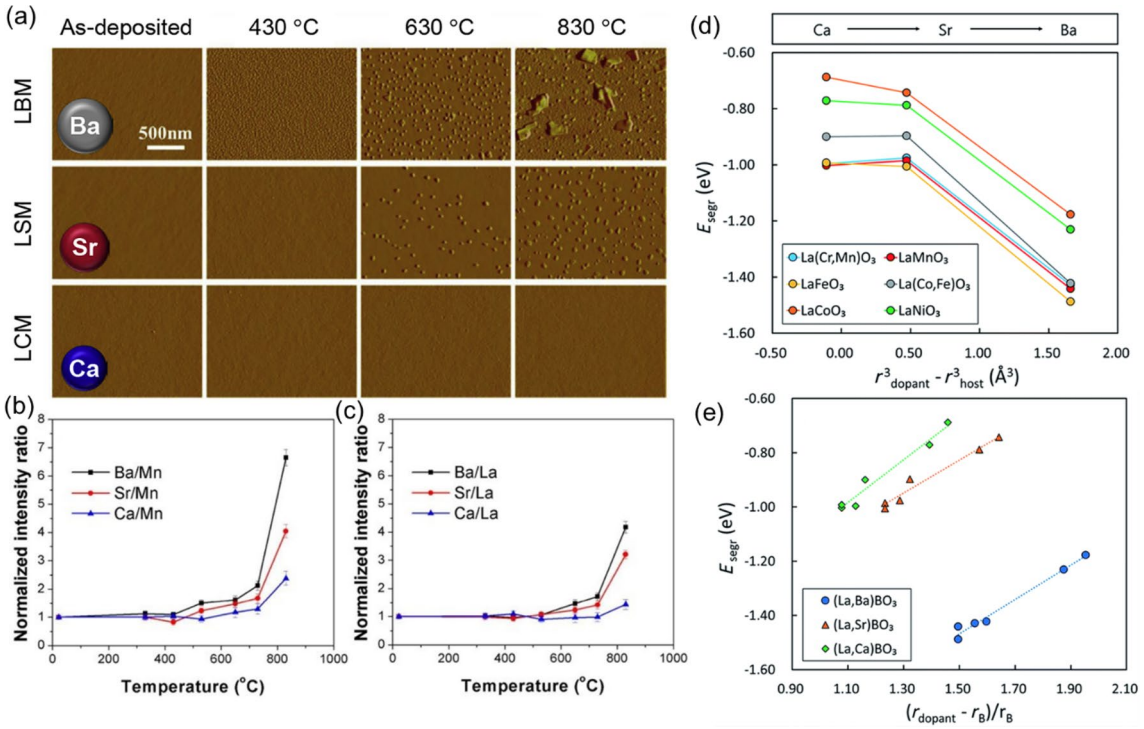

Fig. 3 **a** Atomic force microscopy images of Ca-, Sr- and Ba-doped $LaMnO_3$ (denoted as LCM, LSM and LBM, respectively) thin films at various temperatures in air for 1 h. **b** Normalized dopant/Mn and **c** dopant/La ratios obtained from angle-resolved X-ray photoelectron spectroscopy as a function of temperature. Reproduced with permission from Ref. [29]. Copyright 2013, American Chemical Society. **d** Surface segregation energy as a function of size mismatch between dopant/host at the A-site and **f** size mismatch between A-site dopants and B-site metals. Reproduced with permission from Ref. [39]. Copyright 2016, Royal Society of Chemistry

At elevated temperatures above 430 °C, as shown in Fig. 3a, the $LaMnO_3$ films doped with relatively larger dopants Ba (ionic radius = 1.61 Å) and Sr (ionic radius = 1.44 Å) than the host La (ionic radius = 1.36 Å) were roughened by the formation of small particles on the surface (Fig. 3a). These researchers also found that based on angle-resolved X-ray photoelectron spectroscopy dopant surface enrichment the extent of dopant segregation increased with dopant/host size mismatch level in the order of Ba > Sr > Ca (ionic size = 1.34 Å) (Fig. 3b, c). In another example, Kwon et al. [39] applied density functional theory (DFT) calculations to compare the dopant segregation energy of alkaline-earth element-doped $LaBO_3$ perovskite oxides with various B-site metals including $Cr_{0.5}Mn_{0.5}$, Mn, Fe and $Co_{0.25}Fe_{0.75}$. These researchers confirmed the essential role of A-site host/dopant size mismatching in driving dopant segregation (Fig. 3d, e), and

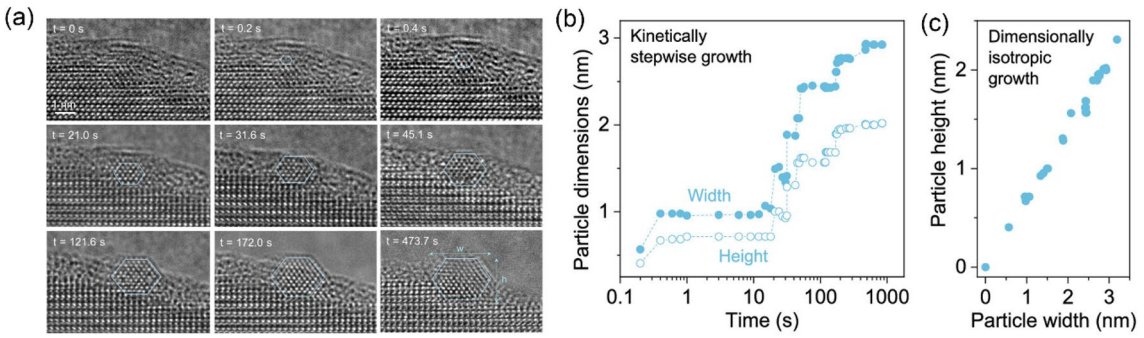

Fig. 4 **a** Time-resolved observations of Ni particle nucleation and growth under vacuum based on TEM at the surface of $La_{0.43}Ca_{0.37}Ti_{0.94}Ni_{0.06}O_3$ powder at 900 °C. **b** Plot of Ni particle width and height shown in (**a**) as a function of time and **c** plot of height versus width of the corresponding Ni particles. Reproduced with permission from Ref. [32]. Copyright 2019, American Chemical Society

also highlighted the role of the B-site cations in the dopant segregation process. They found that increasing B-site cation size can induce extra compressive strain in host lattices and therefore promote dopant segregation (Fig. 3e). Aside from alkaline-earth dopant segregation, our group also observed the more significant surface segregation of Li (0.92 Å) and K (1.64 Å) over $SrFe_{0.8}Nb_{0.1}Ta_{0.1}O_{3-\delta}$ perovskite oxide as compared with Na (1.39 Å) as partially contributed by size mismatch between the Sr host (1.44 Å) and the alkali dopants [18].

Kinetically, large-sized dopants such as Sr, Ba or K can slow down diffusion rates from bulk to surface. For example, Lee et al. [29] performed nudged elastic band calculations for the migration of alkaline-earth metals in doped $LaMnO_3$ and $SmMnO_3$ models and reported increased energy barriers for dopant diffusion with dopant size. A high energy barrier for cation diffusion indicates slow segregation kinetics. This effect is particularly prominent for alkali metal dopants if annealing durations were short. Although the extent of the K/Sr size mismatch is more significant than Li/Sr size mismatch [18], (Sr, Li/K) $Fe_{0.8}Nb_{0.1}Ta_{0.1}O_{3-\delta}$ surfaces were much more easily enriched with Li species (Li/Fe ratio = ~7) than with K species (K/Fe ratio < 1).

2.1.2 Stoichiometry

The stoichiometry of cations and anions in perovskite oxides is another critical factor that can affect the interactions between perovskite bulk and surface. By lowering the stoichiometry of relatively large A-site cations, the elastic energy of lattices can be relieved and thus weaken the driving force for A-site cation segregation from bulk to surface. This has commonly been observed in A-site-deficient $(La, Sr)_{1-x}MnO_3$ oxides [40–42]. For example, Pang et al. [43] very recently developed an A-site-deficient $La_{0.5}Ba_{0.5-x}CoO_{3-\delta}$ ($x = 0$ and 0.025) and reported that Ba deficiency can significantly suppress A-site metal surface segregation, which these researchers attributed to relaxed lattice strain due to the absence of large-sized Ba. On the other hand, materials with excess A-site dopants such as Ruddlesden–Popper (RP) structured $A_{n+1}B_nO_{3n+1}$ can result in A-site metal-rich surfaces after annealing in oxidizing environments and can commonly be observed in RP metal oxides such as $Sr_{n+1}Ti_nO_{3n+1}$ [44], $(La, Sr)_{n+1}(Co, Fe)_nO_{3n+1}$[45] and $La_{n+1}Ni_nO_{3n+1}$ [46].

The introduction of deficiencies (i.e., non-stoichiometry) at A-sites can also serve as a driving force to encourage the exsolution of B-site cations from bulk to surface to revert "defect-abundant" perovskite oxides to "defect-free" oxides [31]. These exsolution processes require reducing conditions however. For example, Neagu et al. [32] recently applied environmental transmission electron microscope (ETEM) to in situ observe the exsolution of Ni nanoparticles at the surface of A-site-deficient $La_{0.43}Ca_{0.37}Ti_{0.94}Ni_{0.06}O_3$ oxide under vacuum at 900 °C (Fig. 4a) in which further analysis of Ni particle height and width from these snapshots revealed that exsolved Ni nanoparticles grew in a stepwise and isotropic manner (Fig. 4b, c).

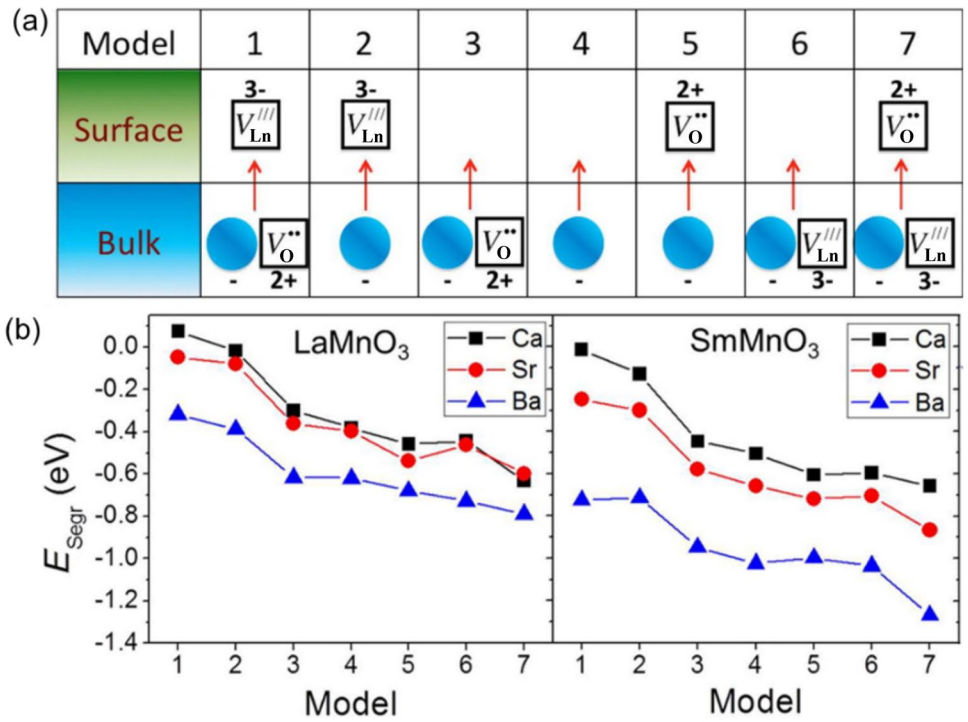

Fig. 5 **a** Schematics of models based on $LaMnO_3$ or $SmMnO_3$ doped with alkaline-earth elements (denoted as blue spheres) with strengthened electrostatic dopant attraction correlating to model number from 1 to 7. **b** Comparison of calculated segregation energy of doped $LaMnO_3$ or $SmMnO_3$ for the seven models described in (**a**). Reproduced with permission from Ref. [29]. Copyright 2013, American Chemical Society

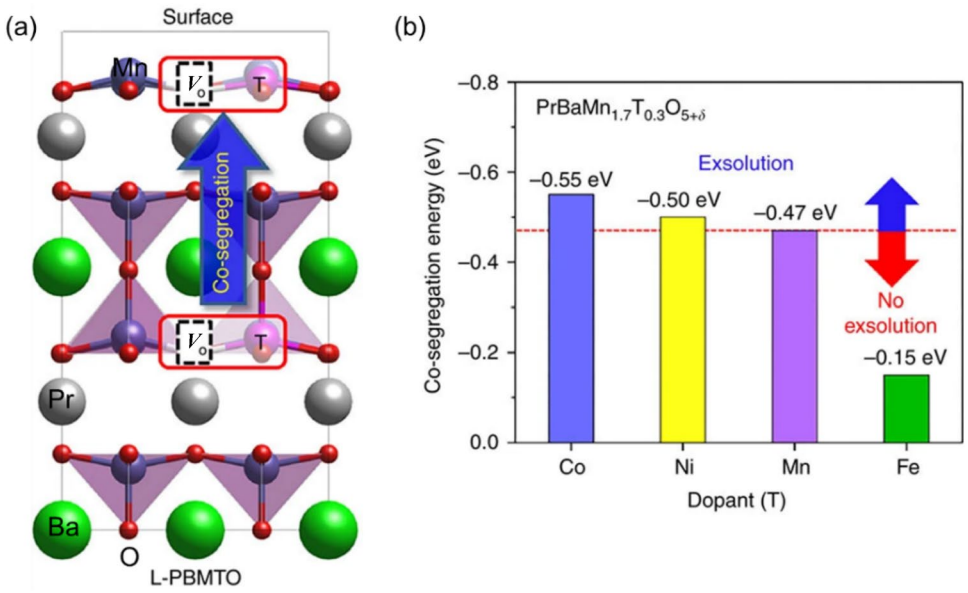

Fig. 6 **a** Schematic of layered perovskite $PrBaMn_2O_{5+\delta}$ model doped with transition metals (denoted as T) including Co, Ni, Mn and Fe. **b** Comparison of co-segregation energy between different transition metal dopants. Reproduced with permission from Ref. [25]. Copyright 2017, Nature Publishing Group

Surface oxygen vacancies can also cause surface cation rearrangement as driven by electrostatic interactions [47]. For example, Lee et al. [29] investigated seven scenarios (Fig. 5a) with varying strength of electrostatic interactions related to $LaMnO_3$ and $SmMnO_3$ doped with divalent alkaline-earth elements at the A-site. Their DFT results revealed easy divalent dopant segregation (low energy for cation segregation) for models experiencing strong electrostatic interactions [i.e., negatively charged dopants (divalent dopants at trivalent cations) are attracted by positively charged oxygen vacancies on surface dopants and pushed from negatively charged A-site vacancies in the bulk (Fig. 5b)]. Tsvetkov et al. [23] further reported the effective suppression of Sr surface segregation through the surface modification of $La_{0.8}Sr_{0.2}CoO_{3-\delta}$ perovskite oxide with less reducible cations (e.g., Nb^{5+}, Ti^{4+}, Hf^{4+} and Al^{3+}) at the surface. The ambient pressure X-ray photoelectron spectroscopy and X-ray adsorption spectroscopy results allowed these researchers to conclude that the observed suppression of surface segregation originated from more oxidized surfaces (i.e., less oxygen vacancies) as imparted by surface modification, which can weaken electrostatic interactions between perovskite oxide surfaces and Sr cations. These results further highlighted the essential role of surface oxygen vacancies in driving surface segregation in perovskite oxides.

Oxygen vacancies can also affect B-site cation exsolution [48]. For example, Kwon et al. [25] investigated B-site cation segregation in layered $PaBaMn_2O_{5+\delta}$ perovskite oxides doped with various transition metals (e.g., Co, Ni, Mn and Fe) at B-sites and found that Co and Ni more easily migrated to the surface than Mn or Fe. These researchers also reported based on DFT calculations that Co and Ni dopants can facilitate more facile co-segregation with oxygen vacancies to the surface than Mn and Fe (Fig. 6) and that co-segregated oxygen vacancies can further contribute to the stabilization

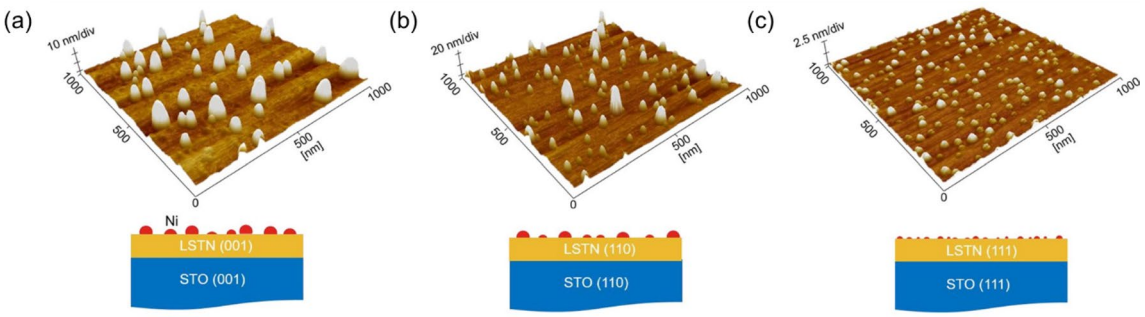

Fig. 7 Atomic force microscopy images of the top surface structures of $La_{0.2}Sr_{0.7}Ti_{0.9}Ni_{0.1}O_{3-\delta}$ thin films with **a** (001), **b** (110) and **c** (111) surface orientations after being reduced in dry H_2 at 900 °C for 12 h. Reproduced with permission from Ref. [50]. Copyright 2019, American Chemical Society

of the metallic dopant phase on the surface, which is also important for facile B-site cation exsolution.

2.1.3 Crystallinity and Surface Orientation

Perovskite oxide crystallinity and surface orientation both affect surface segregation. For example, Cai et al. [37] reported that low $La_{0.6}Sr_{0.4}CoO_{3-\delta}$ thin-film crystallinity can suppress Sr surface enrichment and suggested that the disordered structure can weaken both elastic and electrostatic driving forces by (1) allowing lattices to possess extra spacing (e.g., defects, cation vacancies) to accommodate relatively large Sr cations in the bulk and (2) increasing the oxygen vacancy content in the bulk. Surface orientation also plays a critical role in cation surface segregation. For example, Piskin et al. [49] reported the strong dependency of SrO_x species coverage on $La_{0.6}Sr_{0.4}CoO_3$ dense pellet surfaces on surface orientation in which the coverage of Sr increased in the order: (001) > (101) > (111). The effects of surface orientation are different for B-site cation segregation however. For example, Kim et al. [50] investigated $La_{0.2}Sr_{0.7}Ti_{0.9}Ni_{0.1}O_{3-\delta}$ thin films with three different surface orientations (001), (110) and (111) after chemical reduction in dry H_2 at 900 °C. They observed a strong correlation between surface orientation and the morphology and surface coverage of the exsolved Ni nanoparticles in which the size of Ni particles decreased in the order: (001) > (110) > (111), whereas the coverage of particles increased in the order: (001) < (110) < (111) (Fig. 7). These researchers further highlighted the critical role of interfacial energy between exsolved Ni particles and perovskite host lattices in the nucleation and particle growth processes. High interfacial energy can lead to higher nucleation energy barriers (i.e., slow nucleation rates and low particle populations) and larger critical nucleation sizes. Because of this, the (001) facet with relatively higher interfacial energy will result in less area coverage but larger particle sizes than the other facets.

2.1.4 Lattice Strain

Lattice strain can also affect the elastic energy of lattice cations and therefore influence the level of cation surface segregation in perovskite oxides. In general, tensile strain in lattices can cause A-site cation surface segregation, whereas compressive strain inhibits segregation [22, 51]. For example, Cai et al. [52] applied pulsed laser deposition (PLD) to deposit tensile- and compressive-strained $La_{0.8}Sr_{0.2}CoO_3$ (LSC) thin films over $SrTiO_3$ (STO) and $LaAlO_3$ (LAO), respectively, and reported stronger Sr surface enrichment in the tensile-strained LSC/STO as compared with the compressive-strained LSC/LAO. Lattice tensile strain can also intensify Sr surface segregation in $La_{0.7}Sr_{0.3}MnO_3$ as compared with compressive strain [53]. Consistently, Ding et al. [54] and Yu et al. [20] reported similar effects of lattice strain on Sr surface segregation in (La, Sr)(Co, Fe)$O_{3-\delta}$ (LSCF) oxides.

2.2 External Conditions

2.2.1 Temperature

Although the minimization of elastic and electrostatic energy is the main thermodynamic driving force for cation surface segregation, the rates of cation migration from perovskite oxide bulk to the outer surface are slow due to kinetic limitations. Therefore, surface cation enrichment is usually more prominent at elevated temperatures and longer annealing durations (Fig. 3b, c) [19, 22, 27, 28, 41, 55, 56]. For example, Wen et al. [57] applied in situ ambient pressure XPS to monitor Sr surface segregation in $La_{0.6}Sr_{0.4}CoO_{3-\delta}$ films at temperatures between 200 and 520 °C and reported that Sr segregation became increasingly pronounced with increasing temperature and quickly (within 1 h) reached equilibrium at certain temperatures. This quick response of Sr segregation to temperature change implies that temperature also contributes to the thermodynamic driving force in addition to the kinetic acceleration of surface segregation. Using isotopic ^{86}Sr and cation tracers, Kubicek et al. [58] further investigated cation diffusivity over $La_{0.6}Sr_{0.4}CoO_{3-\delta}$ thin films and reported a less than one order of magnitude difference in diffusivity between A-site and B-site cations at temperatures above 600 °C (relatively small B-site cations diffuse faster than A-site cations), demonstrating that kinetic contributions of temperature are minor as compared with corresponding thermodynamic contributions to cation segregation.

2.2.2 Gas Atmosphere

Gas molecules and partial pressures have significant impacts on the interactions between perovskite oxide surfaces and bulk. Oxygen partial pressures can also influence the oxidation state and size of reducible cations as well as oxygen vacancy content, which in turn can affect elastic and electrostatic interactions within perovskites. As mentioned, the segregation of A-site cations such as Sr normally occurs under oxidizing environments (Fig. 3), whereas the exsolution of B-site cations such as reducible transition metals is facilitated through reducing environments (H_2 gas or high vacuum) [26, 27, 31, 59] (Figs. 4, 7). The perovskite oxide surfaces are sensitive to gas molecules such as moisture and CO_2 to induce cation segregation. For example, Sharma et al. [60] reported pronounced alkaline-earth dopant surface segregation under humid atmosphere and suggested that the promoted cation segregation was related to interactions

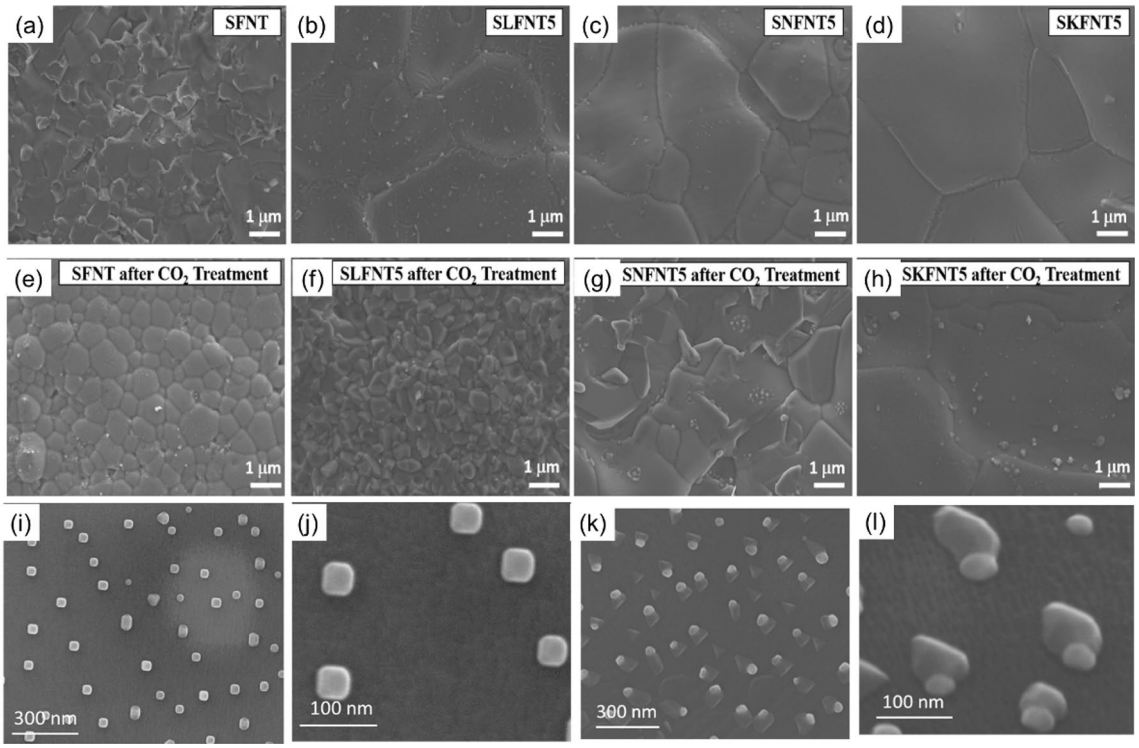

Fig. 8 SEM micrographs of dense pellets of $SrFe_{0.8}Nb_{0.1}Ta_{0.1}O_{3-\delta}$ doped with alkali metals (i.e., Li, Na and K) at A-sites before **a**–**d** and after **e**–**h** treatment in the presence of CO_2 at 600 °C. Reproduced with permission [18], Copyright 2019, American Chemical Society. SEM images of particles exsolved from $La_{0.8}Ce_{0.1}Ti_{0.6}Ni_{0.4}O_3$ perovskite oxide **i**–**j** in the presence of 5% CO at 900 °C for 10 h and **k**–**l** under 2.5% H_2O/5% H_2 at 1000 °C for 10 h. Reproduced with permission from Ref. [32]. Copyright 2019, American Chemical Society

between moisture and surface oxygen vacancies. Similarly, Niania et al. [30] reported more significant Sr segregation for $La_{0.6}Sr_{0.4}Co_{0.2}Fe_{0.8}O_{3-\delta}$ in the presence of water than in air or pure O_2.

The presence of acidic CO_2 can further drive the surface segregation of basic cations such as alkaline-earth and alkali metals. These CO_2-cation interactions can also promote the carbonation of cations at the surface [18, 61] and induce the destruction of crystal structures in the subsurface region [21]. Our previous work on $SrCo_{0.85}Ta_{0.15}O_{3-\delta}$ cathodes for SOFCs achieved more significant Sr surface enrichment if annealed under 10% CO_2 in air as compared with treatment in air alone [18]. In the presence of CO_2, additionally, the $Sr_{0.95}A_{0.05}Fe_{0.8}Nb_{0.1}Ta_{0.1}O_{3-\delta}$ (A is the alkali metal dopant) showed significant alkali metal dopant segregation to the surface as compared with ones without CO_2 treatment (Fig. 8). Moreover, interactions between basic alkali metals and acidic CO_2 can serve as a key driving force for alkali metal segregation in addition to elastic interactions due to dopant/host size mismatch. These combined driving forces were confirmed by XPS in our study, which showed that cation surface segregation increased following the trend: K > Li > Na.

Despite the essential role of reducing atmospheres in facilitating B-site cation exsolution, gas molecules can also influence the morphology of exsolved particles. For example, hydrogen reduction normally leads to quasi-spherical shaped particles [25, 27]. In contrast, Neagu et al. [32] reported that high vacuum conditions can lead to nanoparticles on the surface of $La_{0.8}Ce_{0.1}Ti_{0.6}Ni_{0.4}O_3$ with well-defined facets, whereas CO reduction-produced cubic shaped exsolved Ni particles and humidified hydrogen led to the formation of heterostructures.

2.2.3 Electrochemical Polarization

Electrical polarization (or bias) can vary oxygen chemical potential, cation oxidation states and lattice size, all of which have profound impacts on the interactions between perovskite oxide surfaces and bulk. Typically, cathodic polarization can lower oxygen chemical potentials, create oxygen vacancies and increase the ionic size of reducible cations in lattices, whereas anodic polarization results in the opposite. These properties are related to the elastic and electrostatic driving forces for cation segregation in which cathodic polarization can increase A-site cation segregation degrees over perovskite oxides such as LSC [56, 62–64] and LSM

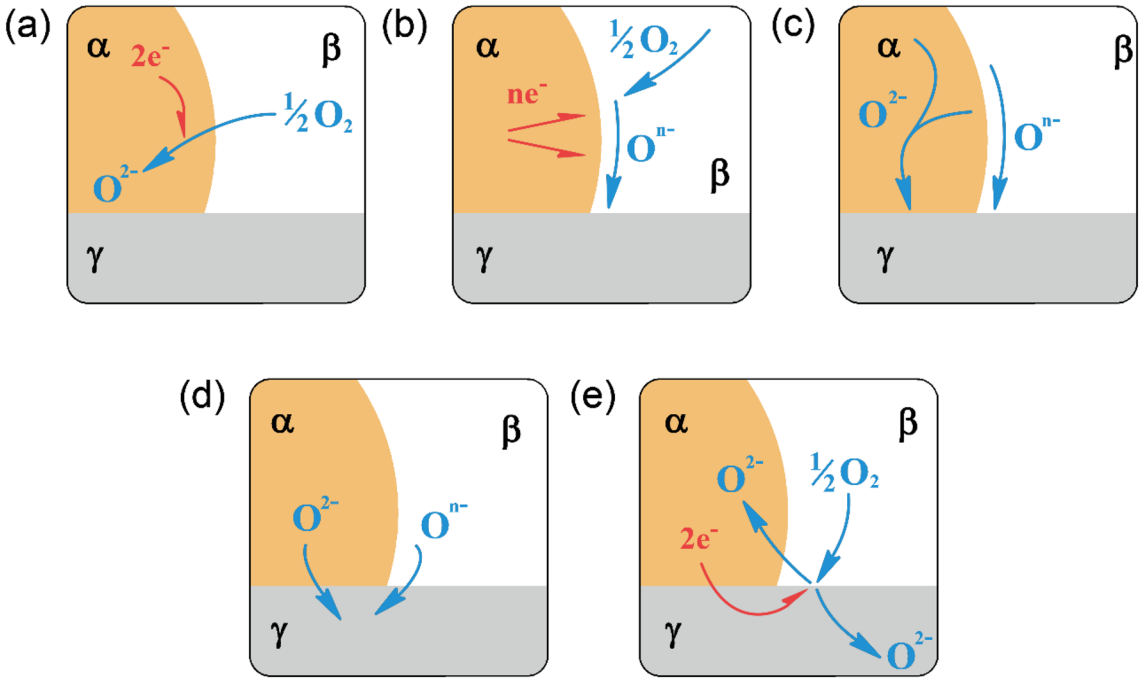

Fig. 9 Diagrams of typical mechanisms believed to govern ORR in cathode materials. α, β and γ represent electronic, gas and ionic phases, respectively. **a** Incorporation of oxygen molecules into the electronic bulk phase (if α is a mixed ionic-electronic conductor); **b** adsorption and/or partial reduction of oxygen molecules on the electronic phase surface; **c** bulk phase or surface phase migration of oxygen ions (O^{2-} and O^{n-}, respectively) toward the α/γ interface; **d** charge transfer of O^{2-} or O^{n-} across the α/γ interface; **e** one or multiple mechanisms wherein the electrolyte is active for generating and transporting oxygen species. Reproduced with permission from Ref. [69]. Copyright 2004, American Chemical Society

[35, 65, 66]. Anodic polarization can impart effects similar to high oxygen partial pressure that can promote A-site cation segregation. Despite this, inconsistent results have been reported in the literature. For example, Huber et al. [67, 68] reported that the degree of Sr enrichment decreased under cathodic polarization and increased under anodic polarization in LSM and (La, Sr)(Cr, Mn)O_3 perovskite oxides. Kim et al. [35] recently also reported that both cathodic and anodic polarizations can lead to significant alkaline-earth dopant segregation on the surface over deposited $LaMnO_3$ perovskite oxides. These inconsistencies may be due to the various synthesis methods and annealing processes used to obtain oxides prior to electrochemical polarization in the different studies. Despite this, these results do highlight the essential role of balance between elastic and electrostatic driving forces. According to results by Kim et al. [35], elastic driving forces are dominant if oxides are under anodic polarization, whereas electrostatic interactions become crucial if oxides are cathodically polarized. This conclusion is reasonable because anodic polarization tends to shrink lattices through the oxidization of cations, which promotes elastic interactions due to dopant/host size mismatch. Cathodic polarization tends to alleviate elastic interactions by expanding lattices to create more oxygen vacancies and therefore increases electrostatic interactions that attract cation segregation.

3 Oxygen reduction and Mixed Conductivity

3.1 ORR Mechanism

The function of a cathode is to reduce oxygen molecules into oxygen ions as represented by Eq. (1). This reaction primarily proceeds through (1) O_2 diffusion into a porous cathode, (2) O_2 adsorption onto the cathode surface, (3) the partial or complete reduction of O_2 into oxygen ions such as O^{2-} and O^- and (4) oxygen-ion migration to the electrolyte along the cathode surface, the cathode-electrolyte interface and the cathode bulk phase (Fig. 9) The rate of ORR is mainly controlled by either oxygen surface exchange (including oxygen dissociative adsorption and lattice incorporation) or oxygen-ion diffusion.

$$\frac{1}{2}O_2(g) + 2e^- \rightarrow O^{2-} \quad (1)$$

In general, oxygen surface exchange can be interpreted as three consecutive stages involving (1) oxygen adsorption,

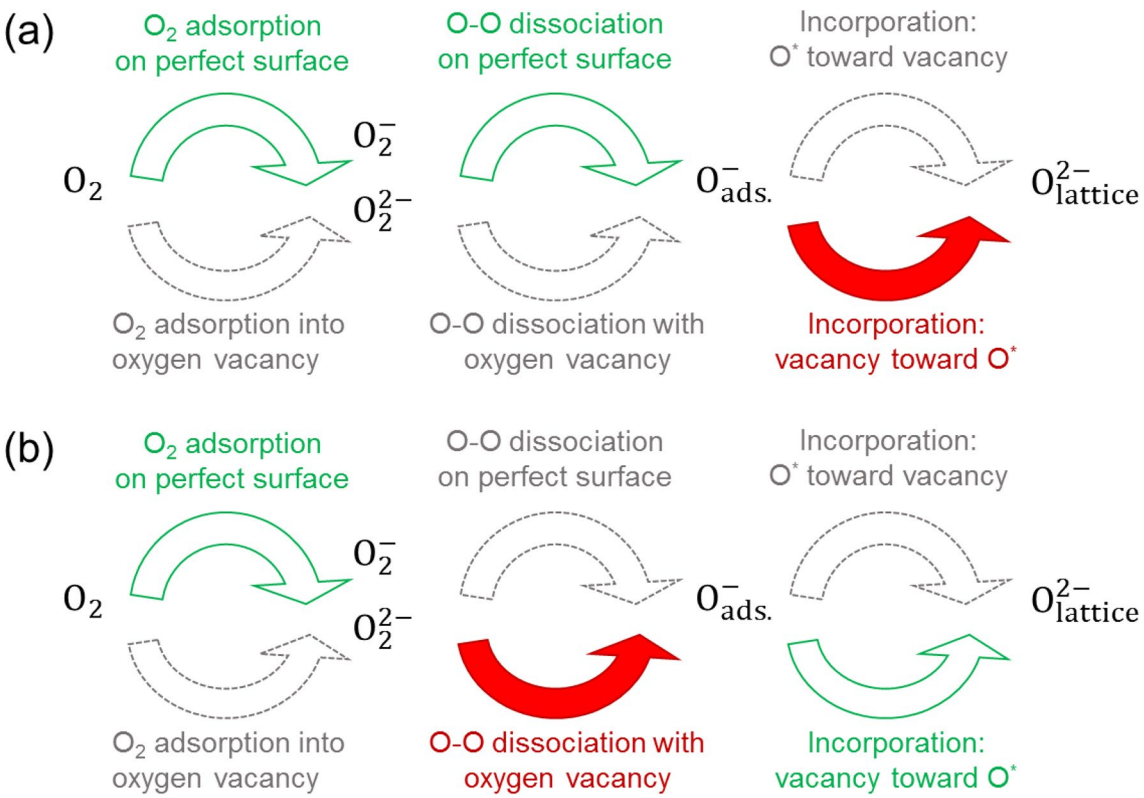

Fig. 10 Schematic of possible pathways for oxygen incorporation into mixed ionic and electronic conductors (MIECs) with **a** few oxygen vacancies and **b** abundant oxygen vacancies according to results from ab initio calculations. Here, red arrows indicate the rate-limiting step, green arrows are the fast processes and dashed arrows represent the slower alternative parallel step. Reproduced with permission from Ref. [70]. Copyright 2012, Materials Research Society

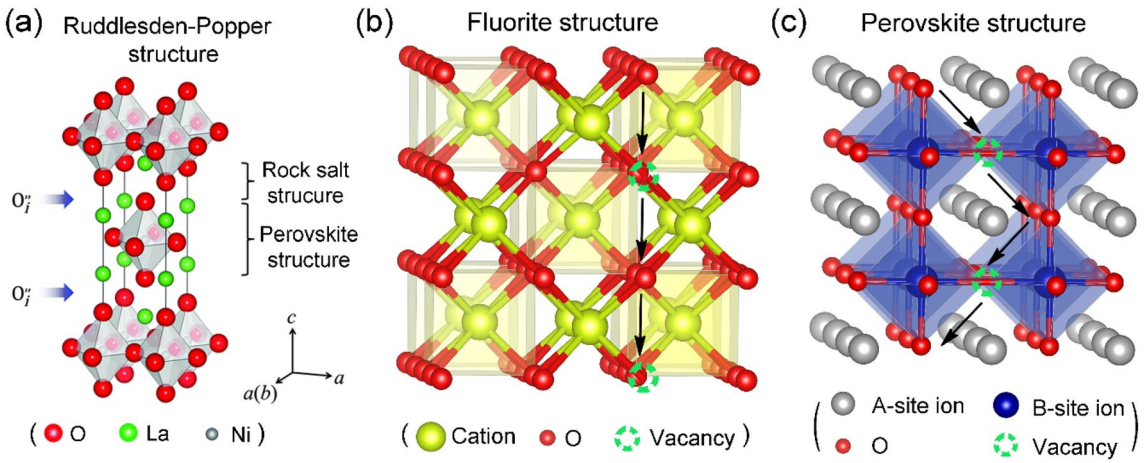

Fig. 11 Crystal model of **a** a RP structure. Reproduced with permission from Ref. [72]. Copyright 2016, Royal Society of Chemistry. Oxygen migration pathway in **b** fluorite and **c** perovskite structures, arrows in (b) and (c) represent the migration orientation of oxygen ions

(2) oxygen dissociation and (3) oxygen species incorporation into crystal lattices (Fig. 10). The rate-determining step of surface exchange is highly dependent on the availability of surface oxygen vacancies. For example, for cathode surfaces with limited oxygen vacancies such as LSM, oxygen migration coupled incorporation may be the rate-controlling

step for oxygen surface exchange [71], whereas for cathode surfaces with sufficient oxygen vacancies such as LSCF and BSCF, surface exchange processes are generally dominated by the dissociation of oxygen ions (O_2^- or O_2^{2-}).

Oxygen diffusion is widely considered to be a hopping process involving oxygen ions from one equilibrium site to an adjacent site along the surface or within the bulk of a material through interstitial or vacancy mechanisms. For example, oxygen-ion migration in materials such as RP structured oxides (Fig. 11a) [72] usually relies on the interstitial mechanism. The oxygen ions located at one interstitial site (i.e., free space) migrate to an adjacent interstitial site [73, 74]. Alternatively, oxygen-ion transport in fluorite-/perovskite-type materials (Fig. 11b, c) occurs through the vacancy mechanism [75] in which oxygen diffusion is facilitated through oxygen-ion hopping from occupied oxygen sites to neighboring vacancy sites [76]. The oxygen vacancy concentration in corresponding materials is critical for oxygen diffusion and overall ORR kinetics. Because the vacancy mechanism is more common and suitable for oxygen ionic conduction, this review will mainly provide an overview of vacancy-driven progress in oxygen-ion diffusion. Detailed information concerning oxygen vacancy formation and oxygen-ion mobility is discussed in Sect. 3.2.

3.1.1 Oxygen Surface Exchange Versus Oxygen-Ion Diffusion

The oxygen surface exchange coefficient (k_{chem}) and the oxygen-ion diffusion coefficient (D_{chem}) are two parameters that can be used to quantify ORR reaction rates on MIEC material surfaces and bulk, respectively. The k_{chem} reflects electrode surface oxygen kinetics (i.e., oxygen adsorption, dissociation and incorporation [77]), whereas D_{chem} describes bulk oxygen-ion diffusion rates. Several techniques such as electrical conductivity relaxation (ECR) [78, 79] and isotope exchange [80] measurements can be applied to obtain k_{chem} and D_{chem} parameters. For example, ECR experiments can be used to calculate k_{chem} and D_{chem} values through the following formula [81, 82]:

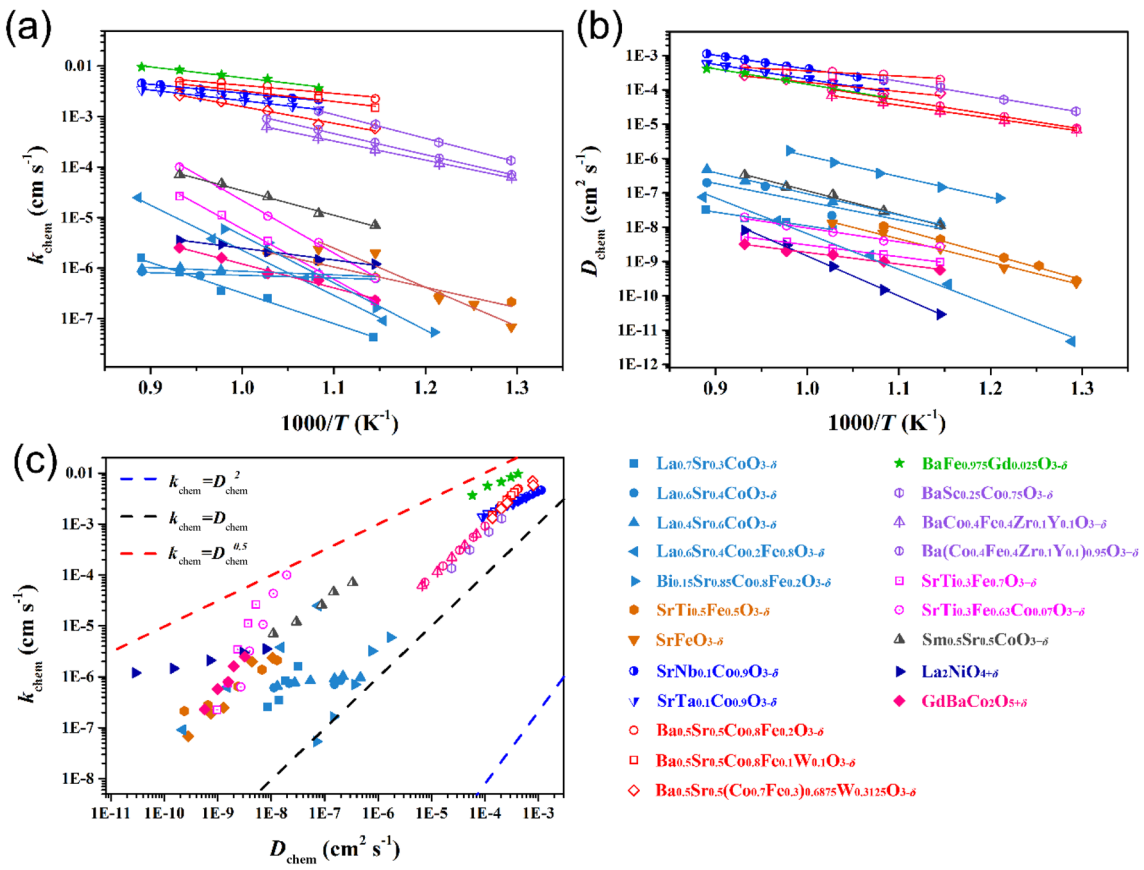

Fig. 12 Oxygen transport data of perovskite-type and other oxides from literature published from 2016 to 2020 [83–90], including the temperature dependence of **a** k_{chem} and **b** D_{chem} and **c** the correlation between k_{chem} and D_{chem}. Materials with different symbols are also shown in the figure

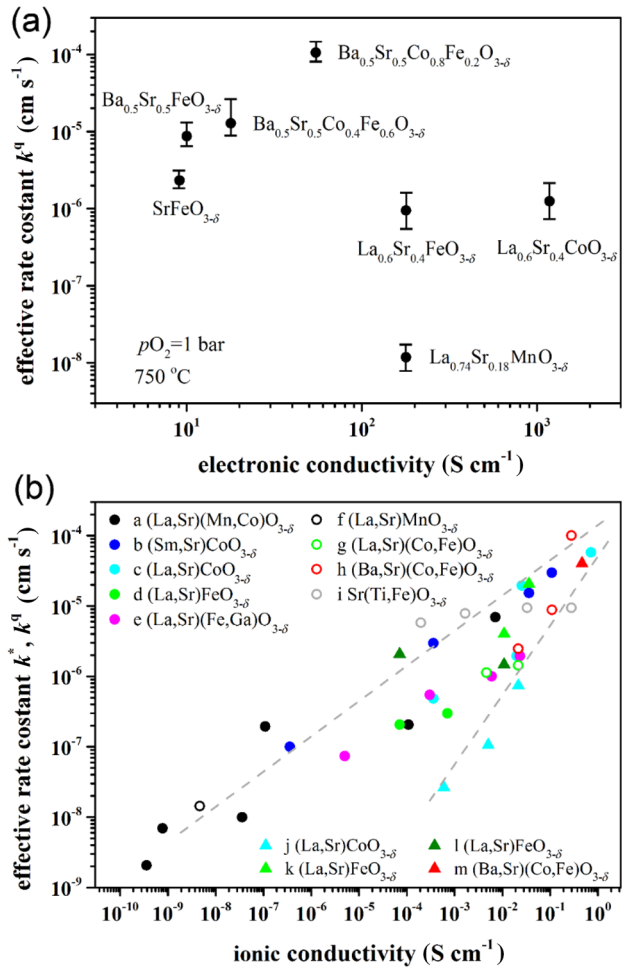

Fig. 13 **a** Correlation between electronic conductivity and the oxygen exchange rate constant (k) at 750 °C and P_{O_2} =1 bar. **b** Bulk ionic conductivity as a function of surface exchange coefficient as determined by isotope exchange (k^*) and chemical relaxation (k^q) experiments. Reprinted with permission [70], Copyright 2012, Materials Research Society

$$\sigma_n = \frac{\sigma(t)-\sigma(0)}{\sigma(\infty)-\sigma(0)} = 1 - \sum_{p=1}^{\infty} \frac{2L_x^2}{\beta_{p,x}^2(\beta_{p,x}^2+L_x^2+L_x)} \exp\left(\frac{\beta_{p,x}^2}{l_x^2} D_{\text{chem}} t\right) \times \sum_{q=1}^{\infty} \frac{2L_y^2}{\beta_{q,y}^2(\beta_{q,y}^2+L_y^2+L_y)} \exp\left(\frac{\beta_{q,y}^2}{l_y^2} D_{\text{chem}} t\right) \times \sum_{r=1}^{\infty} \frac{2L_z^2}{\beta_{r,z}^2(\beta_{r,z}^2+L_z^2+L_z)} \exp\left(\frac{\beta_{r,z}^2}{l_z^2} D_{\text{chem}} t\right) \quad (2)$$

in which $\sigma(0)$, $\sigma(t)$ and $\sigma(\infty)$ are the initial, time-dependent and final conductivities, respectively, whereas L_x, L_y and L_z parameters are defined as:

$$L_x = \frac{l_x K_{\text{chem}}}{D_{\text{chem}}}, \quad L_y = \frac{l_y K_{\text{chem}}}{D_{\text{chem}}} \quad \text{and} \quad L_z = \frac{l_z K_{\text{chem}}}{D_{\text{chem}}} \quad (3)$$

in which 2 lx, $2l_y$ and $2l_z$ are the side lengths of the bar sample. In addition, $\beta_{p,x}$, $\beta_{q,y}$ and $\beta_{r,z}$ coefficients are the roots of transcendental equations:

$$\beta_{p,x}\tan\beta_{p,x} = L_x, \quad \beta_{q,y}\tan\beta_{q,y} = L_y \quad \beta_{r,z}\tan\beta_{r,z} = L_z \quad (4)$$

Here, the magnitudes of p, q and r provide partial influence on calculation accuracy.

Tsvetkov et al. [23] further proposed that k_{chem} can be obtained based on surface polarization resistance (i.e., low-frequency impedance response) as measured using electrochemical impedance spectroscopy (EIS) through Eq. (5):

$$k_{\text{chem}} = \frac{k_B T}{4e^2 c_o R_s} \quad (5)$$

in which k_B is the Boltzmann constant, T is the temperature, e is the electronic charge, c_o is the total lattice oxygen concentration, and R_s is the low-frequency impedance of surface polarization resistance.

A summary of the k_{chem} and D_{chem} values of common cathode materials recently reported in the literature is given by Fig. 12. The reported coefficients, especially k_{chem}, can vary significantly over the same material, which may be due to surface sensitivity arising from segregation (e.g., SrO, BaO), reconstruction and contamination [5]. The values of k_{chem} and D_{chem} (Fig. 12a, b) were also reported to decrease with temperature, which consequently reduces ORR kinetics at lower temperatures. Furthermore, the values of k_{chem} were ~ 0.2–2 orders higher than those of D_{chem} over the same material at the same temperature, which is a trend that is consistent with findings by Souza and Kilner [91] in (La, Sr)(Mn, Co)O_3.

3.2 Electrical Conductivity

Electrical conductivity typically consists of electronic and ionic conductivity [12]. A high electronic conductivity can ensure electron transport to active sites to facilitate charge transfer to adsorbed oxygen species, whereas high oxygen ion conductivity is vital for reduced oxygen-ion transport to electrolyte. Because of this, high electronic and ionic conductivities are essential for efficient ORR catalysis, particularly at reduced temperatures. However, the formation of oxygen vacancies can reduce charge carriers such as holes for electron conduction, meaning the elucidation of which conductivity dominates ORR kinetics is crucial in cathode material optimization, especially at reduced temperatures. Based on the correlation summary provided by Wang et al. [70] between electronic conductivity and surface exchange coefficient (Fig. 13a), no apparent relationship exists between these two parameters, suggesting that electronic conductivity is not a dominant factor for ORR catalysis. This also explains why BSCF with relatively low electronic

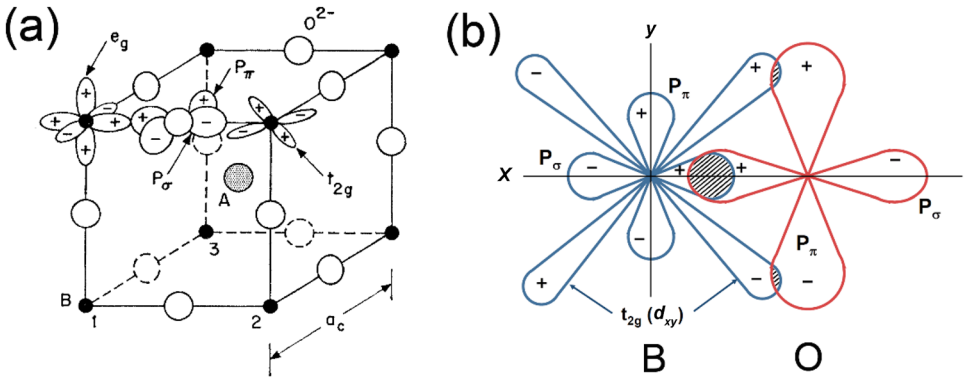

Fig. 14 Schematic of **a** an ABO_3 pseudo-cubic (or cubic) structure with oxygen-ion p_σ and p_δ orbitals and B-site cation e_g ($d_{x^2-y^2}$, d_{z^2}) and t_{2g} (d_{xy}, d_{yz}, d_{xz}) orbitals. Reproduced with permission from Ref. [101], Copyright 1967, American Physical Society. **b** Covalent bonds of p_σ–p_σ and p_π–d_{xy} between an oxygen ion and a B-cation

conductivity is more ORR active than $La_{0.74}Sr_{0.18}MnO_{3-\delta}$. In contrast, a clear trend exists between oxygen-ion conductivity and surface exchange kinetics (Fig. 13b), highlighting the dominant role of oxygen-ion conductivity over electronic conductivity in ORR catalysis.

3.2.1 Electron Conduction

Electron conduction in most perovskite cathodes is believed to experience small polaron hopping, which is a diffusion-type process that involves electrons (or holes) hopping between B-site transition metal ions and mixed valences (e.g., TM^{3+}/TM^{4+}, so-called redox couples) such as Fe [92], Cu [93], Co [89], Ce [94] and Mn [95, 96]. Charge carrier migration generally occurs in conjunction with local structural distortion, and polarons are defined as quasiparticles consisting of charge carriers and associated local structural distortion [97]. A high concentration of charge carriers (e.g., electrons or holes) and availability of redox couples as hopping sites are prerequisites for fast electron conduction. The small polaron hopping process can generally be described by Eq. (6) [97, 98]:

$$\rho(T) = AT^m \exp\left[\left(\frac{T_0}{T}\right)^p\right] \quad (6)$$

in which $\rho(T)$ is the electrical resistivity, A is a constant, T is the temperature, T_0 is the characteristic temperature, and m and p are interrelated parameters that depend on the exact mechanism of the hopping process.

In particular, hopping sites can be created by altering material composition (i.e., incorporating aliovalent cations into perovskite structures). Using $Pr_{1-x}Sr_xFeO_3$ [99] as an example, the partial substitution of divalent Sr cations into Pr-sites can increase electronic conductivity and Fe cation charge compensation from + 3 to + 4, which will leads to increased Fe^{3+}/Fe^{4+} coupling for electron hopping. Besides, the charge disproportionation of B-site cations from intermediate to high or low valences can also increase the level of hopping sites. One typical example is the disproportionation of Fe^{3+} into Fe^{2+} and Fe^{4+} in $Ba_{1-x}La_xFeO_{3-\delta}$ ($x = 0.1$–0.4), which can increase electronic conductivity [100]. Note that these composition alterations can further affect the structural symmetry of materials, which can be reflected by p-d orbital overlap between B-site cations and oxygen ions (Fig. 14) [97, 101]. With a perfect cubic perovskite structure, this p–d overlap can be maximized with an optimal B–O–B bond angle of 180° to facilitate the mobility of electrons (or holes) from t_{2g} orbitals to neighboring p_π orbitals.

Temperature is a significant factor for electronic conductivity based on Eq. (6). Temperature can also affect the number of hopping sites by influencing the electronic structure of B-site cations. Using Co-containing oxides as an example, Co^{3+} at low temperatures exhibiting low-spin configuration ($t_{2g}^6e_g^0$) can be transformed into intermediate-spin ($t_{2g}^5e_g^1$) and subsequent high-spin ($t_{2g}^4e_g^2$) configurations with increasing temperature [102, 103]. Because of this, the reduction of temperature will result in electron transfer from high-spin Co^{3+} to low-spin cations that are prone to transformation into Co^{4+} and Co^{2+} [104].

Gas atmospheres (e.g., increasing or decreasing oxygen partial pressure (P_{O_2})) can also introduce redox couples and promote electron conduction [105]. For example, Mizusaki et al. [106] reported that increases in P_{O_2} for (La, Sr)$FeO_{3-\delta}$ at temperatures above 900 °C can transform n-type conductivity (Fe valence between + 2 and + 3) into p-type conductivity (Fe valence between + 3 and + 4) to increase electrical conductivity. Similar results have also been observed in other ion-containing materials such as $La_{0.6}Sr_{0.4}Co_{0.8}Fe_{0.2}O_{3-\delta}$ [107], $La_{1-x}Sr_xFeO_{3-\delta}$ ($x = 0$, 0.1) [108] and $SrFe_{1-x}Si_xO_{3-\delta}$ ($x = 0.05$–0.20) [109].

3.2.2 Oxygen-Ion Conduction

As discussed in Sect. 3.1, the ionic conduction of perovskite-type materials occurs through an oxygen vacancy mechanism that is related to oxygen vacancy formation and oxygen-ion migration in lattices.

3.2.2.1 Formation of Oxygen Vacancy Oxygen vacancies, commonly described using oxygen non-stoichiometry, are anion defects in lattices as a result of doping or external conditions (e.g., temperature and gas atmosphere change). In most perovskite oxides, these two factors can lower the overall positive charge of cations and create oxygen vacancies to compensate for the induced charge imbalance. A typical example in B-site cations is described in Eq. (7):

$$2B_B^{\times} + O_O^{\times} \rightarrow V_O^{\bullet\bullet} + 2B_B' + \tfrac{1}{2}O_2 \quad (7)$$

in which "×" represents neutrality and "·" and "′" represent the positive and negative charges , respectively.

Although the incorporation of low oxidation state dopants can reduce overall positive charge in corresponding lattices, the formation of oxygen vacancies depends on the reducibility of B-site transition metals (e.g., Mn, Fe, Co and Ni) because induced charge imbalance can also be compensated by reducing the average valence of B-sites. Here, the creation of oxygen vacancies is easier in the case of Co- and Ni-based perovskite oxides as compared with Mn- and Fe-based perovskites, possibly due to the poorer reducibility of Co and Ni than Mn and Fe [110–113].

Lattice geometry is another important factor in the formation of oxygen vacancies. For example, doping with small-sized B-site cations can force corresponding B-site hosts to increase in size to maintain a perovskite structure, which is normally accompanied by the reduction of valence states and thus the formation of oxygen vacancies. For example, Lee et al. [114] reported that smaller ionic radius Ge^{4+} doping at B-sites in $PrBa_{0.5}Sr_{0.5}Fe_{2-x}Ge_xO_{5+\delta}$ (PBSFG, $x=0$ and 0.1) perovskite can facilitate the reduction of Fe^{4+} to Fe^{3+} and the generation of oxygen vacancies by reducing the coordination state from FeO_6 to FeO_4 octahedra. Doping with large ionic sized A-site cations can also expand lattices and therefore increase the size of B-site reducible cations to create oxygen vacancies. For example, Merkle et al. [115] applied DFT calculations to investigate oxygen vacancy formation and migration in $Ba_{1-x}Sr_xCo_{1-y}Fe_yO_{3-\delta}$ ($x=0.5$, 1, $y=0$, 0.2, 0.25, 0.75 and 1) perovskites and found that Ba ($x=0.5$) doping at A-sites can reduce the formation energy of oxygen vacancies by 0.3 eV due to the larger Ba ions as compared with Sr ions, which can result in lattice expansion and low-valence Co.

External conditions such as temperature and gas atmosphere are essential to the equilibrium of oxygen species in gas and perovskite solid phases. At elevated temperatures, especially above 400 °C, oxygen is prone to escape from the solid phase to the gas phase, which causes the solid phase to possess lowered overall lattice positive charge and experience the formation of oxygen vacancies. Similarly, lowering oxygen partial pressure in gas atmospheres can shift equilibriums to create lattice oxygen vacancies [116].

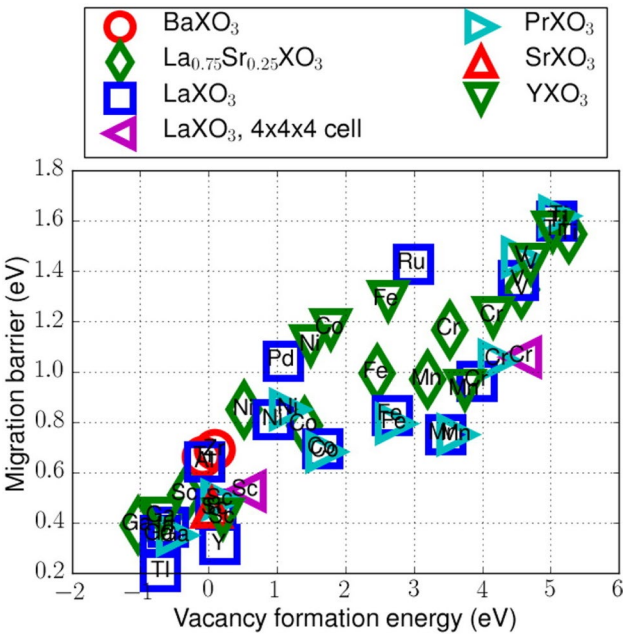

Fig. 15 Relationship between oxygen migration barrier and oxygen vacancy formation energy calculated at 900 °C and 0.1 atm (1 atm=101.325 kPa) P_{O_2}. Reproduced with permission from Ref. [126]. Copyright 2016, Elsevier

Different from doping effects, external condition effects largely depend on equilibrium conditions, meaning that corresponding oxygen vacancy changes are reversible if temperatures and gas atmospheres revert back to original conditions. Such behavior provides opportunities to evaluate oxygen surface exchange kinetics by varying oxygen partial pressure [12, 117, 118].

High oxygen vacancy content that is above optimal can also destabilize beneficial perovskite structures. For example, the transformation of $SrCoO_{3-\delta}$-based oxides into an oxygen-ordering brownmillerite-type structure with significantly increased oxygen vacancy content is easily achievable through exposure to either high temperature or reduced oxygen partial pressure [119–122] and will significantly reduce oxygen condition rates in the corresponding lattice and therefore degrade overall cathode performance. In addition, the formation of oxygen vacancies based on Eq. (7) can reduce the concentration of charge carriers such as holes for hopping processes and therefore degrade electronic conductivity. This is a common phenomenon in many perovskite materials such as $SrCoO_{3-\delta}$-based perovskite oxides [12, 18, 19, 123, 124].

3.2.2.2 Mobility of Oxygen Ions In addition to oxygen vacancy content, the ease of oxygen-ion migration in corresponding lattices can also determine overall oxygen diffusion rate. Moreover, oxygen-ion migration is naturally

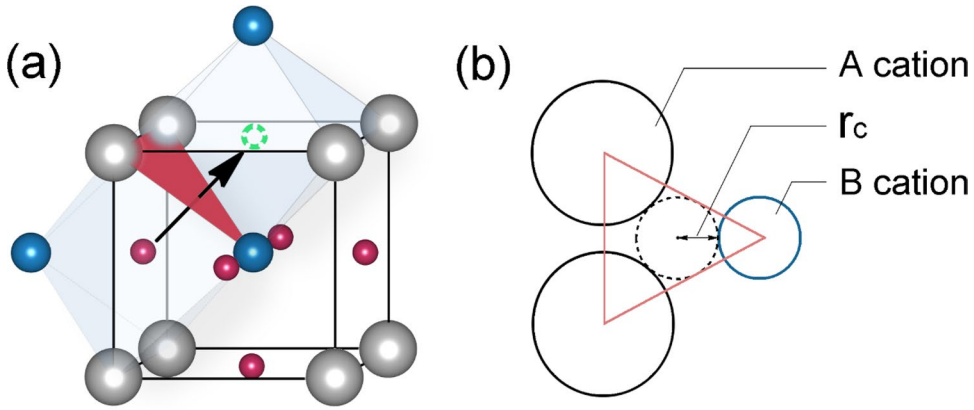

Fig. 16 **a** Schematic of oxygen-ion migration from an occupied site to an adjacent vacant site through permeation through the A_2B trigonal plane (red area). **b** Determination of the critical radius (r_c) among the A_2B trigonal plane

accompanied by the formation and breakage of metal–oxygen bonds and the diffusion of oxygen-ions through lattice voids. Because of this, the bond strength between metals and oxygen and the geometry of lattices are important factors determining oxygen-ion mobility. Weakened interactions further favor oxygen-ion migration [125]. For example, Mayeshiba and Morgan [126] applied ab initio methods to investigate the energy barriers of oxygen vacancies in more than 40 perovskite oxide models and compared corresponding oxygen-ion migration energy with oxygen vacancy formation energy (Fig. 15) to confirm that low metal–oxygen bond strength as measured by oxygen formation energy and oxygen p-band centers generally led to facile oxygen-ion migration in lattices.

High symmetry can further promote high oxygen-ion conduction, particularly in polycrystalline materials, because corresponding oxygen ions can migrate isotopically to adjacent vacancy sites. This is well exemplified by the inferior oxygen-ion conductivity of oxygen-vacancy ordering brownmillerite structures as compared with simple cubic perovskites with less oxygen vacancy content [127–129]. In addition, the oxygen ions need to permeate through a trigonal planar phase established by two A-site and one B-site ions (Fig. 16a), whereas the large space surrounding an A_2B triangle phase enables facile oxygen-ion migration. This surrounding space can be referred to as a "saddle point" in which the critical radius (r_c) can be defined to describe the size of the space (Fig. 16b) based on Eq. (8):

$$r_c = \frac{r_B^2 - r_A^2 + a\left(\frac{3}{4}a - \sqrt{2}r_B\right)}{2(r_A - r_B) + \sqrt{2}a} \tag{8}$$

in which r_A and r_B are the radii of A- and B-site cations, whereas a represents the lattice constant and the pseudo-cubic structure and can be calculated by using Eq. (9) [130]:

$$a \approx \sqrt[3]{V_{Cell}} = 2.15r_B + 2.72 - 1.40(\tau^{-1} - 1) \tag{9}$$

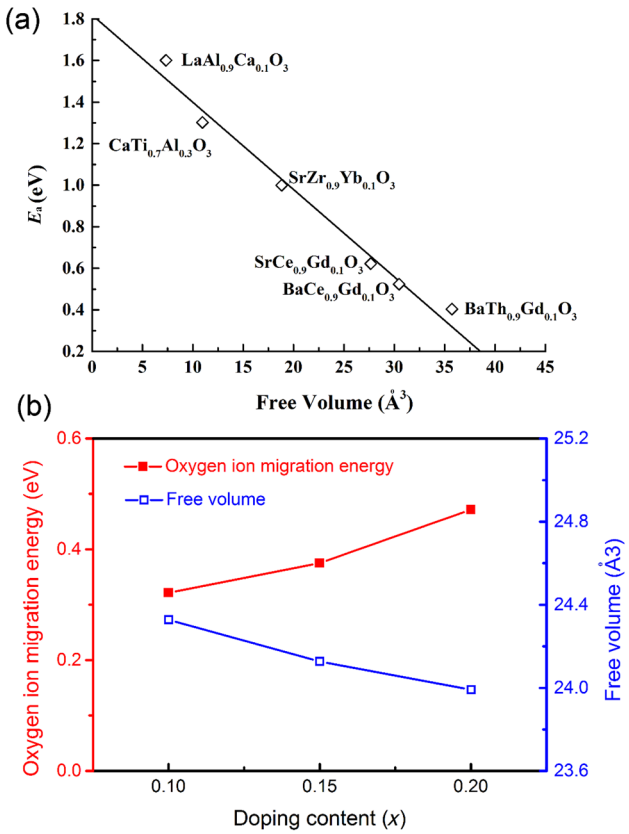

Fig. 17 **a** Activation energy of oxygen-ion migration in various perovskite oxides as a function of free volume. Reproduced with permission [135], Copyright 1992, The Electrochemical Society. **b** Influence of doping content (x) in $BaFe_{1-x}In_xO_{3-\delta}$ (x = 0.1–0.2) at 900 °C on oxygen-ion migration energy and free volume. Reproduced with permission from Ref. [134]. Copyright 2015, Royal Society of Chemistry

in which τ_o is the Goldschmidt tolerance factor as determined based on Eq. (10) [131]:

$$\tau = \frac{r_A + r_o}{\sqrt{2}(r_B + r_o)} \tag{10}$$

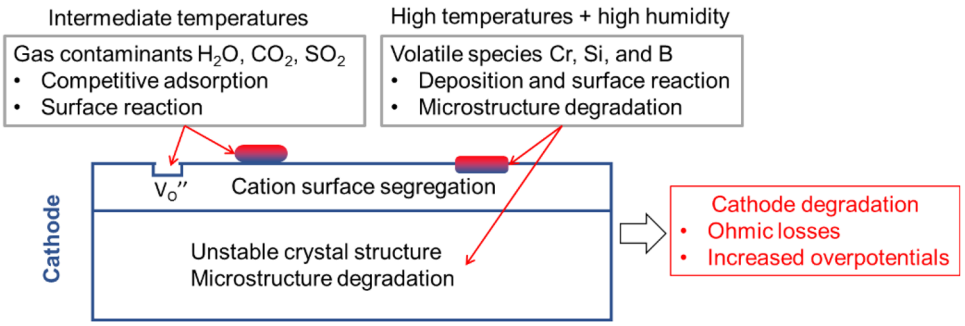

Fig. 18 Brief summary of cathode degradation modes in the presence of common contaminants

in which r_o is the radius of the anion (usually the oxygen ion).

Despite these calculations, Mogensen et al. [132] found that calculated r_c values were usually less than 1.05 Å for typical perovskite oxides and were far smaller than the size of oxygen anions (1.4 Å), suggesting that oxygen ions cannot travel through the A_2B trigonal plane as defined by the hard-sphere model. Such inconsistencies highlight the role of lattice relaxation (or constant expansion [133]) in facilitating oxygen-ion migration.

Lattice-free volume (V_f) is another parameter used to describe geometrical effects on oxygen-ion mobility. Here, V_f is defined as the volume of unoccupied ions in lattice unit cells and can be calculated using Eq. (11) [134]:

$$V_f = a^3 - \frac{4}{3}\pi\left[r_A^3 + r_B^3 + (3-\delta)r_o^3\right] \quad (11)$$

in which δ is the oxygen non-stoichiometry in the lattice.

Here, Cook et al. [135] reported that increasing V_f values from ~ 7 $Å^3$ to ~ 36 $Å^3$ can effectively reduce oxygen-ion migration activation energy from ~ 1.6 eV to ~ 0.4 eV (Fig. 17a) and Lu et al. [134] reported that the reduction of In doping content from 0.2 to 0.1 in $BaFe_{1-x}In_xO_{3-\delta}$ (x = 0.1–0.2) perovskite oxide increased free volume by ~ 0.4 $Å^3$ and therefore lowered oxygen-ion migration activation energy by nearly 0.12 eV at 900 °C (Fig. 17b). Despite these results, geometric effects on oxygen migration remain controversial in which theoretical calculations from Mayeshilba and Morgan [126] revealed no significant correlation between oxygen migration energy barrier and geometric factors such as lattice volume.

4 Cathode Degradation Mechanisms

In contrast to conventional power generation devices such as internal combustion engines, fuel cell stacks cannot be easily repaired through the simple replacement of parts, meaning extended lifetimes (i.e., more than 40,000 h operation [136] with degradation rates less than 0.2% per 1000 h operation) are essential in practical SOFC applications. Lowering the operating temperature of SOFC is an effective strategy to alleviate the potential degradation due to particle coarsening and volatile contamination at elevated temperatures. Cathode materials still face challenges in terms of (1) sustaining original structures and surfaces optimal for ORR catalysis and (2) tolerating poisoning effects from contaminants (e.g., CO_2, SO_2, humidity, chromium, boron and silicon) in ambient air and/or from other contacting fuel cell components such as interconnects and sealants. In addition, these two

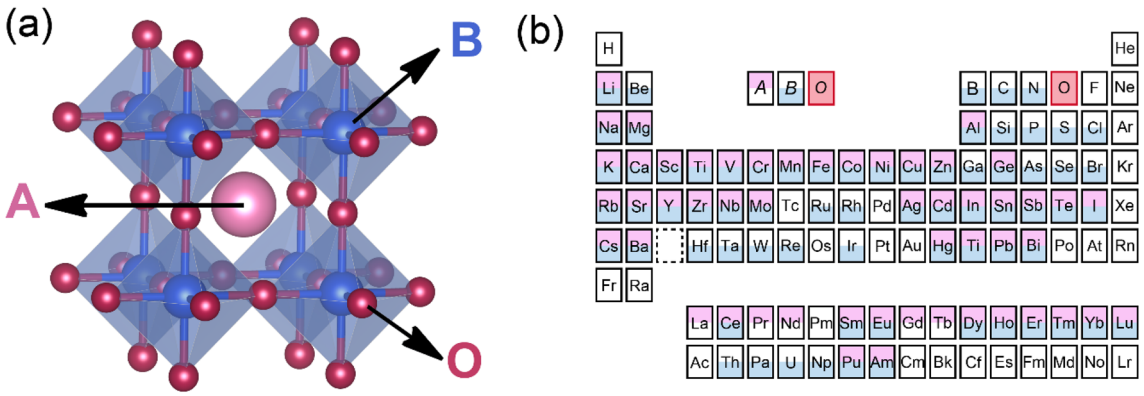

Fig. 19 **a** Schematic of a simple cubic perovskite structure of ABX_3 and **b** a summary of elements that can occupy A, B, and X-sites of perovskite materials

degradation modes are highly related to the bulk and surface of perovskite cathodes as well as their interaction with gas and solid phases in contact with cathodes and can lead to increased ohmic and kinetic loss (Fig. 18) [137].

4.1 Crystal Structure and Surface Degradation

4.1.1 Crystal Structure

The crystal structures of perovskites are essential for cathode performance because they predetermine mixed electron and oxygen-ion conductivity, cation segregation (e.g., through elastic energy minimization) and material stability. Because of this, seminal efforts have been devoted to the investigation of correlations between cathode performance and crystal structure [12, 19, 117–119, 138, 139]. Typically, high symmetry perovskite structures such as simple cubic perovskite oxide and A-site or B-site-ordered perovskites render sufficiently mixed electronic and ionic conductivities for ORR catalysis in which the Goldschmidt tolerance factor [140] is a common descriptor that can be used to predict the stability of perovskite structures with given composition. Here, the occupation of A-, B- and X-sites in perovskite materials is mainly dependent on elemental ionic size (Fig. 19) with corresponding ionic radii being easily obtained from the Shannon effective ionic radii [34]. And despite the Goldschmidt tolerance factor (Eq. 10) being an over-simplified approximation [141], it is still a practical tool to predict the trend of perovskite stability in which (1) $\tau > 1$ prefers the formation of hexagonal or tetragonal phases; (2) τ close to 1 likely leads to cubic structures; and (3) $\tau < 0.9$ allows for the easy formation of orthorhombic or rhombohedral structures.

The crystal structure of perovskites is also closely related to the interatomic distance between ions in lattices. Because of this, variations in cation oxidation state and cation and oxygen stoichiometry can lead to structural transformation at elevated temperatures and varied oxygen partial pressures. For example, the oxidation states of B-site reducible cations such as Co and Fe can easily be lowered by elevating temperatures and/or lowering oxygen partial pressures. These cations with lowered oxidation states possess increased ionic sizes, which will further decrease tolerance factors and induce phase transition from cubic phase to hexagonal (e.g., BSCF-based oxides [142]) or orthorhombic phases (e.g., brownmillerite-type structure for Sr(Co, Fe)$O_{3-\delta}$-based oxides [119, 143, 144]).

4.1.2 Surface

Driven by elastic and electrostatic interactions, cation segregation from surface to bulk generally impacts surface oxygen exchange kinetics with many studies reporting oxygen surface exchange kinetics degradation in perovskite oxides with significant Sr enrichment [17, 23, 28, 37, 145]. Here, because B-site redox cations (e.g., Co ions) are active centers facilitating oxygen surface kinetics [146], degraded surface oxygen exchange rates can be attributed to increased coverage of A-site cations and/or insulating A-site cation surface precipitates (e.g., SrO and $Sr(OH)_2$) [147]. As mentioned in Sect. 2, A-site cation segregation typically occurs at the near-surface region of perovskite oxides and thus may not significantly affect bulk oxygen-ion transport in which despite observing degraded oxygen surface kinetics, Baque et al. [148] in their study found that Sr surface enrichment did not significantly impact bulk oxygen-ion conductivity in porous $La_{0.6}Sr_{0.4}Co_{0.2}Fe_{0.8}O_{3-\delta}$ perovskite oxide after annealing at 800 °C for 50 h. As the cathode performance is closely related to both bulk oxygen-ion conductivity and oxygen surface exchange kinetics, exact relationships remain unclear between surface enrichment and overall cathode performance degradation. In addition, surface enrichment in most cases is partially driven by abundant oxygen vacancies that are also critical for efficient oxygen surface and bulk kinetics. This has been well exemplified by the volcano-shaped dependency observed by Tsvetkov et al. [23] in terms of the surface exchange kinetics of LSC-based thin films with the formation of oxygen vacancies in which although oxygen vacancies are key active sites for ORR, excessive concentrations of surface oxygen vacancies can degrade surface reactivity by accelerating Sr surface segregation. Moreover, surfaces predetermine the tolerance of cathodes against contaminants in gas phases and/or contacting fuel

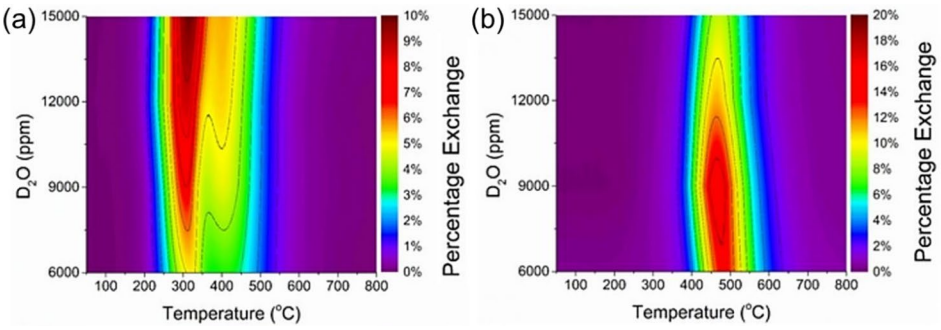

Fig. 20 **a** D_2O exchange signal and **b** O_2 exchange signal over $La_{0.6}Sr_{0.4}Co_{0.2}Fe_{0.8}O_{3-\delta}$ as a function of temperature and water content [157]

cell components [149]. More details are provided in the following subsections.

4.2 Susceptibility to Gas Contaminants

4.2.1 Water Vapor

Moisture is a common compound in ambient air and can adversely affect the durability of cathodes through the direct degradation of ORR and/or promotion of chromium [150–152] and silicon poisoning [153]. Based on this, this subsection will mainly focus on the direct effects of water vapor.

Nielsen, Hagen and Liu [154, 155] reported the strong dependency of water–vapor effects on moisture content, cathode polarization and temperature for LSM and LSCF cathodes in single-cell configurations in which for LSM-yttria-stabilized zirconia (YSZ) composite cathodes, the degradation rate of corresponding fuel cells increased with moisture content [155]. These researchers also found that cell performance degradation was more prominent at lower temperatures (e.g., 750 °C) under a high current load at 0.75 A cm^{-2} [154] but that such degradation could partially be recovered if humid air was replaced with dry air.

Water vapor can also compete against O_2 for the limited surface oxygen vacancies of perovskite oxides [156–159]. For example, by applying *operando* ^{18}O isotope exchange techniques and using deuterium oxide (D_2O) as the water vapor, Huang et al. [157] reported the existence of competitive adsorption between water and oxygen at the surface of $La_{0.6}Sr_{0.4}Co_{0.2}Fe_{0.8}O_{3-\delta}$ in which at 200–350 °C, increasing water vapor content promoted water surface exchange (Fig. 20a) but prohibited oxygen surface exchange (Fig. 20b). Alternatively, these researchers reported that this competitive adsorption phenomenon was not significant in $(La_{0.8}Sr_{0.2})_{0.95}MnO_3$ oxide, indicating a higher tolerance for humidity as compared with $La_{0.6}Sr_{0.4}Co_{0.2}Fe_{0.8}O_{3-\delta}$. This finding was consistent with results obtained by Liu et al. [160], who reported the higher tolerance of LSM as compared with LSCF in the presence of 10% humidity. In addition to degrading oxygen surface exchange rates, the competitive adsorption of water vapor can further influence oxidizing conditions and therefore the lattice geometry and electrochemical property of perovskite oxides. For example, Wang et al. [161] reported that water vapor absorption can prevent the oxidization of $La_{0.4}Sr_{0.6}Co_{0.2}Fe_{0.7}Nb_{0.1}O_{3-\delta}$ perovskite oxide, which consequently decreased lattice parameters, electrical conductivity and oxygen vacancy content. And because properties such as lattice geometry, conductivity and oxygen vacancy are dominant factors affecting surface cation segregation and ORR kinetics, the presence of water vapor can lead to complex degradation mechanisms through competitive surface adsorption with O_2.

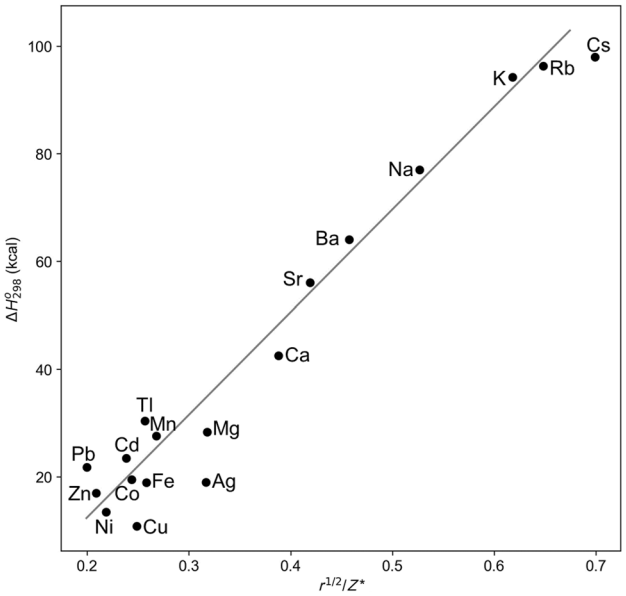

Fig. 21 Decomposition enthalpy of various carbonates against cationic property $r^{1/2}/Z^*$ at 298 K in which r denotes cation radius and Z^* is the effective nuclear charge calculated from Slater's rules [185]. Reproduced with permission from Ref. [172]. Copyright 1972, American Institute of Physics

4.2.2 CO_2 Poisoning

CO_2 is commonly present in air at concentrations of ~ 300 cm^3 m^{-3} and can strongly interact with defects such as oxygen vacancies and basic alkali and alkaline-earth element cations on the surface of perovskite oxides [13, 18, 162–167] due to acid–base interactions between acidic CO_2 and the basic nature of defects and alkali and alkaline-earth elements. As a result, even small amounts of CO_2 can compete against O_2 for limited surface reactive oxygen vacancies [168] and react with cations to form catalytically inert carbonates that can block active sites and adversely affect the crystal structure integrity of sub-surfaces [21]. Here, cathode performance degradation due to acid–base interactions can be recovered by lowering CO_2 partial pressures [13, 18, 169]; however, degradation due to carbonate formation is irreversible. In addition, the poisoning effects of CO_2 on cathode materials are more prominent at lower temperatures (< 650 °C) [158], likely arising from the increased stability of carbonate phases at reduced temperatures.

Cations are another factor that can determine anion stability. For example, Stern and Weise [170] reported that anion stability decreased with cation polarization power and suggested that cation polarization power can be used as a term to describe cation capability to distort anions and is associated with the size, charge and electronegativity of cations. In general, cations with strong polarization power possess (1) small size, (2) large positive charge and (3) high

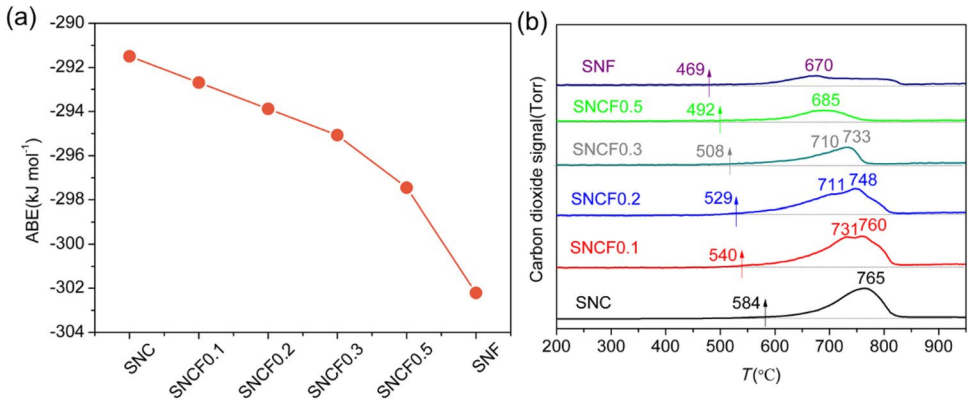

Fig. 22 (**a**) Comparison of calculated average metal–oxygen bond energy and (**b**) CO_2 temperature-programmed desorption profiles of $SrNb_{0.1}Co_{0.9-x}Fe_xO_{3-\delta}$ oxides. Reproduced with permission from Ref. [165]. Copyright 2015, Elsevier

electronegativity that is close to the anion [171]. Based on this, Stern [172] proposed $r^{1/2}/Z^*$ (r is the cation size, Z^* is the effective nuclear charge) to describe the polarization power and enthalpy of carbonate deposition at 298 K as a method to describe the thermal stability of carbonates. As a result, these researchers found a near-linear behavior between these two parameters (Fig. 21) in which relatively large-sized A-site cations were consistently more reactive with CO_2 than small-sized B-site cations and perovskite oxides containing cations such as Sr and Ba were more susceptible to CO_2 poisoning as compared with perovskite oxides containing Ca [173–176] or cations with higher oxidation states (Nb^{5+} [177, 178], Sb^{5+} [179, 180], Ta^{5+} [181, 182], Ti^{4+} [183] and Cr^{6+} [184]).

Due to strong interactions between CO_2 and A-site cations such as Sr and Ba, the lower surface coverage of those reactive cations can improve the CO_2 tolerance of perovskite oxides. The surface coverage of these cations is associated with surface segregation (Sect. 2), and the weakening of the two main driving forces (i.e., elastic and electrostatic interactions) can help to suppress surface segregation and therefore limit exposure to CO_2. Based on this, perovskite properties such as cation size, stoichiometry, crystallinity and lattice strain and cathode operating conditions such as polarization can all affect the tolerance of cathodes against CO_2 poisoning.

Based on the strong dependency of anion stability on cation polarization power, a conclusion can be made that cations possessing strong interactions with oxygen ions should also possess strong interactions with carbonate ions in which the former can affect the stability of perovskite oxides, whereas the latter can determine reactivity with CO_2, meaning that CO_2-tolerant cathodes should contain cations with optimal interactions with O^{2-} and CO_3^{2-} (i.e., strong bonding with O^{2-} but weak bonding with CO_3^{2-}). Here, interactions between metal and oxygen can be described by using average metal–oxygen energy (ABE) and an example of calculating the ABE of an ABO_3 perovskite oxide is provided by Eq. (12) [186] in which ΔH denotes formation enthalpy for A_mO_n, B_xO_y and sublimation enthalpy of A or B metals and $D_{(O_2)}$ is the dissociation energy of O_2. Possibly due to the balance of cation interactions with oxygen and carbonate, more negative ABE values strengthen metal–oxygen interactions and therefore indicate cathodes that are more CO_2 tolerant [21, 165]. For example, by varying the ratio of Co to Fe at B-sites, Zhang et al. [165] reported that the thermal stability of adsorbed CO_2 species at their perovskite surface decreased with more negative ABEs (Fig. 22).

$$\mathrm{ABE} = \frac{1}{12}\left(m\left(\Delta H_{\mathrm{A}_m\mathrm{O}_n}\right) - m\Delta H_{\mathrm{A}} - \frac{n}{2}D_{\mathrm{O}_2}\right) + \frac{1}{6}x\left(\Delta H_{\mathrm{B}_x\mathrm{O}_y} - x\Delta H_{\mathrm{B}} - \frac{y}{2}D_{\mathrm{O}_2}\right) \quad (12)$$

in which $\Delta H_{\mathrm{A(B)}_m\mathrm{O}_n}$, $\Delta H_{\mathrm{A(B)}}$ and D_{O_2} represent the formation enthalpy of $\mathrm{A(B)}_m\mathrm{O}_n$ oxide, sublimation enthalpy of A(B) metal at 25 °C and dissociation energy of oxygen ($D_{\mathrm{O}_2} = 500.2\,\mathrm{kJ \cdot mol^{-1}}$), respectively.

4.2.3 SO_2 Poisoning

Trace amounts of SO_2 (e.g., in the 1×10^{-3} cm^3 m^{-3} level) present in air can exert adverse effects (i.e., increased ohmic and polarization resistances) on the long-term stability of cathodes [187, 188]. Similar to CO_2, SO_2 is also an acidic gas that is reactive to basic cations such as Sr and Ba to form sulfate species on the surface. The formation of sulfates is an oxidization reaction (i.e., S^{4+} needs to be oxidized to S^{6+}) as represented by Eq. (13) that can easily occur at high SO_2 concentrations on cathode surfaces with abundant basic terminated AO phases, oxygen vacancies and dissociated oxygen species. For example, Wang et al. [189] reported that increasing SO_2 concentrations from 0.1 cm^3 m^{-3} to 100 cm^3 m^{-3} led to the more pronounced cathode degradation of $La_{0.6}Sr_{0.4}Co_{0.2}Fe_{0.8}O_{3-\delta}$ and that high SO_2 levels led to the further formation of $La_2O_2SO_4$ in addition to $SrSO_4$. These researchers also compared the stability of $(La, Sr)Co_{0.2}Fe_{0.8}O_{3-\delta}$ cathodes with varying La/Sr ratios in the presence of 1 cm^3 m^{-3} SO_2 at 800 °C and found

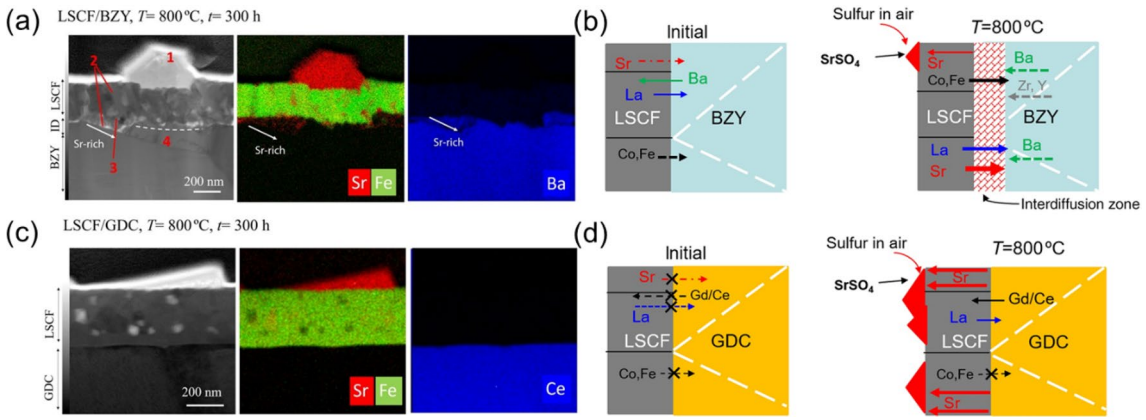

Fig. 23 Scanning transmission electron microscopy bright-field images and elemental distributions of the cross sections of $La_{0.6}Sr_{0.4}Co_{0.2}Fe_{3-\delta}$ thin films over **a** BZY and **c** GDC electrolytes. Schematics of the proposed mechanisms of $La_{0.6}Sr_{0.4}Co_{0.2}Fe_{3-\delta}$ interaction with **b** BZY and **d** GDC and their role in SO_2 poisoning. Reproduced with permission from Ref. [191]. Copyright 2018, Materials Research Society. In (**a**), label 1 denotes the $SrSO_4$ phase, label 2 denotes nanopores, label 3 denotes the interdiffusion region rich in Y and Sr, and label 4 denotes the other interdiffusion region rich in La, Co and Fe

higher coverage of the $SrSO_4$ phase over the Sr-rich perovskite oxide as compared with La-rich samples as well as immediate poisoning effects with the introduction of SO_2 [190]. Here, this trend can be explained by the promoted Sr segregation and oxygen vacancy as imparted by increasing divalent and large-sized Sr content.

$$AO + SO_2 + \frac{1}{2}O_2(g) \rightarrow ASO_4 \quad (13)$$

Cathode/electrolyte interfaces can also play a role in SO_2 tolerance. For example, De Vero et al. [191] reported the improved SO_2 tolerance of $La_{0.6}Sr_{0.4}Co_{0.2}Fe_{3-\delta}$ thin film after annealing at 800 °C for 300 h over a $BaZr_{0.8}Y_{0.2}O_{3-\delta}$ (BZY) electrolyte substrate as compared with over a $Gd_{0.1}Ce_{0.9}O_{1.95}$ (GDC) electrolyte substrate in which these researchers observed the significant interdiffusion of cations across the cathode/BZY interface (over the 1-µm-thick interdiffusion zone) but not across the cathode/GDC interface (Fig. 23a, b). Here, these researchers proposed that significant cation interdiffusion with BZY can weaken the thermodynamic driving force of Sr surface segregation and therefore hinder further $SrSO_4$ formation with SO_2 (Fig. 23 d), whereas due to limited Sr interdiffusion into GDC, Sr species in the corresponding cathode can only diffuse to the cathode/gas interface, which consequently promoted unwanted $SrSO_4$ precipitation (Fig. 23c). Based on this, these researchers postulated that easy Sr interdiffusion between cathodes and electrolytes is likely related to the similar lattice symmetries (i.e., perovskite structures for cathodes and BZY) of the cathode and the electrolyte, which can reduce cation migration energy barriers across different phases. This easy cation interdiffusion has also been commonly reported for materials with similar structures by other researchers [192–195].

4.3 Susceptibility to Volatile Contaminants

Cathode materials are also susceptible to volatile contaminants such as Cr, Si and B-based species from fuel cell components (e.g., interconnects, balance of plants, glass sealants). Although Cr, Si and B play essential roles in the tailoring of fuel cell component properties to tolerate SOFC operating conditions, they can become volatile at high temperature and humidity conditions. Therefore, one of the main motivations to lower SOFC operating temperatures is to suppress the vaporization of these elements and achieve improved long-term stability of the electrodes.

4.3.1 Chromium Poisoning

Chromium is an important element that can prevent the oxidization of metallic alloys at SOFC operating temperatures through the formation of Cr_2O_3 layers on alloy surfaces. However, chromium can also rapidly degrade cathode performance if evaporated as highly oxidized (i.e., Cr^{6+}) volatile species such as $CrO_2(OH)_2$ and CrO_3. Aside from temperature, the volatility of Cr_2O_3 is also related to water vapor and oxygen content in gases in which Gindorf et al. [196] reported that the vaporization of $CrO_2(OH)_2$ increased with increasing humidity in air at 950 °C. Water vapor partial pressure in air can also affect Cr volatile species vaporization from Cr_2O_3 in which CrO_3 (g) is dominant at low water vapor pressures (Eq. 14), whereas $CrO_2(OH)_2$ is dominant at high water vapor pressures (Eq. 15):

$$Cr_2O_3(S) + 1.5O_2(g) \rightarrow 2CrO_3(g) \quad (14)$$

$$CrO_3(g) + 1.5O_2(g) + 2H_2O(g) \rightarrow 2CrO_2(OH)_2(g) \quad (15)$$

In general, the nucleation theory can be used to explain the deposition of Cr on LSM and LSCF surfaces [197–199] and involve the deposition of volatile Cr species through chemical reactions between high-valent Cr and nucleation agents such as Mn, Co and Sr to form Cr_2O_3, $(Cr, Mn)_3O_4$, $SrCrO_3$ or $CoCr_2O_4$ on cathode surfaces. Here, the general reaction routes as summarized by Jiang and Chen [197] can be represented by Eqns. (16–18) in which N denotes Mn, Co and/or SrO species at cathode surfaces and indicate that Cr deposition kinetics is highly dependent on cathode surface chemistry, which is dominated by factors discussed in Sect. 2.

$$CrO_3(g) + N(s) \rightarrow Cr - N - O_{(nuclei)}(s) + O_2(g) \quad (16)$$

$$Cr - N - O_{(nuclei)}(s) + CrO_3(g) \rightarrow Cr_2O_3(s) \quad (17)$$

$$Cr - N - O_{(nuclei)}(s) + N + CrO_3(g) \rightarrow N - Cr - O_x(s) \quad (18)$$

4.3.2 Silicon Poisoning

Glass-based sealants used in the manufacturing of SOFCs contain silicon-based materials such as boroaluminosilicate, borosilicate, aluminosilicate and silicate [200]. In addition, silicon species are present in alloys used for high-temperature operations [201, 202]. Similar to Cr, Si species can easily generate $Si(OH)_4$ vapor at elevated temperatures, particularly with increasing water vapor pressure [203], the deposition of which on cathode surfaces can significantly degrade cathode performance by blocking oxygen-ion transport [202] and promoting perovskite phase decomposition at the near-surface region [204, 205]. For example, Perz et al. [204] observed significant performance degradation of 5.9 times in $La_{0.6}Sr_{0.4}Co_{0.2}Fe_{0.8}O_{3-\delta}$ with a cathode surface coated with 10-nm-thick SiO_2 at 700 °C for 1340 h as compared with a cathode surface without SiO_2 coating (degradation of 4.5 times in the same annealing conditions). Such degradation is related to the formation of a continuous layer of La-Sr-Si–O species on the surface and Co-Fe–O nanoparticles as promoted by SiO_2 deposition. Bucher et al. [206] also observed the decomposition of surface phases over $La_{0.6}Sr_{0.4}CoO_{3-\delta}$ oxides due to Si species deposition and highlighted the role of water vapor (relatively humidity = 30%–60%) in exacerbating Si poisoning effects in which such surface phase decompositions can degrade oxygen surface exchange kinetics and bulk diffusivities and therefore degrade cathode performance [206, 207].

4.3.3 Boron Poisoning

Boron is commonly used to tune the viscosity and soften the temperature of glass sealants [208–210]. Similar to Cr and Si contaminants however, borates become volatile at high temperatures and water pressures [211, 212] in which Zhang et al. [212] reported that borates mainly vaporize in the form of BO_2 in dry atmosphere but $B_3H_3O_6$ in humid atmosphere. Here, the deposition of volatile borate species can degrade the performance of perovskite oxides such as LSM and LSCF-based materials by inducing surface phase decomposition and accelerating particle coarsening. Based on this, Chen et al. comprehensively studied the effects of boron poisoning on LSM- [213], LSCF- [214] and BSCF-based [215] electrodes by annealing perovskite oxides in the presence of borosilicate glass at 700–800 °C for 7–30 days and found that volatile boron was highly reactive with surface La species to form $LaBO_3$, which led to the destruction of the perovskite structures. Alternatively, these researchers reported that La-free BSCF showed much-improved tolerances toward surface boron deposition, but that boron can promote A-site cation (e.g., Ba and Sr) segregation and alter the microstructure of cathodes [215]. These researchers further reported that deposited boron can serve as a sintering agent to cause the severe particle coarsening of infiltrated Gd-doped ceria nanoparticles in LSM composite cathodes and significantly degrade overall cathode performance [216].

5 Design Strategies to Develop Perovskite Cathode Materials

At SOFC operating conditions, both the surface and bulk properties of cathode materials are essential for efficient and stable ORR activity. In addition, surface and bulk interactions such as surface cation segregation are significant for the catalytic activity and long-term stability of corresponding cathodes. Considering the importance of cathode surface and bulk properties in ORR catalysis, cathode performance can be enhanced through several methods, including (1) optimizing cathode composition and structures and (2) incorporating additional functional phases. As such, this section will mainly focus on reviewing recent advancements in cathode development through doping (Sect. 5.1) and surface functionalization (Sect. 5.2).

5.1 Doping Strategy

The structural and compositional flexibility of perovskite oxides enable the tuning of corresponding bulk and surface properties through the incorporation of heterogeneous atoms at A-sites and B-sites (Table 1). Here, common doping methods in cathode development include (1) solid-state reactions

Table 1 Summary of doping strategies at A-site, B-site and A-/B-sites in typical perovskites reported in the literature

Doping method	Materials	Temperature (°C)	Performance	Mechanisms	References
A-site size mismatch	$Pr_{1-x}Nd_xBaCo_{1.6}Fe_{0.4}O_{5+\delta}$	600	With 20 mol.% Nd dopant, the peak power density is 1.34 W cm^{-2} at 600 °C, which is 109% higher than that of $PrBaCo_{1.6}Fe_{0.4}O_{5+\delta}$	Nd acting as the A-site dopant has a similar size to Pr but lower valance state, resulting in increased oxygen vacancy concentration	[219]
A-site size mismatch	$Sr_{1-x}Li_xFe_{0.8}Nb_{0.1}Ta_{0.1}O_{3-\delta}$	600	With $x=0.05$, the ASR value is 0.146 cm^2 and the peak power density is 836 mW cm^{-2}, which is ~ 160% greater than that of $SrFe_{0.8}Nb_{0.1}Ta_{0.1}O_{3-\delta}$	Size mismatch between Li (~ 0.92 Å) dopant and host Sr (1.44 Å) leads to Li segregation and A-site deficiency, which favors improved ORR activity	[19]
A-site size mismatch	$PrBa_{1-x}Ca_xCoCuO_{5+\delta}$	650–800	Reduced ASR value of 0.052 Ω cm^2 at 650 °C, increased peak power density of 2.04 W cm^{-2} at 800 °C and high stability (degradation rate = 0.053% h^{-1}) at 700 °C	Ca doping can lower A-site cation size mismatch and therefore alleviate lattice distortion, broaden PrO_δ layer space, maintain surface chemical properties and largely improve ORR activity and stability	[220]
A-site segregation	$(La_{0.7}Sr_{0.3})_{0.95}(Co_{0.2}Fe_{0.8})O_{3-\delta}$	600 and 650	Reduced ASR values of 0.037 Ω cm^2 at 650 °C and 0.1 Ω cm^2 at 600 °C and increased peak power densities of 1.4 W cm^{-2} at 650 °C and 1.0 W cm^{-2} at 600 °C	A-site deficiency in $(La_{0.7}Sr_{0.3})_{0.95}(Co_{0.2}Fe_{0.8})O_{3-\delta}$ favors the creation of a catalytically active B-site spinel phase and improved electrode performance	[221]
A-site size mismatch	$(Sr_{0.95}A_{0.05}Fe_{0.8}Nb_{0.1}Ta_{0.1}O_{3-\delta}$ (A = Li, Na, and K)	600	Li doping leads to a low ASR value of 0.12 Ω cm^2, high peak power density of 1.02 W cm^{-2} and high stability (degradation rate = ~ -8.1×10^{-12} W cm^{-2} h^{-1}) at 600 °C	Significant size mismatch between Li dopant and Sr host leads to easy Li cation migration to material surface, resulting in increased bulk A-site deficiency and oxygen vacancies	[18]
A-site exsolution	$Sr_{0.95}Ag_{0.05}Nb_{0.1}Co_{0.9}O_{3-\delta}$	500	Low ASR of ~0.214 Ω cm^2, high peak power density of 1116 mW cm^{-2} at 500 °C and high stability at a current density of 625 mA cm^{-2} for 140 h	Ag exsolved from $Sr_{0.95}Ag_{0.05}Nb_{0.1}Co_{0.9}O_{3-\delta}$ can contribute to bulk A-site cation deficiency and simultaneous surface ORR-active Ag nanoparticle formation	[222]
A-site exsolution	$La_{1-x-y}Sr_xAg_xAg_yMnO_{3-\delta}$	500–800	Ag nanoparticle exsolution for 12 h reduced ASR values by ~ 20% at 600 °C and 800 °C in 20% O_2 balanced Ar gas	Ag dopant exsolution to form ORR-active nanoparticles can improve electrochemical performance	[223]
A-site polarization power	$PrBa_{0.8}Ca_{0.2}Co_2O_{5+\delta}$	750	High CO_2 tolerance with slight increases in ASR value from ~ 0.024 Ω cm^2 to 0.028 Ω cm^2 after 1000 h in ~ 1 vol% CO_2 balanced air at 750 °C	Pr and Ca cations at A-sites with high oxidation states and/or small sizes possess high polarization power and can therefore improve CO_2 tolerance and ORR durability	[224]
B-site dopant size	$Ba_{0.5}Sr_{0.5}Fe_{1-x}Sb_xO_{3-\delta}$ ($x=0.0$, 0.05, 0.1)	700	Sb doping content of 10 mol.% can reduce ASR values from 0.213 Ω cm^2 to 0.120 Ω cm^2 at 700 °C	The larger size of Sb^{3+} (0.76 Å) than Fe^{3+} (0.645 Å) and Fe^{4+} (0.585 Å) helps to reduce the tolerance factor close to unity, which contributes to a stabler cubic structure	[225]

Table 1 (continued)

Doping method	Materials	Temperature (°C)	Performance	Mechanisms	References
B-site dopant size	$SrSc_xCo_{1-x}O_{3-\delta}$ ($x=0.0$–0.2)	600	With $x=0.1$, a reduced ASR of 0.25 Ω cm^2 at 600 °C was obtained	Large-sized Sc dopant (0.745 Å) can stabilize the cubic phase of $SrSc_{0.1}Co_{0.9}O_{3-\delta}$ and increase electrical conductivity	[226]
B-site high-valence	$SrCo_{0.85}Fe_{0.1}P_{0.05}O_{3-\delta}$	589	A reduced ASR value of 0.097 Ω cm^2 at 589 °C	P dopant can stabilize the cubic perovskite structure and increase the disordering of oxygen vacancies to result in high stability and high ORR performance	[119]
B-site high-valence	$Sm_{0.5(1-x)}Sr_{0.5(1-x)}Ba_xCo_{1-0.3x}Fe_{0.2x}Nb_{0.1x}O_{3-\delta}$ ($x=0.4$, 0.5, and 0.6)	600–900	Lower ASR value of 0.53 Ω cm^2 at 600 °C than those of $Sm_{0.5}Sr_{0.5}CoO_{3-\delta}$ (1.79 Ω cm^2) and $Ba(Co_{0.7}Fe_{0.2}Nb_{0.1})O_{3-\delta}$ (0.64 Ω cm^2), good tolerance toward Cr contaminant	Doping of Nb^{5+} effectively suppresses the surface segregation of Ba and thus improves Cr tolerance	[227]
B-site with high-valence	$Sr(Co, Ta)O_{3-\delta}$	450–700	A Ta content of 20 mol.% allowed for reduced ASR values of ~0.011–~0.78 Ω cm^2 from 700 to 450 °C	High-valence Ta dopant can help to easily change the Co valence and contribute to faster oxygen surface exchange	[117]
B-site with high-valence	$SrSc_{0.175}Nb_{0.025}Co_{0.8}O_{3-\delta}$	450–550	A low ASR value of 0.95 Ω cm^2 at 450 °C and a high peak power density of 0.91 W cm^{-2} at 550 °C	Doping Nb at the B-site can decrease oxygen vacancy migration barrier along neighboring Co sites	[11]
B-site with high-valence	$SrSc_{0.175}Ta_{0.025}Co_{0.8}O_{3-\delta}$	500–700	Reduced ASR values of 0.233, 0.033 and 0.004 Ω cm^2 at 500, 600 and 700 °C, respectively	Strong Ta–O bonds result in the low valence state of Co and higher oxygen vacancy concentrations	[138]
B-site with high-valence	$SrCo_{0.8}Nb_{0.1}Ta_{0.1}O_{3-\delta}$	450–550	Highly reduced ASR values of ~0.16 Ω cm^2 at 500 °C and ~0.68 Ω cm^2 at 450 °C, significantly increased peak power densities of 1.2 W cm^{-2} at 500 °C and 0.7 W cm^{-2} at 450 °C	The synergistic effects of Nb and Ta dopants arouse the optimal balance of oxygen vacancies, ionic mobility and surface electron transfer to promote ORR activity	[12]
B-site with high-valence	$Sr_{1-y}Ca_yFe_{1-x}Si_xO_{3-\delta}$ ($y=0$, 0.25, 0.5, 0.75 and 1; $x\leqslant0.20$)	450–800	With $x=0.15$, a lower ASR value of 0.51 Ω cm^2 was obtained as compared with undoped $Sr_{0.75}Ca_{0.25}FeO_{3-\delta}$ (0.91 Ω cm^2) at 700 °C	The doping of high-valence Si^{4+} can reduce Fe valence and thus produce more oxygen vacancies to promote ORR activity	[228]
B-site low-valence	$Ba_{0.5}Sr_{0.5}(Co_{0.8}Fe_{0.2})_{0.96}Zn_{0.04}O_{3-\delta}$	600 and 750	ASR (600 °C) = 0.23 Ω cm^2, ASR (750 °C) = 0.03 Ω cm^2, peak power density (750 °C) = 580 mW cm^{-2}	Low-valence Zn dopant can reduce the average valence of B-site cations, which favors the formation of more oxygen vacancies and promotes surface exchange and oxygen-ion migration	[229]
B-site electronegativity	SCN20 and SCT20	500–700	Obtained ASR values of SCT20 (0.092–0.097 Ω cm^2) were lower than those of SCN20 (0.21–0.24 Ω cm^2) at 550 °C	The low electronegativity of Ta dopant moves the electron cloud closer to neighboring Co centers, resulting in the relatively low oxidation state of Co and a slightly high oxygen vacancy content	[118]

Table 1 (continued)

Doping method	Materials	Temperature (°C)	Performance	Mechanisms	References
B-site changing ABE	$Bi_{0.5}Sr_{0.5}Fe_{1-x}Ti_xO_{3-\delta}$ ($x=0.05$–0.20)	700	With $x=0.15$, an ASR value of 0.085 Ω cm^2 and a peak power density of 1.41 W cm^{-2} was obtained at 700 °C along with good CO_2 tolerance and chemical stability in 15% CO_2 balanced air	Increasing Ti content from 5 mol.% to 15 mol.% can change ABE values from − 282.05 kJ mol^{-1} to − 292.79 kJ mol^{-1}, leading to strengthened metal–oxygen bonding and increased overall acidity	[230]

and (2) sol–gel methods in which the solid-state reaction route involves the mechanical mixing of metal precursors (e.g., metal oxides or carbonates), the pelletizing of powder mixtures and long-term (more than 10 h) calcination at high temperatures (e.g., 1200 °C) to enable sufficient interdiffusion between constituent ions. Despite its simplicity and versatility in perovskite synthesis, the long-term sintering procedures of solid-state reactions have limited application in obtaining products with well-controlled particle sizes. Alternatively, the sol–gel route (the so-called Pechini method) [217] requires relatively low temperatures (normally below 1000 °C) to calcine metal precursors and typically involves dissolving water-soluble metal precursors such as nitrates, complexation with agents such as EDTA and citric acid, gel formation through water evaporation, firing to form char and calcination at elevated temperatures to obtain targeted oxides. As compared with solid-state reactions, the sol–gel reactions are more uniform dispersions of metal precursors than mixtures of solids, meaning that the sol–gel method requires lower calcination temperatures and shorter calcination periods. Despite this, a major limitation of the sol–gel method is the lack of water-soluble salts such as Ta-containing precursors. Nevertheless, the sol–gel method is preferred for perovskite synthesis due to low calcination temperatures and easy control of synthesis conditions [218].

5.1.1 A-Site Doping

A-site cations in perovskites typically possess relatively large ionic sizes as compared with B-site cations and are coordinated with 12 oxygen atoms in the lattice. Common A-site cations include lanthanide elements (e.g., La, Pr, Nd, Sm and Gd) [231] and alkaline-earth elements (e.g., Ca, Sr and Ba) [232]. A-site cations can further be partially occupied by alkali metals (e.g., Li, Na and K) [18] and post-transition metals such as Bi metals [233]. And although most A-site cations are redox inactive and are not directly involved in ORR, they play an essential role in determining cathode performance and long-term stability. For example, A-site cations due to their relatively large ionic size can influence lattice spacing for B-site cations that normally sit within voids formed by A-site cations and therefore can affect the overall oxidation state of B-site cations. Perovskite surfaces are also usually enriched with A-site cations (Sect. 2 and 4) that can reduce the number of active sites for oxygen surface exchange and are prone to react with gaseous and volatile contaminants such as CO_2 and Cr species. The migration of A-site cations from bulk to surface at elevated temperatures can further dynamically change the bulk and surface properties of cathodes. Considering these effects, the rational modulation of perovskite oxide properties through A-site doping can allow for optimized cathode catalytic activity and stability.

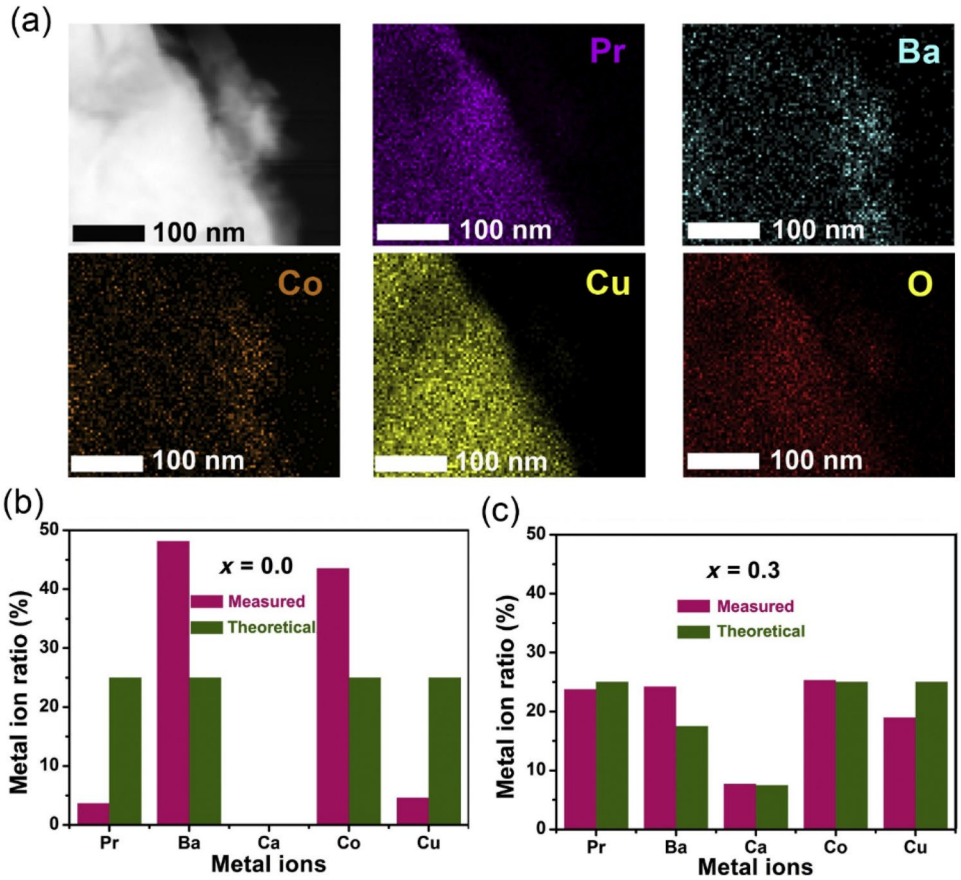

Fig. 24 **a** Energy-dispersive X-ray (EDX) images of $PrBa_{1-x}Ca_xCoCuO_{5+\delta}$, including Pr, Ba, Co, Cu and O elements. Metal cation concentrations on the surface of $PrBa_{1-x}Ca_xCoCuO_{5+\delta}$ with Ca contents of **b** $x=0$ and **c** $x=0.3$ as calculated from X-ray photoelectron spectroscopy results. Reproduced with permission from Ref. [220]. Copyright 2020, Elsevier

5.1.1.1 A-Site Cation Size The ionic size of A-site cations determines tolerance factor (τ) (Eq. 10) and thus affect perovskite structural stability [100, 234]. In addition, perovskite structures with high symmetry such as simple cubic perovskite structures generally exhibit higher mixed ionic and electronic conductivity (Sect. 3 and 4) in which high mixed conductivity is important for efficient ORR activity, especially at reduced operating temperatures (Sect. 3.2 and 3.3). Therefore, the consideration of A-site cation effects on structural symmetry is important. One typical example is our recent work [19] involving the incorporation of Li into Co-free $SrFe_{0.8}Nb_{0.1}Ta_{0.1}O_{3-\delta}$ perovskite oxide in which because Li (~0.92 Å) is much smaller than host Sr (1.44 Å), less than 5% of Li can be incorporated into the lattice to maintain the beneficial cubic structure of the perovskite. As a result, the stabilized cubic structure of $Sr_{1-x}Li_xFe_{0.8}Nb_{0.1}Ta_{0.1}O_{3-\delta}$ with $x<0.05$ together with optimal levels of oxygen vacancies and A-site deficiencies as imparted by Li doping led to improved ORR activities at 600 °C by ~ 1.6 times.

5.1.1.2 A-Site Cation Surface Segregation A-site dopant/host ionic size mismatch constitutes a major driving force (i.e., elastic energy minimization) for A-site cation surface segregation in SOFC operating conditions in which in most

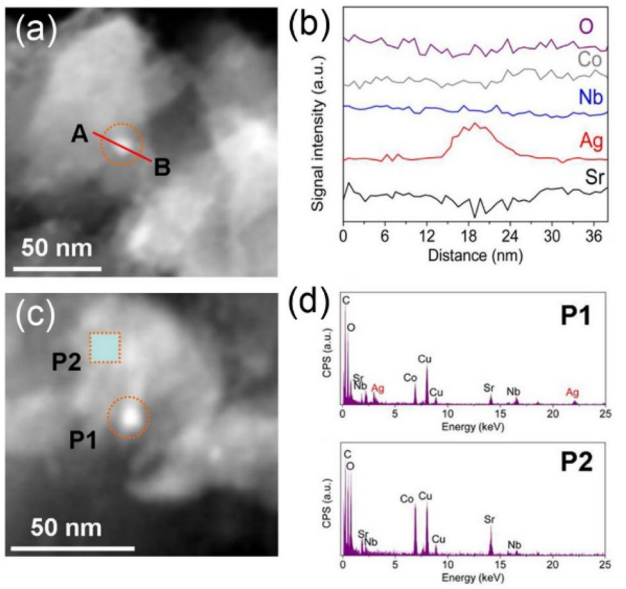

Fig. 25 **a** High-angle annular dark-field scanning transmission electron microscopy (HAADF-STEM) image of the e-SANC material with **b** corresponding liner scan file from A to B. **c** HAADF-STEM image of the s-SANC material with **d** EDX spectra at P1 and P2 positions. Reproduced with permission from Ref. [222]. Copyright 2015, American Chemical Society

cases, surface-enriched A-site cation species pose negative impacts on cathode performance and long-term stability (Sects. 2, 4). Because of this, the minimization of dopant/host size mismatch can suppress unwanted surface cation segregation [235]. For example, Pang et al. [220] highlighted the role of A-site cation size mismatch in determining ORR activity and stability for double perovskite $PrBa_{1-x}Ca_xCoCuO_{5+\delta}$ and reported that relatively low A-site cation size mismatch as achieved by $PrBa_{0.7}Ca_{0.3}CoCuO_{5+\delta}$ led to an improved ORR activity of 0.052 Ω cm^2 at 650 °C as compared with the undoped sample (0.072 Ω cm^2) and a peak power density of 2.04 W cm^{-2} at 800 °C. These researchers also found that the incorporation of Ca can effective suppress Ba surface enrichment (Fig. 24) during 100-h stability testing under 0.7 V at 700 °C. As a result, a single-cell using $PrBa_{0.7}Ca_{0.3}CoCuO_{5+\delta}$ as the cathode showed better stability (the degradation rate = 0.053% h^{-1}) than a cell using the parent oxide as the cathode (the degradation rate = 0.178% h^{-1}). And because surface-enriched A-site cations such as Sr are susceptible to contaminants such as water, vapor, CO_2 and SO_2 (Sects. 4.2 and 4.3), the suppression of surface segregation through the minimization of A-site dopant/host size mismatch can also effectively improve cathode tolerance toward these contaminants.

Alternatively, A-site cation surface segregation can create A-site deficiencies in lattices and induce the formation of oxygen vacancies to compensate charge imbalance

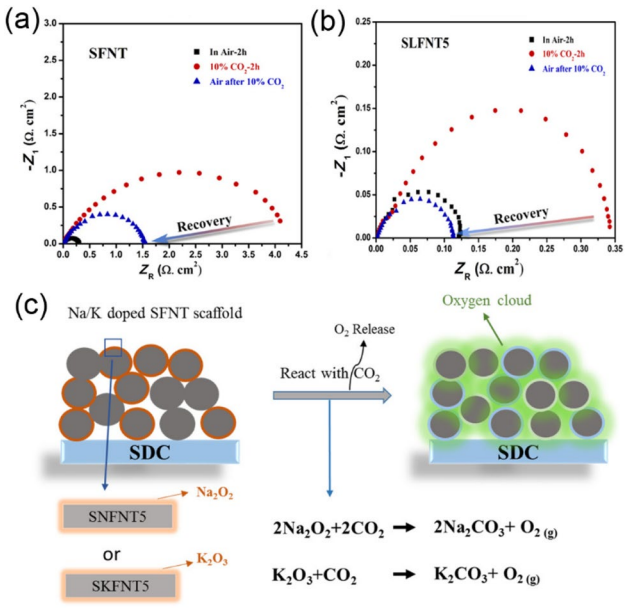

Fig. 26 Impedance spectra of **a** $SrFe_{0.8}Nb_{0.1}Ta_{0.1}O_{3-\delta}$ and **b** $Sr_{0.95}A_{0.05}Fe_{0.8}Nb_{0.1}Ta_{0.1}O_{3-\delta}$ measured in air, 10% CO_2 balanced air and the subsequent removal of CO_2 after 2 h. **c** Mechanism of oxygen cloud generation that enhanced the CO_2 tolerance of the $Sr_{0.95}A_{0.05}Fe_{0.8}Nb_{0.1}Ta_{0.1}O_{3-\delta}$ cathode. Reproduced with permission from Ref. [18]. Copyright 2019, American Chemical Society

in which A-site deficiencies and oxygen vacancies can enhance electronic and ionic conductivities [236]. For example, Celikbilek et al. [221] recently designed A-site deficiency by manipulating the composition of $(La_{0.71}Sr_{0.29})_{0.95}Co_{0.17}Fe_{0.83}O_{3-\delta}$. By introducing 5 mol.% A-site deficiency, the authors observed a low polarization resistance of 0.037 Ω cm^2 at 650 °C and 0.1 Ω cm^2 at 600 °C in a symmetrical cell, and a peak power densities of 1.4 W cm^{-2} at 650 °C and 1.0 W cm^{-2} at 600 °C in a Ni/YSZ anode-supported cell were obtained, which were much better than values obtained from a pristine $La_{0.6}Sr_{0.4}Co_{0.2}Fe_{0.8}O_{3-\delta}$ analogue. Furthermore, if enriched A-site cations such as alkali metals or noble metals do not passivate electrochemically active surfaces, A-site cation surface segregation can promote ORR activity. This was well exemplified by our recent work on alkali metal-doped $SrFe_{0.8}Nb_{0.1}Ta_{0.1}O_{3-\delta}$ [18, 19] in which significant size mismatch between the Li dopant and the Sr host allowed for the easy migration of the Li dopant from the bulk to the cathode surface, leaving a bulk with increased A-site deficiency and oxygen vacancy. Interestingly, alkali metal segregation can also suppress problematic Sr surface enrichment to further contribute to improved ORR activity and contaminant tolerance. Similarly, Zhu et al. [222] slightly reduced $Sr_{0.95}Ag_{0.05}Nb_{0.1}Co_{0.9}O_{3-\delta}$ with hydrogen to induce Ag exsolution from the bulk to the surface (Fig. 25) and created A-site cation deficiency in the bulk and ORR-active Ag nanoparticles on the surface to result in a remarkably low polarization resistance of 0.214 Ω cm^2 at 500 °C. Similar improvements resulting from A-site cation surface segregation were also reported for an Ag-doped LSM cathode [223].

Enriched A-site dopants can further functionalize cathode surfaces to resist contaminant poisoning in which our recent findings [18] highlighted alkali metals such as Na and K that can form peroxide or sesquioxide species in cathode operating conditions that can react with CO_2 to release oxygen molecules as a product and therefore increase oxygen partial pressures close to the cathode surface (Fig. 26c). Moreover, these formed alkali metal carbonates at the cathode surface are good oxygen-ion conductors that can accelerate oxygen surface exchange in the presence of CO_2 and constituted one of the major reasons for remarkable cathode ORR activity and stability improvements at 600 °C in the presence of CO_2, showing area-specific resistance (ASR) values as low as 0.12 Ω cm^2 at 600 °C and over fourfold improvement in tolerance to CO_2 poisoning (Fig. 26a, b).

5.1.1.3 Polarization Power of A-Site Cations Cation polarization power reflects the capability of cations to stabilize anions (Sect. 4.2) in which large cations with low oxidation states generally possess weaker polarization power and strong bonds with anions such as oxygen or carbonate anions. And because A-site cations (e.g., Sr and Ba) are larger

in size and have lower oxidation states than B-site cations, they are more prone to poisoning from gaseous contaminants such as CO_2 than B-site cations. Based on this, increases in A-site cation oxidation state (e.g., replacing alkaline-earth elements with lanthanides) or reductions in A-site cation size (e.g., replacing Ba or Sr with Ca) can improve the durability of corresponding cathodes in the presence of gaseous contaminants. For example, Chen et al. [224] developed a $PrBa_{0.8}Ca_{0.2}Co_2O_{5+\delta}$ double perovskite that exhibited stable ORR activity with ASR values of ~ 0.024–0.028 Ω cm^2 at 750 °C in the presence of 1 vol.% CO_2 for over 1000 h and attributed the improved durability and ORR activity to the Pr^{3+} and Ca^{2+} cations at the A-sites (high oxidation state and/or small size). Other rare-earth elements such as Eu [237], Nd and Sm [238] with high polarization powers have also been reported to be able to destabilize bonding with anions such as sulfates and carbonates to improve the contaminant tolerance of corresponding cathodes.

5.1.1.4 Inducing Effects on B-Site Cations Doping A-site cations can also impact B-site cations in perovskite oxides. A common strategy to introduce oxygen vacancies into perovskite oxides is to reduce the overall positive charge of lattices through the partial replacement of high-valence A-site cations such as La^{3+} with relatively low oxidation state dopants such as Sr^{2+} [10, 239, 240], Ba^{2+} [234, 241] and alkali metals [18, 242]. Such induced charge imbalance can be compensated by either increasing the oxidation state of B-site cations or creating oxygen vacancies. The response of perovskite oxides to the induced charge imbalance likely depends on the ease of B-site cation redox transition. For B-site cations with easy redox transitions such as Mn [243, 244] and Fe [245, 246], increases in B-site cation oxidation state are preferred and will generally lead to increased electronic conductivity due to the increased density of redox couples as charge hopping sites. As for B-site cations that are difficult to oxidize such as Co and Ni, induced charge imbalances can lead to the formation of oxygen vacancies that can enhance ionic conductivity. Increasing the size of A-site cations can also facilitate the expansion of B-site cations (i.e., be slightly reduced) to further create oxygen vacancies with a typical example being benchmark cathode BSCF in which large-sized Ba can promote oxygen vacancy formation [247]. Interestingly, although A-site cations with lower oxidation states and large ionic sizes can enhance mixed conductivity, they can also lead to weak polarization powers that increase susceptibility toward contaminants. Therefore, an optimal balance between activity and stability needs to be considered in the selection of A-site cations.

The electronegativity of A-site dopants can also affect the oxidation state of B-site cations in which relatively low electronegativities can weaken the capability of neighboring oxygen to attract electron clouds from adjacent B-site cations and slightly reduce B-site valences to promote oxygen vacancy [18] as confirmed by our recent investigation into the effects of alkali metals (i.e., Li, Na and K) on Fe valence in doped $SrFe_{0.8}Nb_{0.1}Ta_{0.1}O_{3-\delta}$ oxide. In this study, monovalent alkali metal doping not only promoted oxygen vacancies, but also reduced the average valence of B-site Fe cations in which we believed the lower electronegativity of Li (0.99), Na (0.98) and K (0.93) as compared with host Sr (1.03) [248] was the main reason for Fe valence state reduction.

5.1.2 B-Site Doping

As main ORR active centers, B-site cations play an essential role in ORR catalysis. In general, typical B-site cations in perovskite oxides are six-coordinated transition metals that include Mn [249, 250], Fe [245, 251], Ni [252] and Co [253, 254]. B-sites can also be partially occupied by a variety of elements while maintaining perovskite structural integrity, allowing for the tailoring of perovskite properties through B-site doping. Similar to A-site cations, B-site properties such as cation size, oxidation state and electronegativity can all influence the overall performance of perovskite cathodes.

5.1.2.1 Selection of B-Site Dopant Size The selection of suitable B-site dopant size is a prerequisite for successful doping in which B-site dopants should generally be comparable in size to B-site host cations to sustain perovskite structures. Here, the Shannon ionic radii of common host cations such as Mn, Fe, Co and Ni are within 0.4–0.8 Å and can serve as a criterion for the selection of potential B-site dopants. For example, Ling et al. [225] reported that the partial replacement of Fe with Sb^{3+} in $Ba_{0.5}Sr_{0.5}Fe_{1-x}Sb_xO_{3-\delta}$ ($x = 0.0$, 0.05, and 0.1) perovskite can stabilize the beneficial cubic perovskite structure by reducing the tolerance factor close to unity, resulting in the $Ba_{0.5}Sr_{0.5}Fe_{0.9}Sb_{0.1}O_{3-\delta}$ displaying significantly lowered polarization resistances from 0.213 Ω cm^2 down to 0.120 Ω cm^2 at 700 °C.

The ionic size of B-site dopants can also affect specific free volume and critical saddle point with large sizes leading to facile oxygen-ion transport (Sect. 3.1). However, the ionic size of redox-active B-site dopants can vary with oxidation state depending on A-site cations and operating conditions (e.g., temperature and gas atmosphere) and oxidation state is strongly correlated with oxygen vacancy and mobility. As a result, the understanding of the specific effects of B-site cations on saddle point free volume and size through experiments is challenging.

5.1.2.2 Doping with High Oxidation State B-Site Dopants The oxidation state of B-site cations is an important factor governing cathode ORR activity and long-term stability, and numerous studies have shown that doping

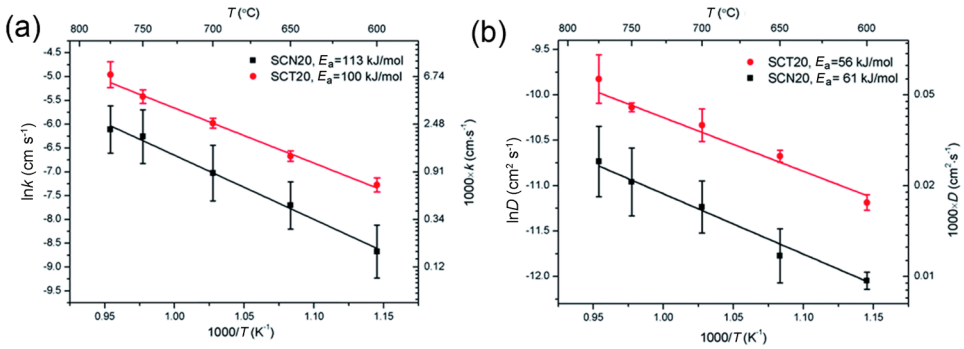

Fig. 27 **a** Oxygen surface exchange coefficient (k) and **b** oxygen-ion diffusivity (D) as a function of temperature for $SrCo_{0.8}Nb_{0.2}O_{3-\delta}$ (SCN20) and $SrCo_{0.8}Ta_{0.2}O_{3-\delta}$ (SCT20). Reproduced with permission from Ref. [118]. Copyright 2015, Royal Society of Chemistry

with high oxidation state cations such as W^{6+} [255], Mo^{6+} [256], Sb^{5+} [257], Nb^{5+} [118, 258], Ta^{5+} [13, 117], Zr^{4+} and V^{5+} [259] can effectively enhance cathode performance. According to Pauling's rules [260], high-valence B-site cations with low coordination numbers can increase electrostatic repulsion between polyhedra and stabilize high symmetry perovskite structures. Nagai and Sakon [261] also studied the effects of dopants including Ni, Cu, Zn, Cr, Fe, Al, Ga, In, Ce, Ti, Zr, Sn, V and Nb on the structural stability of $SrCoO_{3-\delta}$ and found that high-valence cations with higher solubility in lattices such as Nb^{5+} and Ti^{4+} were more effective in stabilizing the cubic structure than low-valence dopants. Interestingly, researchers have also reported that non-metals with high valences and suitable ionic sizes such as P^{5+} [262], S^{6+} [263, 264] and Si^{4+} [265] can also be applied as B-site dopants to enhance the structural stability and ORR activity of materials. We have further reported that P cation doping at the B-sites of $SrCo_{0.85}Fe_{0.1}P_{0.05}O_{3-\delta}$ can stabilize the cubic perovskite structure and prevent oxygen-vacancy ordering brownmillerite-type structure formation [119], resulting in the P-doped cathode exhibiting a low polarization resistance of 0.097 Ω cm^2 at 589 °C and no performance degradation at 600 °C for 40 h. Similar effects of these non-metal dopants were also reported by Xu et al. [266] and Luo et al. [267]

Despite their role in stabilizing structural stability, high-valence B-site dopants can reduce oxygen vacancy content in lattices due to increases in overall cation positive charge. And because oxygen vacancies are major carriers for oxygen-ion conduction (Sect. 3), high-valence B-site doping can have negative impacts on oxygen kinetics at both the surface and the bulk lattice. One method to alleviate this negative effect is to slightly lower the electronegativity of high-valence dopants. For example, one of our studies investigated the effects of Nb^{5+} and Ta^{5+} electronegativity by constraining potential effects from structural geometry and the oxidation state based on the fact that although Nb^{5+} and Ta^{5+} possessed similar sizes with the same Shannon ionic radius of 0.64 Å, they possessed different electronegativity (Ta^{5+} is slightly lower than Nb^{5+} in electronegativity) [118]. In this study, both experimental results and theoretical calculations revealed that the low electronegativity of the Ta^{5+} dopant can move electron clouds closer to neighboring Co centers to result in relatively low oxidation state Co and therefore slightly higher oxygen vacancy content, which led to enhanced oxygen surface and bulk kinetics (Fig. 27a, b) as well as cathode performance as compared with the Nb-doped counterpart. Similarly, our recent results [138] revealed that Sc^{3+} and Ta^{5+} co-doped $SrCoO_{3-\delta}$ perovskite can increase oxygen vacancy content as compared with Sc^{3+} and Nb^{5+} co-doped analogues to result in a notably lower ASR of 0.233 Ω cm^2 at 500 °C.

Reduced oxygen vacancy content should also alleviate unwanted A-site cation segregation by weakening electrostatic interactions between A-site cations and oxygen vacancies. This effect has recently been confirmed by Tsvetkov et al. [23] (Sect. 2.1 and Fig. 5). And because A-site cation segregation is a major reason for cathode susceptibility to contamination (Sect. 4), high-valence dopants can further enhance resistance to poisoning. Zhao et al. [227] also highlighted the role of Nb^{5+} doping in $Sm_{0.5(1-x)}Sr_{0.5(1-x)}Ba_xCo_{1-0.3x}Fe_{0.2x}Nb_{0.1x}O_{3-\delta}$ ($x = 0.4$, 0.5, and 0.6) in the suppression of surface Ba segregation if in contact with Fe–Cr metallic interconnects under 200 mA cm^{-2} at 900 °C for 20 h in which suppressed Ba segregation can significantly improve cathode tolerance to Cr contamination.

Although it is generally unlikely that high-valence dopants are directly involved in oxygen-ion transport, dopants can affect neighboring redox-active B-site cations. For example, Zhou et al. [11] developed a Sc^{3+} and Nb^{5+} co-doped $SrSc_{0.175}Nb_{0.025}Co_{0.8}O_{3-\delta}$ (SSNC) perovskite that showed a remarkably low ASR value of 0.95 Ω cm^2 in a symmetrical cell at 450 °C and 0.91 W cm^{-2} in a Ni-SDC|SDC based single cell at 550 °C. Here, DFT calculations revealed that oxygen vacancy formation energy was 1.007 eV for Sr_4Co_2, 2.164 eV for Sr_4CoNb and 1.906 eV for Sr_4CoSc clusters, highlighting the negative effects of Nb^{5+} on oxygen vacancy formation. Alternatively, these researchers found that oxygen migration energy barriers were significantly reduced within Sr_4Co_2 clusters close to Nb dopants (Fig. 28a-d), suggesting that improved lattice

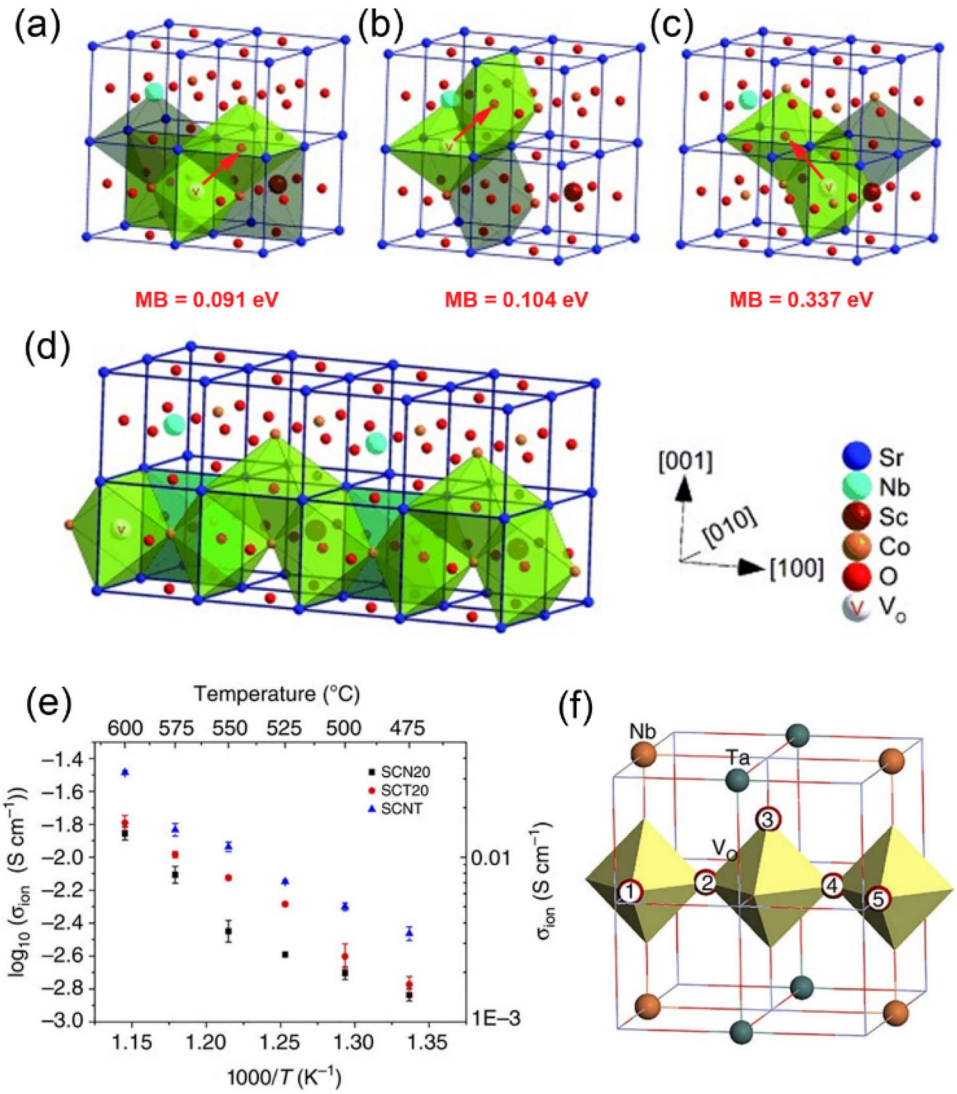

Fig. 28 Schematics of oxygen vacancy migration from **a** $V_O(Sr_4Co_2)$, **b** $V_O(Sr_4CoNb)$ and **c** $V_O(Sr_4CoSc)$ in the **d** SSNC perovskite structure. MB represents oxygen vacancy migration barrier. Reproduced with permission from Ref. [11]. Copyright 2013, Wiley–VCH. **e** Oxygen ionic conductivities of SCN20, SCT20 and SCNT from 475 to 600 °C. **f** Schematic of oxygen vacancy migration with minimum energy [12]

oxygen migration is a main contributor to enhanced ORR activity. These results also highlighted the fact that easy oxygen vacancy formation does not necessarily represent high ORR activity, especially at reduced operating temperatures. Li et al. [12] also studied Nb^{5+} and Ta^{5+} co-doped $SrCo_{0.8}Nb_{0.1}Ta_{0.1}O_{3-\delta}$ (SCNT) perovskite that showed low ASR values of ~ 0.16 Ω cm^2 at 500 °C and ~ 0.68 Ω cm^2 at 450 °C in which DFT calculations revealed that oxygen could only migrate along Co sites in the lattice (Fig. 28f). These researchers further reported that Nb^{5+} doping can enhance the density of state at the Fermi level of the next nearest Co to the dopant, which can contribute to facile charge transfer to adsorbed oxygen species. And together with the beneficial effects of Ta^{5+} in oxygen vacancy formation, the enhanced oxygen mobility and charge transfer as a result of Nb^{5+} doping allowed for an optimal balance between oxygen vacancy, oxygen-ion mobility and surface charge transfer in the resulting cathode.

Although volatile Si species can cause ORR degradation (Sect. 4.3), Si doping in perovskite lattices can effectively improve cathode performance due to benefits from its high valence. For example, Porras-Vazquez et al. [228] found that Si doping into a $Sr_{0.75}Ca_{0.25}Fe_{0.85}Si_{0.15}O_{3-\delta}$ perovskite cathode can allow for a lower polarization resistance of 0.51 Ω cm^2 than undoped $Sr_{0.75}Ca_{0.25}FeO_{3-\delta}$ (0.91 Ω cm^2) at 700 °C and that doping with high-valence Si^{4+} can reduce the average valence of Fe to lower values to introduce more oxygen vacancies close to Fe ions. These researchers also highlighted the role of cathode surfaces and bulk in determining the effects of particular elements on cathode performance in which Si interaction with surface-enriched A-site cations can result in the formation of unwanted phases that block active sites for oxygen surface exchange, whereas high-valence Si doping into cathode bulk can optimize neighboring B-site hosts to enhance cathode performance.

Table 2 Summary of cathode surface functionalization strategies

Methods	Materials with details	Temperature (°C)	Performance	Mechanisms	References
Infiltration	PrO_x infiltrated into $La_{0.6}Sr_{0.4}Co_{0.2}Fe_{0.8}O_{3-d}$-GDC composite	600–800	PrO_x reduces both polarization and ohmic resistance	PrO_x can improve charge transfer processes and increase connectivity between active and inactive interfaces at the cathode	[268]
Infiltration	$SrCo_{0.9}Ta_{0.1}O_{3-\delta}$ infiltrated into $(La_{0.6}Sr_{0.4})_{0.95}Co_{0.2}Fe_{0.8}O_{3-\delta}$-GDC composite	700–800	Infiltrated cathode showed 4.5-fold improvement in ORR activity and much better Cr tolerance	$SrCo_{0.9}Ta_{0.1}O_{3-\delta}$ is highly active for ORR and its surface has less Sr segregation, thus suppressing potential reactions between SrO and Cr species	[269]
Infiltration	SDC infiltrated into SCT15 + SDC composite	550	CO_2 tolerances improved by five times at 550 °C in the presence of 10% CO_2	SDC has stable ionic conductivity and SCT15 has stable electronic conductivity in the presence of 10% CO_2; infiltration increases the ORR-active SDC/SCT15 interface that enhances stability	[13]
Infiltration	Densified hierarchical $La_2NiO_{4+\delta}$ protected BSCF prepared through 2-step infiltration assisted with microwave plasma heating	500–700	More than twofold improvement in cathode performance in air; nearly no degradation in the presence of CO_2, whereas pristine BSCF degraded by over 20 times in 5 min	$La_2NiO_{4+\delta}$ has high surface exchange rates and is stable in the presence of CO_2; the dense thin film protects the BSCF core from CO_2 poisoning	[270]
Infiltration	$LaNi_{0.8}Fe_{0.2}O_{3-\delta}$ grown in a GDC scaffold through electrodeposition and chemically assisted electrodeposition	750	Improve Cr tolerance, no degradation at 750 °C for 300 h in the presence of Cr vapor	Low-temperature electrodeposition prevents multiple annealing procedures; $LaNi_{0.8}Fe_{0.2}O_{3-\delta}$ has a high tolerance against Cr due to the absence of Sr	[271]
Chemical vapor deposition	5-nm-thick amorphous iron oxide coating on $SrSc_{0.2}Co_{0.8}O_{3-\delta}$	700	Polarization resistances improved by 50% at 700 °C	Amorphous coating enhances the surface charge-transfer processes of the pristine cathode	[272]
Atomic layer deposition	20 nm ZrO_2 thin film with nanopores on $La_{0.6}Sr_{0.4}Co_{0.8}Fe_{0.2}O_{3-\delta}$–$Gd_{0.2}Ce_{0.8}O_{1.9}$	800	Thermal stability at 800 °C for 1100 h in which ohmic resistances improved by 1.5 times and polarization resistances improved by three times	Cation interdiffusion at the interface: Fe/Co interdiffusion into ZrO_2 improves mixed conductivity and Zr diffusion into the cathode can suppress Sr surface segregation	[273]
Atomic layer deposition	5 nm ZrO_2 coating with nanopores over 10–20 nm $La_{0.6}Sr_{0.4}Co_{O3-\delta}$ infiltrated $La_{0.80}Sr_{0.20}Ga_{0.83}Mg_{0.17}O_{3-\delta}$	700	Thermal stability at 700 °C for 4000 h in which ohmic resistances improved by 45% and polarization resistances improved by ~ 18 times	Cation interdiffusion at the interface improves mixed conductivity in the overcoat and suppresses Sr segregation to stabilize the nano-structured cathode	[274]
Atomic layer deposition	1–12-nm-thick LSC film over $La_{0.6}Sr_{0.4}Co_{0.2}Fe_{0.8}O_{3-\delta}$	600	Cathode performance improved by 45% at 600 °C and power density improved by 1.8-fold	The partially amorphous thin film can easily create oxygen vacancies that can promote oxygen surface exchange kinetics	[275]
Atomic layer deposition	Pt anchored ZrO_2 mesoporous film over a LSM-YSZ cathode backbone	750	Fuel cell power density improved by 1.5–1.7-fold at 750 °C	The Pt-ZrO_2 nanoporous composite can promote surface mixed electron and ion conductivities	[276]
Atomic layer deposition	5-nm-thick ZrO_2 coated $La_{0.6}Sr_{0.4}Co_{0.8}Fe_{0.2}O_{3-\delta}$—infiltrated GDC	650	Polarization resistance stability improved by 3.75-fold at 650 °C	$SrZrO_3$ formation at the interface can remove segregated SrO at the surface	[277]

Table 2 (continued)

Methods	Materials with details	Temperature (°C)	Performance	Mechanisms	References
Pulsed laser deposition	$Nd_{0.8}Sr_{1.2}CoO_4/Nd_{0.5}Sr_{0.5}CoO_3$ multilayers prepared by PLD, followed by annealing at 650 °C	500 and 650	Surface exchange coefficient of $Nd_{0.5}Sr_{0.5}CoO_3$ improved by ~ 100-fold	The heterostructures have consistent surface orientations that make the formation of oxygen vacancies easier at the interfacial region	[278]
Pulsed laser deposition	$La_{0.8}Sr_{0.2}CoO_3/(La_{0.5}Sr_{0.5})_2CoO_4$ vertically aligned heterostructures prepared by PLD	320–400	Surface exchange coefficient of the single-phase thin film improved by ten times at 320–400 °C	The heterostructure provides sufficient electrons for charge transfer and suppresses La and Sr surface segregation	[279]
Sputtering	Co-sputtering Y/Zr and $La_{0.6}Sr_{0.4}Co_{0.2}Fe_{0.8}O_{2.95}$ to form porous composite cathode structure	600	All sputtered 3-micron-thick thin-film SOFCs with the obtained cathodes exhibited ~ 1.7 W cm^{-2} at 600 °C	$La_{0.6}Sr_{0.4}Co_{0.2}Fe_{0.8}O_{2.95}$ sputtering leads to a dense thin film, whereas Y/Zr sputtering leads to a porous columnar structure. The co-sputtering of both can yield $YSZ/La_{0.6}Sr_{0.4}Co_{0.2}Fe_{0.8}O_{2.95}$ with high ORR-active areas	[280]
Sputtering	Sputtering Au to form 25 nm Au nanoparticles over $PrBaCo_{1.8}Cu_{0.2}O_{5+\delta}$ cathode	600–800	Polarization resistance reduced by 60% at temperatures between 600–800 °C	Doped Cu can serve as an anchor to limit the growth of Au nanoparticles at elevated temperatures and surface Au can promote oxygen surface kinetics	[281]

5.1.2.3 Modulation of ABE B-site doping can also impact average metal–oxygen bonding energy (Eq. 12) in which the strengthening of average metal–oxygen interactions can effectively improve perovskite tolerance to contaminants such as CO_2 (Sect. 4.2) [21, 165]. For example, the replacement of Co with Fe can significantly shift ABE to more negative values (Fig. 22). Gao et al. [230] also evaluated the effects of Ti^{4+} doping on the structural and electrocatalytic properties of Fe-based $Bi_{0.5}Sr_{0.5}Fe_{1-x}Ti_xO_{3-\delta}$ ($x = 0.05$–0.20) cathodes and found by increasing CO_2 content from 5 mol.% to 15 mol.%, the overall ABE value of the sample decreased from − 282.05 kJ mol^{-1} to − 292.79 kJ mol^{-1}. These researchers also reported that the strengthened metal–oxygen bonding and increased overall acidity as imparted by Ti^{4+} doping did not lead to the formation of carbonates after a BSFT0.15 cathode was treated at 700 °C for 12 h in the presence of 15% CO_2.

5.2 Surface Functionalization

The surface of perovskite oxide cathodes is an important factor determining oxygen surface exchange rate and contaminant tolerance and can potentially affect bulk properties (Sect. 2). And although the modulation of material property and operating condition through doping can indirectly modify cathode surface chemistry and microstructure, surface functionalization is a more direct method. Table 2 provides a summary of discussed strategies for cathode surface functionalization.

5.2.1 Infiltration

Infiltration (also called wet impregnation) is a popular technique to prepare cathodes and modify cathode surfaces (Fig. 29). In typical infiltration processes, the substrate is normally a porous backbone bonded with the electrolyte (Fig. 29a), in which during infiltration, a liquid solution is introduced into the substrate through coating techniques such as drop-casting (Fig. 29b). Here, liquid solutions contain precursors with desired concentrations, surfactants or additives for easy wetting and complexing agents to enhance precursor dispersion in the solution. A vacuum is also commonly introduced after coating to assist with the penetration of the solution inside the scaffold. Infiltrated samples are subsequently exposed to thermal treatment to evaporate solvents, decompose precursors and additives and strengthen backbone/infiltrate bonds to allow for the deposition of discrete particles or continuous thin films on target surfaces (Fig. 29c, d).

Advances in the application of infiltration techniques in cathode development have been comprehensively reviewed by Jiang et al. [283], Vohs and Gorte [284], Jiang et al. [285] and Ding et al. [282]. Because of this, this review

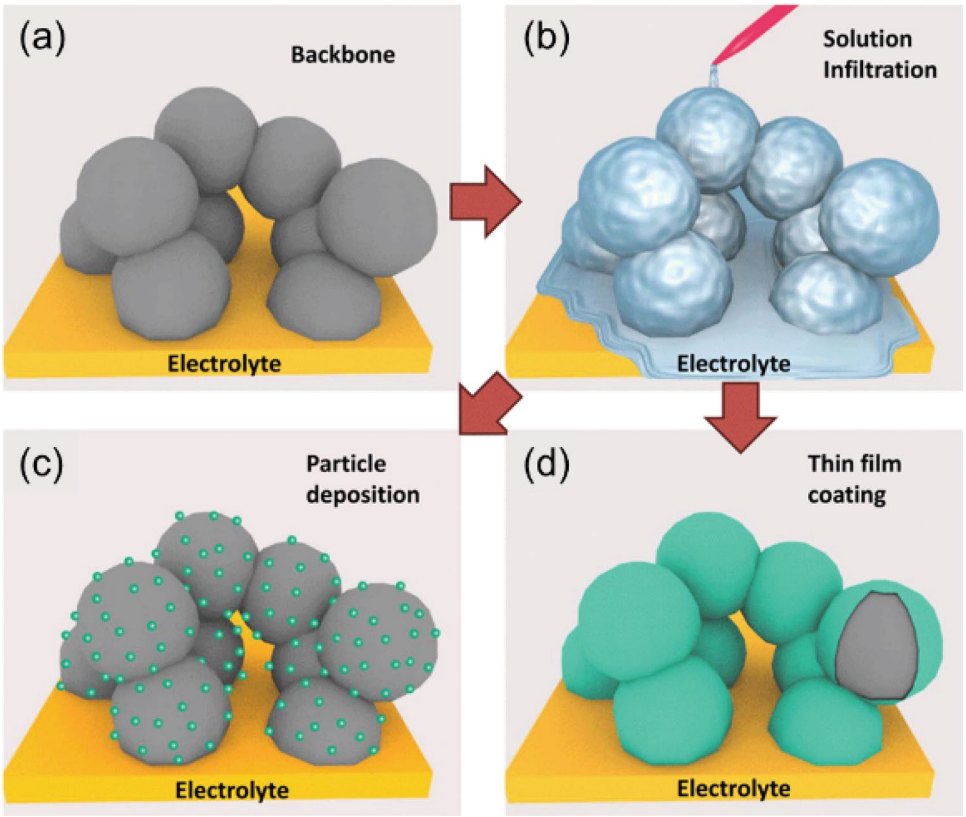

Fig. 29 Schematic of a typical infiltration process. Reproduced with permission from Ref. [282]. Copyright 2014, Royal Society of Chemistry

will provide a brief summary of advancements in the improvement of cathode ORR activity and stability through infiltration.

Large triple-phase interfaces are key to effectively lowering SOFC operating temperatures and the infiltration of either mixed-conducting materials into oxygen-ion-conducting porous scaffolds (usually made of electrolyte materials) [268, 286] or ionic-conducting materials into porous cathode backbones can extend ORR-active interfaces [287, 288]. In the case of cathode materials with sufficiently high mixed conductivities such as BSCF and $SrCo_{0.85}Ta_{0.15}O_{3-\delta}$ (SCT15), infiltrating with conventional ionic conducting materials such as doped ceria can degrade cathode ORR activity however. For example, our previous results [13] revealed that although the incorporation of SDC through both mechanical mixing and infiltration degraded the ORR activity of SCT15 in instrument air, slight improvements in activation energy from 102 kJ mol^{-1} to 96–97 kJ mol^{-1} for the SDC-infiltrated cathode were obtained (Fig. 30a). In addition, the CO_2 tolerance of the infiltrated cathode was improved by over five-fold at 550 °C in the presence of 10% CO_2 (Fig. 30b), which can be attributed to the extended ORR-active interface formed by the SCT15 and the infiltrated SDC nanoparticles in which SCT15 can sustain its electronic conductivity and SDC can sustain its ionic conductivity in 10% CO_2 (Fig. 30c).

The selection of infiltrates, scaffolds and microstructures is limited by chemical incompatibility between scaffolds and infiltrates such as La/Zr [289, 290], Sr/Zr [291, 292] and BSCF/$La_2NiO_{4+\delta}$ at temperatures higher than 900 °C [270] in which the lowering of annealing temperatures or the shortening of annealing durations are common methods used to address this challenge. For example, Zhou et al. [270] developed a novel BSCF-based cathode protected by a hierarchical conformal $La_2NiO_{4+\delta}$ dense coating through the use of microwave plasma heating that allowed for rapid heating up to 1800 °C within seconds. As a result, the infiltrated coating only required 10 min for densification and did not experience the formation of additional phases, both of which are not achievable through conventional heating processes (i.e., 850 °C for 5 h). This densification of the $La_2NiO_{4+\delta}$ shell was further demonstrated to be able to effectively improve the tolerance of the pristine BSCF cathode, resulting in only a 1.7-fold increase in polarization resistance in 10% CO_2 for the first hour (likely due to reduced oxygen partial pressure) and no degradation for the following 24 h. Similarly, Ai et al. [293] reported that their fast annealing procedure involving placing samples into a preheated furnace at 800 °C followed by rapid cooling led to a continuous shell of $La_{0.6}Sr_{0.4}Co_{0.2}Fe_{0.8}O_{3-\delta}$ infiltrate over a $La_{0.8}Sr_{0.2}MnO_3$ backbone (Fig. 31) and that the resulting dense $La_{0.6}Sr_{0.4}Co_{0.2}Fe_{0.8}O_{3-\delta}$ thin shell significantly improved the cathode performance of $La_{0.8}Sr_{0.2}MnO_3$ by

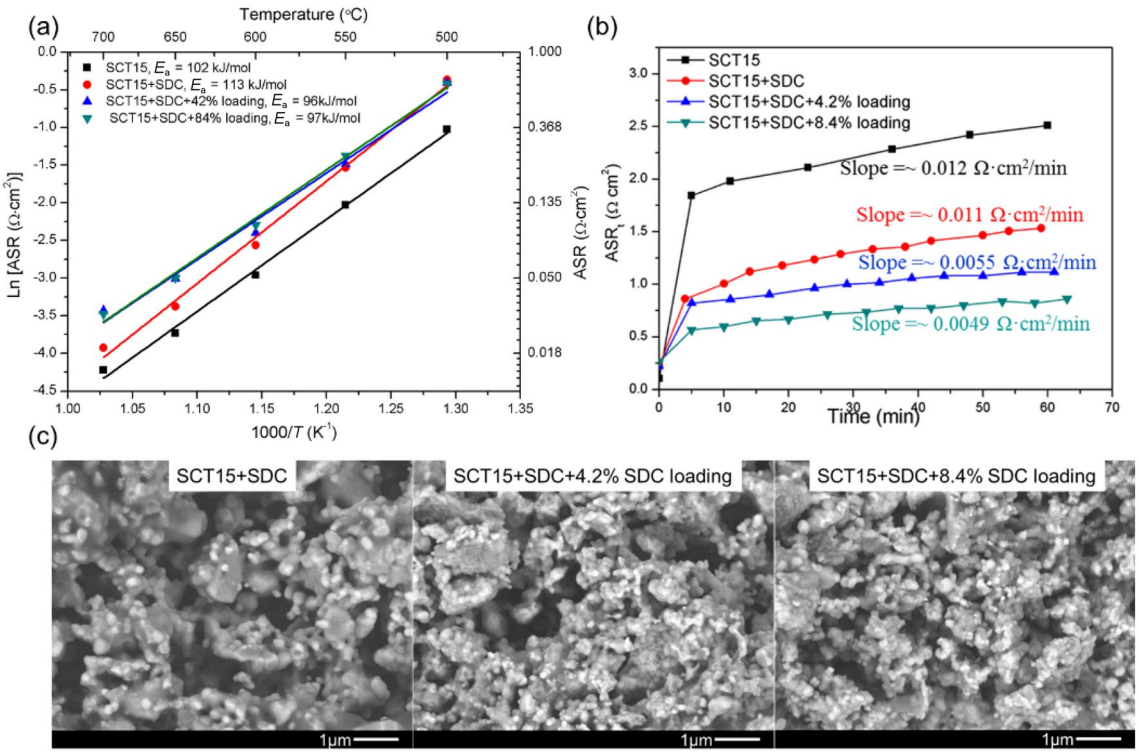

Fig. 30 Comparison of **a** polarization resistance and **b** tolerance against 10% CO_2 of SCT15, SCT15 + SDC and SCT15 + SDC infiltrated with 4.2% and 8.4% SDC nanoparticles in a symmetrical cell. **c** Back-scattered electron images of the microstructures of SCT15 + SDC, SCT15 + SDC + 4.2% infiltrated SDC and SCT15 + SDC + 8.4% infiltrated SDC cathodes. Reproduced with permission from Ref. [13]. Copyright 2017, American Chemical Society

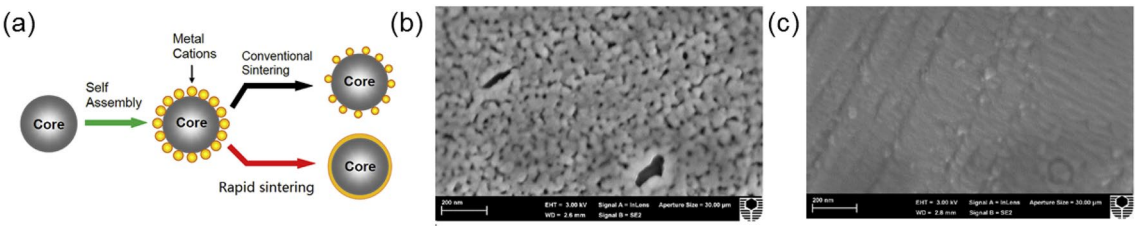

Fig. 31 **a** Schematic of the effects of annealing in determining cathode microstructure. SEM images of the LSCF infiltrate microstructure annealed through **b** conventional heating and **c** rapid heating treatments. Reproduced with permission [293], Copyright 2016, Elsevier

reducing polarization resistances from 88.2 Ω cm^2 to 2.1 Ω cm^2 at 700 °C.

Another strategy to address potentially adverse effects arising from multiple cycles of infiltration and thermal treatment is to apply electrodeposition at room temperature [252, 253, 271] in which the facilitation of electrochemical infiltration into the scaffold and the selection of suitable substrates for infiltrate deposition are key. Based on this, Lee et al. [252, 253, 271] incorporated 3D-structured carbon nanotubes into a porous scaffold through catalytic chemical vapor deposition in the presence of C_2H_4 and N_2 (50:50 vol%) at 750 °C (Fig. 31) using infiltrated cobalt nitrate as the catalyst for carbon formation. In one study involving $LaNi_{0.6}Fe_{0.4}O_{3-\delta}$ deposition for example [271] (Fig. 32), these researchers deposited Ni and Fe through co-electrodeposition in a single chamber electrolysis cell and La $(OH)_3$ through chemically assisted electrodeposition (CAED) in a typical H-cell with the cathode and anode chambers being separated by an anion exchange membrane in which the CAED technique involved the use of generated hydroxide ions (OH^-) from electrochemical nitrate reduction (Eq. 19) to form precipitates with soluble metal ions (M^{n+}) such as La and Co ions (Eq. 20). Here, the deposited precursors were thermally converted into desired oxides, which

Fig. 32 Schematic of electrochemical deposition to prepare nano-structured $LaNi_{0.6}Fe_{0.4}O_{3-\delta}$ on a $Sc_{0.1}Ce_{0.01}Zr_{0.89}O_2$ scaffold. Reproduced with permission from Ref. [271]. Copyright 2020, American Chemical Society

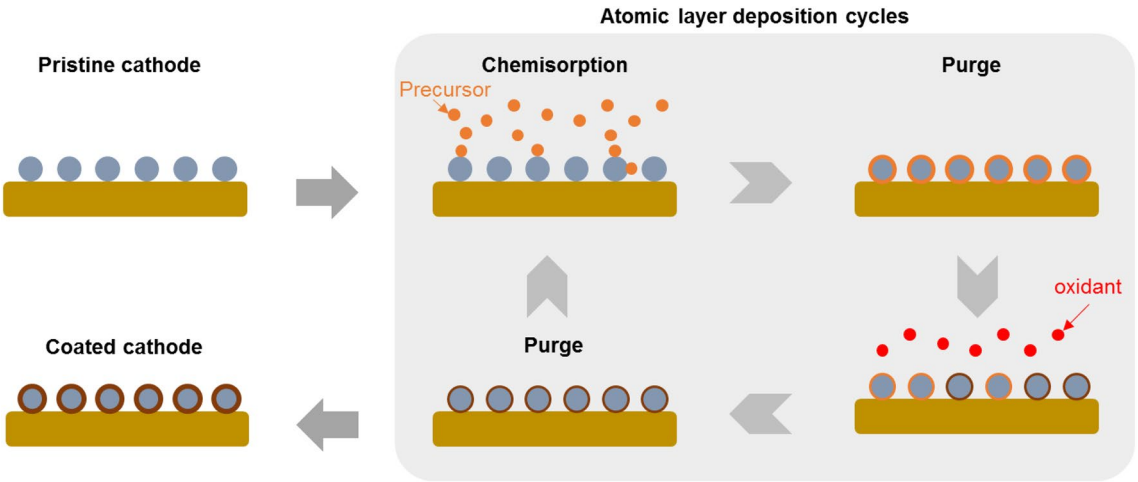

Fig. 33 Schematic of atomic layer deposition for cathode surface functionalization

avoided the long-term sintering processes of conventional infiltration techniques and therefore prevented the potential formation of insulating phases such as $La_2Zr_2O_7$. And as a result of the absence of Sr in $LaNi_{0.6}Fe_{0.4}O_{3-\delta}$, the resulting $LaNi_{0.6}Fe_{0.4}O_{3-\delta}$-GDC composite showed significant improvements against Cr poisoning and exhibited stable operations at 750 °C for 300 h in the presence of Cr vapor [271].

$$NO_3^- + H_2O + 2e^- \rightarrow NO_2^- + 2OH^- (E = 0.1\,\text{V vs. RHE}) \quad (19)$$

$$M^{n+} + nOH^- \rightarrow M(OH)_n \downarrow \quad (20)$$

5.2.2 Chemical Vapor Deposition

Chemical vapor deposition is an effective method to functionalize substrate surfaces with heterogeneous thin films through the thermally activated decomposition or reaction of precursors in vapor or gas form on substrates. However, typical chemical vapor deposition methods are not commonly

Table 3 Summary of common metal precursors used for ALD

Metal oxide for deposition	Metal precursor	Deposition temperature (K)	References
ZrO_2	Tetrakis(dimethylamido)zirconium(IV)	523	[273]
	Tetrakis(2,2,6,6-tetramethyl-3,5-heptanedionate) zirconium	523	[296]
CeO_x	TETRAKIS(2,2,6,6-tetramethyl-3,5-heptanedionato)cerium	673	[298]
SrO	BIS(2,2,6,6-tetramethyl-3,5-Heptanedionato)strontium	463	[298]
	Bis(tri-isopropyl cyclopentadienyl) strontium	473	[275]
CoO_x	Bis(cyclopentadienyl)cobalt (II)	548	[295]
	Bis(1,4-di-iso-propyl-1,4-diazabutadiene) cobalt	473	[275, 297]
	Tris(2,2,6,6-tetramethyl-3,5-heptanedionato) cobalt(III)	437	[299]
La_2O_3	Tris(2,2,6,6-tetramethyl-3,5-heptanedionato) lanthanum	523	[296]
	Tris(isopropyl cyclopentadienyl) lanthanum	473	[275]
Fe_2O_3	Ferrocene	573	[296]
NiO	Tris(2,2,6,6-tetramethyl-3,5-heptanedionato) nickel (II)	437	[299]
Al_2O_3	Trimethyl aluminum	423	[300]
PdO	Tris(2,2,6,6-tetramethyl-3,5-heptanedionato) palladium	453	[299]

used to decorate SOFC cathodes because of limited precursor penetration into cathode active surfaces inside pores. Nevertheless, Zhou et al. [272] demonstrated the effectiveness of chemical vapor deposition in promoting the cathode performance of $SrSc_{0.2}Co_{0.8}O_{3-\delta}$ by depositing 5-nm-thick amorphous iron oxide on the surface in which these researchers found that the decorated cathode demonstrated reduced polarization resistances of 50% at 700 °C and can stably operate in a fuel cell configuration for at least 250 h at 650 °C. To further address precursor transport limitations, atomic layer deposition involving evacuation (or vacuum) during deposition is also an emerging technique to decorate porous cathode surfaces.

5.2.3 Atomic Layer Deposition

Atomic layer deposition (ALD) is a thin-film deposition technique that can introduce uniform heterogeneous coatings onto cathode surfaces with similar thicknesses (so-called conformal coating). In typical ALD processes (Fig. 33), deposition usually occurs in a flow reactor in which pristine cathodes are placed in a chamber. Here, coating precursors are introduced into the chamber in vapor form and can form monolayers on the top of cathode surfaces in which as the surface becomes saturated with the precursor, excess precursor can be pumped away and other gas species can be introduced (e.g., oxidants such as water vapor or ozone) to further adsorb and condense the deposited monolayer. This process can subsequently be repeated to achieve desired film thicknesses over cathode surfaces [294]. And because precursor vapors can easily access the inner surface of porous cathodes to a depth of at least 50 μm [295] using ALD, cathode with uniform 3D hierarchal structures can be obtained [276, 295].

Based on these advantages, researchers have attempted to deposit several metal oxides onto cathodes, such as ZrO_2 [274, 276], Fe_2O_3 [296] and CoO_x [295, 297]. Table 3 summarizes common metal precursors for ALD over cathode surfaces. Here, deposition temperatures are normally kept at between 150 and 400 °C to facilitate the thermal decomposition of vapors in which insufficient temperatures may slow down reaction rates, whereas excessive temperatures may prevent the adsorption of gas species onto cathode surfaces [294].

Not all deposited films lead to enhanced ORR activity. Instead, cathodes deposited with metal oxides such as Al_2O_3 [300], ZrO_2 [273], La_2O_3 and Fe_2O_3 [296] show worse initial cathode performance than pristine cathodes, possibly due to degradation arising from either ORR-inert overlays that can block oxygen adsorption sites (e.g., ZrO_2 and Fe_2O_3 over $La_{0.8}Sr_{0.2}FeO_{3-\delta}$) [296] or chemical incompatibility between overlayers and pristine cathode materials [291]. Because of this, the careful selection of materials for overlay is important to sustain cathode performance in which because surface overlay dominates surface oxygen kinetics, materials with mixed electron and oxygen-ion conductivities that provide easy access to gases are preferred for thin film deposition. For example, Rahmanipour et al. [296] achieved improved ORR activity by co-depositing La_2O_3 and Fe_2O_3 thin films over $La_{0.8}Sr_{0.2}FeO_{3-\delta}$, whereas Chen et al. [276] introduced a conformal Pt coating onto a nanoscale ZrO_2 mesoporous medium to improve the performance of an LSM-YSZ cathode by 1.5–1.7-fold at 750 °C, which these researchers attributed to the promotion of mixed conductivity by the Pt-ZrO_2 nanocomposite. Choi et al. [275] further deposited a conformal thin LSC layer (1–12 nm) over a $La_{0.6}Sr_{0.4}Co_{0.2}Fe_{0.8}O_{3-\delta}$ cathode and reported enhanced

cathode performance (0.45 lower polarization resistance than pristine) that contributed to a 1.8-fold increase in fuel cell power density at 600 °C. These researchers also found that the deposited LSC film was partially amorphous and therefore possessed an oxygen p-band center close to the Fermi level that can contribute to improved surface oxygen kinetics.

ALD can also suppress unwanted cation segregation through cation interdiffusion at the interface between the backbone and the deposited layer and prevent the backbone cathode from thermal agglomeration. For example, Gong et al. [273] deposited a nanostructured ZrO_2 overcoat over a $La_{0.6}Sr_{0.4}Co_{0.8}Fe_{0.2}O_{3-\delta}$-$Gd_{0.2}Ce_{0.8}O_{1.9}$ composite cathode using a flow reactor in which tetrakis(dimethylamido) zirconium(IV) and water were dosed as Zr and O sources, respectively, to the cell at 250 °C and found that the ZrO_2 overcoat (~20 nm thick with nanopores, Fig. 34a) can significantly improve the overall thermal stability (ohmic and polarization resistances) of the cathode by fourfold for 1100 h at 800 °C despite the cathode with the overcoat initially showing inferior performance as compared with the pristine one. Here, these researchers proposed that cation interdiffusion (e.g., Co, Fe into ZrO_2 and Zr into the cathode) across the interface between $La_{0.6}Sr_{0.4}Co_{0.8}Fe_{0.2}O_{3-\delta}$ and the ZrO_2 overcoat can suppress Sr surface segregation over long-term annealing by alleviating electrostatic driving forces (i.e., attraction between electron holes and Sr_{La}, Fig. 34b). These researchers further used the same technique to coat 5-nm-thick ZrO_2 onto nanostructured $La_{0.6}Sr_{0.4}CoO_{3-\delta}$ infiltrated in a $La_{0.8}Sr_{0.2}Ga_{0.83}Mg_{0.17}O_{3-\delta}$ porous medium and reported significantly enhanced thermal stability at 700 °C for 4000 h (Fig. 34c) [274]. In this study, these researchers similarly claimed that interfacial cation interdiffusion can promote mixed conductivity in ZrO_2, suppress Sr surface segregation and stabilize the nanostructured cathode over long-term operation. Despite this, the potential formation of additional phases such as insulating $SrZrO_3$ [291, 292] and $BaZrO_3$ [301] between cathodes and the porous ZrO_2 film was overlooked by these studies and likely contributed to the reported degradation of initial cathode performance [273]. For example, Schmauss et al. [291] reported the formation of an unwanted $SrZrO_3$ phase between $SmCoO_{3-\delta}$ and the ZrO_2 overcoat after annealing at 750 °C for only 10 h and attributed this phase as the main reason for initial cathode performance degradation. However, these researchers also highlighted the potential benefits of $SrZrO_3$ in the suppression of Sr surface enrichment [277] and the limitation of cathode coarsening over long-term operation [291]. This significant improvement to cathode performance over long-term operation highlights the importance of nanostructure confinement and suppression of Sr surface enrichment toward cathode thermal stability.

5.2.4 Pulsed Laser Deposition

Pulsed laser deposition (PLD) is a commonly used deposition technique to prepare thin films that is particularly useful to probe the fundamental mechanisms of cathode materials at operating conditions. PLD involves the application of pulsed laser beams to excite targets in ultra-high vacuum to generate energy such as thermal, chemical and mechanical energy that can in turn generate fumes from metal targets [302]. These generated fumes can subsequently condense and form dense thin films on substrates (e.g., electrolyte or cells). PLD can also allow for the co-evaporation of multiple materials including refractory materials (e.g., Nb and Ta) and rare-earth elements in short durations [303] to synthesize ORR-active materials that contain multiple elements.

Dense thin films fabricated by using PLD can also provide a platform for the investigation of intrinsic ORR activities, surface exchange kinetics and surface cation enrichment by ruling out potential effects from the grain boundaries

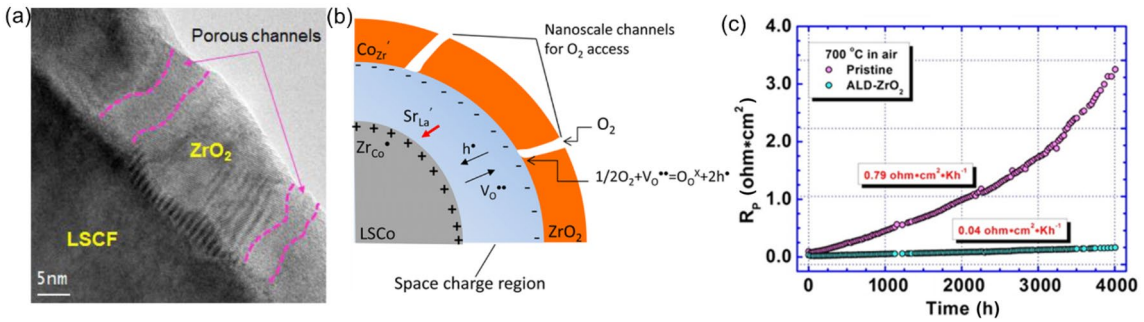

Fig. 34 **a** TEM image of ZrO_2 porous thin film deposited using ALD on $La_{0.6}Sr_{0.4}Co_{0.8}Fe_{0.2}O_{3-\delta}$. Reproduced with permission from Ref. [273]. Copyright 2013, American Chemical Society. **b** Proposed mechanism of a ZrO_2 overcoat in the enhancement of $La_{0.6}Sr_{0.4}CoO_{3-\delta}$ thermal stability. **c** Comparison of the polarization resistance between ZrO_2 coated and pristine $La_{0.6}Sr_{0.4}CoO_{3-\delta}$ cathodes in a symmetrical cell at 700 °C for 4000 h. Reproduced with permission from Ref. [274]. Copyright 2013, American Chemical Society

and microstructures of conventionally fabricated cathodes in which the surface segregation mechanisms as discussed in Sect. 2 were uncovered based on thin-film perovskite materials prepared by using PLD [20, 22, 29, 51, 54]. The selection of substrates or modifications for PLD can further affect the surface orientation of thin films [304, 305]. By varying the electrolyte substrate for example, Zhu et al. [305] deposited (110) faceted $Sr_2Sc_{0.1}Nb_{0.1}Co_{1.5}Fe_{0.3}O_{6-2\delta}$ thin films onto (100)-oriented YSZ and the (100) facet on the (100)-oriented SDC/YSZ substrate using PLD, followed by annealing at above 600 °C. The authors reported a much higher ORR activity (ASR = 30.9 Ω cm^{-2}) over (110) facets than over (100) facets (ASR = 45.6 Ω cm^{-2}) at 650 °C. The improvement of the ORR activity arises from a less Sr surface enrichment and a higher concentration of redox-active Co ions over (110) facets as compared to over (100) facets. The surface composition of the thin film cathode can also be modified after PLD deposition. For instance, Tsvetkov et al. [23] modified the deposited $La_{0.8}Sr_{0.2}CoO_3$ thin films into aqueous solutions containing metal (i.e., Co, V, Nb, Zr, Ti, Hf and Al) chloride precursors. Interestingly, the authors found an increase of cobalt oxidations states at the thin film when the surface was doped with cations such as Ti and Hf, which likely arise from the diminishment of surface oxygen vacancies. The reduced oxygen vacancy level, as imparted by surface doping, alleviates the Sr surface segregation and thus benefit the oxygen surface exchange kinetics.

The PLD also enables the formation of well-defined hetero-interfaces, which allows one to explore the roles of the heterostructures such as perovskite (e.g., LSC/RP (e.g., $(La, Sr)_2CoO_4$) phases in boosting the ORR activity [279, 306–308]. For more detailed advances in heterointerface engineering, we refer readers to the very recent review by Zhao et al. [15]. Well-defined interfaces are also beneficial in the study of the role of interfaces in long-term cathode stability. For example, Bagarinao et al. [309] studied the oxygen-ion blocking effects of $SrZrO_3$ that contributed to cathode performance degradation by an order of magnitude by intentionally depositing a ~ 20-nm-thick $SrZrO_3$ in between $La_{0.6}Sr_{0.4}CoO_{3-\delta}$ and GDC, which further clarified the negative effects of $SrZrO_3$ formation at the interfaces between Sr-containing cathodes and Zr-containing materials.

5.2.5 Sputtering

Sputtering is another deposition technique that involves the use of plasma to bombard target atoms to form vapors that can subsequently condense onto desired substrates [302]. Commonly used sputtering techniques include direct-current, radio-frequency and magnetron sputtering in which direct-current sputtering is the simplest, involving the use of direct current power to create plasma over flowing Ar. Alternatively, radio-frequency sputtering alternates current to sputter at typical frequencies between 0.5 and 30 MHz [302], whereas magnetron sputtering uses magnetic fields to create high-density plasma to accelerate sputtering rates.

Unlike PLD, sputtering can easily manipulate cathode microstructures. For example, Lee et al. [280] recently obtained a power density of ~ 1.7 W cm^{-2} at 600 °C for a 3-μm-thick all-sputtered SOFC cell with nanostructured $La_{0.6}Sr_{0.4}Co_{0.2}Fe_{0.8}O_{2.95}$/YSZ composite cathodes and suggested that the direct-current sputtering of Y/Zr alloys can allow for the easy formation of a porous columnar structured thin film (Fig. 35a), whereas the sputtering of ceramic $La_{0.6}Sr_{0.4}Co_{0.2}Fe_{0.8}O_{2.95}$ usually results in a dense thin film (Fig. 35b). These researchers also reported that the co-sputtering of both the Y/Zr alloy and the ceramic material led to a highly porous columnar structured nanocomposite (Fig. 35c). And because of the low temperatures required for the sputtering processes and the relatively low annealing temperature (600 °C), these researchers further reported the lack of insulating phases such as $SrZrO_3$ or $La_2Zr_2O_7$ forming, highlighting the advantages of sputtering in the fabrication of nanostructured composite cathodes over conventional procedures that involve high-temperature thermal treatments. In another example, Yun et al. [281] recently studied the interaction between Cu cations of a $PrBaCo_{1.8}Cu_{0.2}O_{5+\delta}$ substrate and sputtered Au nanoparticles at SOFC operating temperatures that involved Cu localization at deposited Au sites as revealed by EDS elemental mapping. And based on their results, these researchers suggested that this interaction can confine surface Au nanoparticles to ~ 25 nm to promote oxygen surface kinetics and therefore led to a ~ 60% improvement in cathode performance. In addition, Choi et al. [310] sputtered Sc stabilized ZrO_2 to successfully prevent their porous sputtered Ag electrode from thermal coarsening at below 500 °C, allowing this confinement effect as a result of the sputtered coating to contribute to a significantly improved peak power density of 59.3 mW cm^{-2} and much higher cathode stability at 0.4 V for 25 h at 450 °C as compared with bare Ag and Pt electrodes.

6 Conclusions and Perspective

The surface and bulk properties of perovskite oxides are essential for ORR activity and stability in cathodes at intermediate temperatures. The surface of cathodes determines the availability of active sites for oxygen adsorption, charge-transfer and oxygen surface migration and react dynamically to external conditions such as contacting materials (e.g., electrolytes) and contaminants (e.g., CO_2, water vapor and Cr vapor). Alternatively, cathode bulk can determine both electron and oxygen-ion conductivities that are important for efficient ORR activity at reduced temperatures. Interplay also exists between the bulk and surface of cathodes. For

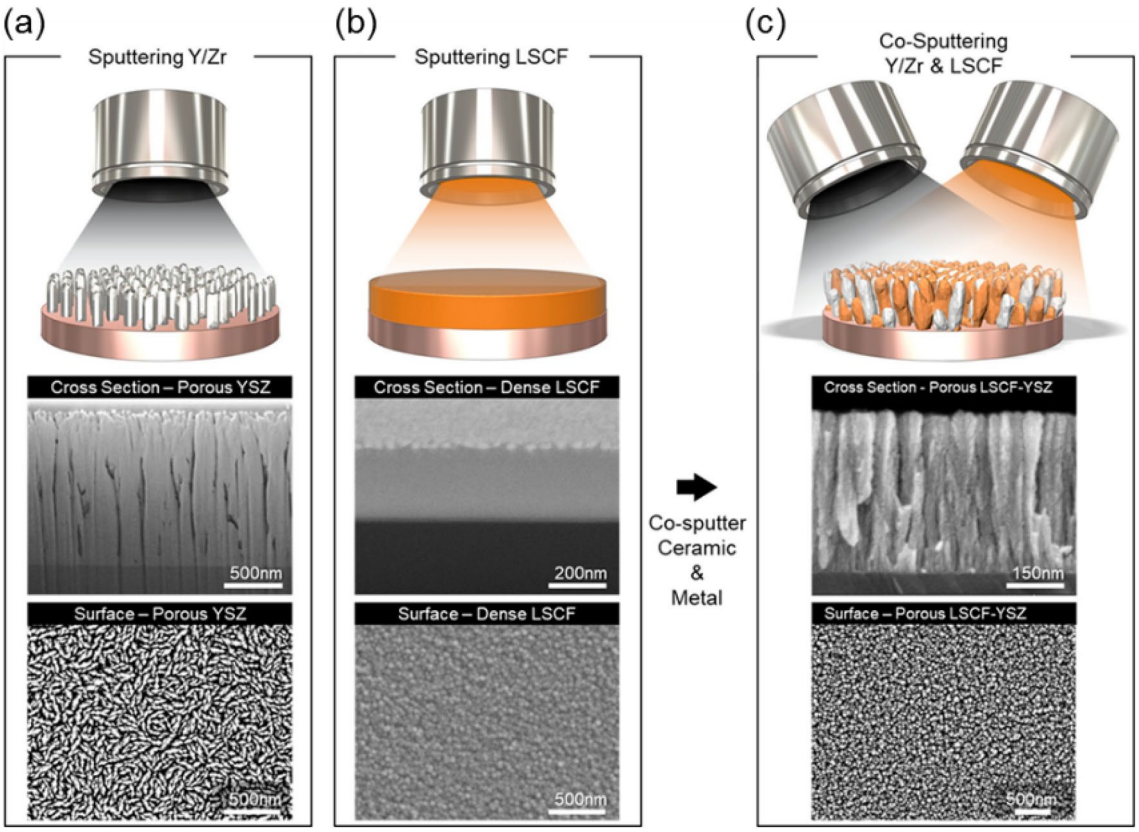

Fig. 35 Schematics of sputtering **a** metals and **b** ceramics and **c** co-sputtering metals and ceramic as well as SEM images of the corresponding cross-sections and top-view microstructures of the sputtered materials. Reproduced with permission from Ref. [280]. Copyright 2020, American Chemical Society

example, bulk properties such as increased lattice strain, cation dopant/host size mismatch and cation non-stoichiometry can all contribute to cation levels (e.g., Sr surface enrichment) and surface oxygen vacancies. Alternatively, surface oxygen vacancies as determined by lattice structures, composition and operating conditions constitute a major driving force for cation segregation from bulk and surface. Moreover, surface cation segregation can alter bulk lattice composition and consequently significantly impact bulk properties.

As such, current strategies to improve cathode performance and stability involve either the manipulation of bulk properties through doping or the introduction of heterogeneous phases through mechanical mixing or surface deposition. The key information presented in this review is as follows:

1. Cation size is essential for crystal structures, oxygen transport kinetics and cation surface segregation.
    - Increases in A-site cation size and/or decreases in B-site cation size can shift the Goldschmidt tolerance factor toward higher values to alter crystal structures from orthorhombic/rhombohedral symmetry to cubic or even hexagonal/tetragonal phases.
    - Relatively large A-site cations can increase lattice sizes to expand the ionic size of B-site redox-active cations such as Co ions and increase oxygen vacancies. Enlarged lattices can also enhance oxygen-ion migration in lattices.
    - Dopant/host size mismatch, particularly for relatively large A-site cations, can induce lattice strain that can drive dopant segregation from bulk to the surface.
2. Cation oxidation state determines crystal structure, cation surface segregation and oxygen vacancy concentration.
    - High oxidation state B-site cations (such as Nb^{5+} and Ta^{5+}) can exert strong electrostatic repulsion between adjacent octahedra and can therefore effectively stabilize beneficial cubic perovskite structures.

- Dopant/host oxidation state mismatch (e.g., Sr^{2+} dopants at La^{3+} sites) constitutes the electrostatic driving force for cation segregation.
- The introduction of low oxidation state A-site dopants such as alkaline-earth or alkali metals can either increase the oxidation state of B-site cations or induce more oxygen vacancies to compensate for overall charge imbalance. The effectiveness of this strategy to enhance oxygen vacancies is believed to depend on the redox activity of B-site cations, which has a general trend: Mn > Fe > Co > Ni.

3. Dopant electronegativity is a key factor for B-site cation states and therefore plays a vital role in ORR catalysis in which low electronegativity B-site dopants (e.g., Ta) generally lead to increased oxygen vacancies by affecting neighboring hosts such as Co.
4. The polarization power of cations is essential in determining cathode stability. Here, large-sized cations with low oxidation states normally show weaker polarization power, which will lead to strong bonding with anions such as CO_3^{2-} and explains the susceptibility of alkali-earth metals at A-sites to contaminants. However, large-sized A-site cations with low oxidation states can enhance oxygen vacancies at B-sites and therefore, increases to the bond energy between B-site cations and oxygen can enhance perovskite stability and contaminant poisoning resistance.
5. Surface modification is an effective approach to address the limitations of doping and can both increase oxygen vacancy and promote cation surface segregation in which various surface deposition methods such as infiltration, atomic layer deposition and sputtering can coat heterogeneous layers over pristine structures to result in the constraining of unwanted surface segregation, enhancement of oxygen kinetics and resistance to negative impacts from contaminants.**

In general, these strategies have multiple impacts on cathode properties, making the investigation of underlying mechanisms challenging. Nevertheless, they provide opportunities to overcome the limitations of catalyst design due to trade-offs between cathode activity and stability if single strategies are applied. A typical example involves the deposition of thin films over pristine Sr-doped perovskite surfaces to suppress Sr surface enrichment and take advantage of the beneficial effects of Sr on bulk oxygen kinetics.

Despite seminal efforts in cathode development however, the detailed relationship between ORR mechanisms and oxygen-ion transport in cathode surfaces and bulk is underexplored. However, several recent studies have reported the nonlinear relationship between ORR activity and oxygen vacancy concentration. For example, Tsvetkov et al. [23] found that surface exchange kinetics does not increase with oxygen vacancy concentration and attributed this nonlinear trend to Sr surface enrichment. Mayeshiba and Morgan [126] further calculated oxygen vacancy and mobility over an array of doped perovskites and found local nonlinear trends for samples with ORR-active elements including cobalt, nickel, iron and manganese ions at B-sites, meaning that the easy formation of oxygen vacancies may not necessarily lead to high oxygen mobility. Our results [12, 117, 118, 138] on Nb and Ta-doped perovskites also presented similar trends in which perovskite activities were much higher than BSCF but with significantly lower bulk oxygen vacancies. Overall, all of these recent experimental and theoretical findings highlight the fact that these nonlinear behaviors likely originate from both the surface and bulk properties of perovskites. Despite this, the role of cathode surfaces and bulk in overall performance remains unclear.

The rational modulation of interactions between cathode surfaces and bulk also shows promise to further improve cathode performance, particularly for cobalt-free perovskite oxides in which our team [18] demonstrated an effective method to in situ promote A-site alkali metal surface segregation so as to create A-site deficiencies in the bulk to improve electron and oxygen-ion conductivity and surface CO_2 poisoning resistance. Alkali metals themselves also present interesting behaviors at SOFC operating temperatures in which peroxides and sesquioxides of Na and K can release local oxygen partial pressures if reacting with gaseous contaminants such as CO_2.

Recent advancements in perovskite deposition techniques (e.g., atomic layer deposition, electrochemical deposition and sputtering) can further enable the practical application of nanostructured cathodes at elevated temperatures. More importantly, these techniques can be tailored to avoid potential side reactions between different phases through either the shortening of annealing durations or the reduction of annealing temperatures, both of which are not easily achievable through conventional cathode preparation methods. These techniques also hold great promise in the development of next generation composite cathodes with high density active sites and optimal porous structures.

Acknowledgements Z. Li acknowledges the financial support from the China Scholarship Council (CSC). M. Li acknowledges the financial support from the HBIS Group and the Australian Research Council (ARC) Linkage Project (LP160101729). Z. Zhu acknowledges the financial support from the ARC Discovery Projects (DP170104660 and DP190101782).

References

1. Kishimoto, M., Muroyama, H., Suzuki, S., et al.: Development of 1 kW-class ammonia-fueled solid oxide fuel cell stack. Fuel Cells **20**, 80–88 (2020)
2. Murray, E.P., Tsai, T., Barnett, S.A.: A direct-methane fuel cell with a ceria-based anode. Nature **400**, 649–651 (1999)
3. Chen, Y., deGlee, B., Tang, Y., et al.: A robust fuel cell operated on nearly dry methane at 500 °C enabled by synergistic thermal catalysis and electrocatalysis. Nat. Energy **3**, 1042–1050 (2018)
4. Hussain, A.M., Wachsman, E.D.: Liquids-to-power using low-temperature solid oxide fuel cells. Energy Technol. **7**, 20–32 (2019)
5. Gao, Z., Mogni, L.V., Miller, E.C., et al.: A perspective on low-temperature solid oxide fuel cells. Energ. Environ. Sci. **9**, 1602–1644 (2016)
6. Boldrin, P., Brandon, N.P.: Progress and outlook for solid oxide fuel cells for transportation applications. Nat. Catal. **2**, 571–577 (2019)
7. Wachsman, E.D., Lee, K.T.: Lowering the temperature of solid oxide fuel cells. Science **334**, 935–939 (2011)
8. Brett, D.J.L., Atkinson, A., Brandon, N.P., et al.: Intermediate temperature solid oxide fuel cells. Chem. Soc. Rev. **37**, 1568–1578 (2008)
9. Shao, Z., Haile, S.M.: A high-performance cathode for the next generation of solid-oxide fuel cells. Nature **431**, 170–173 (2004)
10. Choi, S., Yoo, S., Kim, J., et al.: Highly efficient and robust cathode materials for low-temperature solid oxide fuel cells: : $PrBa_{0.5}Sr_{0.5}Co_{2-x}Fe_xO_{5+\delta}$. Sci. Rep. **3**, 2426 (2013)
11. Zhou, W., Sunarso, J., Zhao, M., et al.: A highly active perovskite electrode for the oxygen reduction reaction below 600 °C. Angew. Chem. Int. Ed. **52**, 14036–14040 (2013)
12. Li, M., Zhao, M., Li, F., et al.: A niobium and tantalum co-doped perovskite cathode for solid oxide fuel cells operating below 500 °C. Nat. Commun. **8**, 13990 (2017)
13. Li, M., Zhou, W., Zhu, Z.: Highly CO_2-tolerant cathode for intermediate-temperature solid oxide fuel cells: samarium-doped ceria-protected $SrCo_{0.85}Ta_{0.15}O_{3-\delta}$ Hybrid. ACS Appl. Mater. Inter. **9**, 2326–2333 (2017)
14. Irvine, J.T.S., Neagu, D., Verbraeken, M.C., et al.: Evolution of the electrochemical interface in high-temperature fuel cells and electrolysers. Nat. Energy **1**, 15014 (2016)
15. Zhao, C., Li, Y., Zhang, W., et al.: Heterointerface engineering for enhancing the electrochemical performance of solid oxide cells. Energ. Environ. Sci. **13**, 53–85 (2020)
16. Chen, K., Jiang, S.P.: Surface segregation in solid oxide cell oxygen electrodes: phenomena, mitigation strategies and electrochemical properties. Electrochem. Energy Rev. (2020). https://doi.org/10.1007/s41918-020-00078-z
17. Koo, B., Kim, K., Kim, J.K., et al.: Sr segregation in perovskite oxides: why it happens and how it exists. Joule **2**, 1476–1499 (2018)
18. Rehman, A.U., Li, M., Knibbe, R., et al.: Enhancing oxygen reduction reaction activity and CO_2 tolerance of cathode for low-temperature solid oxide fuel cells by in situ formation of carbonates. ACS Appl. Mater. Inter. **11**, 26909–26919 (2019)
19. Rehman, A.U., Li, M., Knibbe, R., et al.: Unveiling lithium roles in cobalt-free cathodes for efficient oxygen reduction reaction below 600 °C. ChemElectroChem **6**, 5340–5348 (2019)
20. Yu, Y., Ludwig, K.F., Woicik, J.C., et al.: Effect of Sr content and strain on Sr surface segregation of $La_{1-x}Sr_xCo_{0.2}Fe_{0.8}O_{3-\delta}$ as cathode material for solid oxide fuel cells. ACS Appl. Mater. Inter. **8**, 26704–26711 (2016)
21. Yi, J., Weirich, T.E., Schroeder, M.: CO_2 corrosion and recovery of perovskite-type $BaCo_{1-x-y}Fe_xNb_yO_{3-\delta}$ membranes. J. Membr. Sci. **437**, 49–56 (2013)
22. Koo, B., Kwon, H., Kim, Y., et al.: Enhanced oxygen exchange of perovskite oxide surfaces through strain-driven chemical stabilization. Energ. Environ. Sci. **11**, 71–77 (2018)
23. Tsvetkov, N., Lu, Q., Sun, L., et al.: Improved chemical and electrochemical stability of perovskite oxides with less reducible cations at the surface. Nat. Mater. **15**, 1010–1016 (2016)
24. Anjum, U., Agarwal, M., Khan, T.S., et al.: Controlling surface cation segregation in a nanostructured double perovskite $GdBaCo_2O_{5+\delta}$ electrode for solid oxide fuel cells. Nanoscale **11**, 21404–21418 (2019)
25. Kwon, O., Sengodan, S., Kim, K., et al.: Exsolution trends and co-segregation aspects of self-grown catalyst nanoparticles in perovskites. Nat. Commun. **8**, 15967 (2017)
26. Neagu, D., Papaioannou, E.I., Ramli, W.K.W., et al.: Demonstration of chemistry at a point through restructuring and catalytic activation at anchored nanoparticles. Nat. Commun. **8**, 1855 (2017)
27. Neagu, D., Oh, T.S., Miller, D.N., et al.: Nano-socketed nickel particles with enhanced coking resistance grown in situ by redox exsolution. Nat. Commun. **6**, 8120 (2015)
28. Chen, Y., Téllez, H., Burriel, M., et al.: Segregated chemistry and structure on (001) and (100) surfaces of $(La_{1-x}Sr_x)_2CoO_4$ override the crystal anisotropy in oxygen exchange kinetics. Chem. Mater. **27**, 5436–5450 (2015)
29. Lee, W., Han, J.W., Chen, Y., et al.: Cation size mismatch and charge interactions drive dopant segregation at the surfaces of manganite perovskites. J. Am. Chem. Soc. **135**, 7909–7925 (2013)
30. Niania, M., Podor, R., Britton, T.B., et al.: In situ study of strontium segregation in $La_{0.6}Sr_{0.4}Co_{0.2}Fe_{0.8}O_{3-\delta}$ in ambient atmospheres using high-temperature environmental scanning electron microscopy. J. Mater. Chem. A **6**, 14120–14135 (2018)
31. Neagu, D., Tsekouras, G., Miller, D.N., et al.: In situ growth of nanoparticles through control of non-stoichiometry. Nat. Chem. **5**, 916–923 (2013)
32. Neagu, D., Kyriakou, V., Roiban, I.L, et al.: In situ observation of nanoparticle exsolution from perovskite oxides: from atomic scale mechanistic insight to nanostructure tailoring. ACS Nano **13**, 12996–13005 (2019)
33. Li, Y., Zhang, W., Zheng, Y., et al.: Controlling cation segregation in perovskite-based electrodes for high electro-catalytic activity and durability. Chem. Soc. Rev. **46**, 6345–6378 (2017)
34. Shannon, R.: Revised effective ionic radii and systematic studies of interatomic distances in halides and chalcogenides. Acta Crystallogr. Sect. A **32**, 751–767 (1976)
35. Kim, D., Bliem, R., Hess, F., et al.: Electrochemical polarization dependence of the elastic and electrostatic driving forces to aliovalent dopant segregation on $LaMnO_3$. J. Am. Chem. Soc. **142**, 3548–3563 (2020)
36. Porotnikova, N.M., Eremin, V.A., Farlenkov, A.S., et al.: Effect of AO segregation on catalytical activity of $La_{0.7}A_{0.3}MnO_{3\pm\delta}$ (A = Ca, Sr, Ba) regarding oxygen reduction reaction. Catal. Lett. **148**, 2839–2847 (2018)
37. Cai, Z., Kubicek, M., Fleig, J., et al.: Chemical heterogeneities on $La_{0.6}Sr_{0.4}CoO_{3-\delta}$ thin films: correlations to cathode surface activity and stability. Chem. Mater. **24**, 1116–1127 (2012)
38. Choi, M., Ibrahim, I.A.M., Kim, K., et al.: Engineering of charged defects at perovskite oxide surfaces for exceptionally stable solid oxide fuel cell electrodes. ACS Appl. Mater. Inter. **12**, 21494–21504 (2020)
39. Kwon, H., Lee, W., Han, J.W.: Suppressing cation segregation on lanthanum-based perovskite oxides to enhance the stability of solid oxide fuel cell cathodes. RSC Adv. **6**, 69782–69789 (2016)

40. Jin, T., Lu, K.: Surface and interface behaviors of $(La_{0.8}Sr_{0.2})_xMnO_3$ air electrode for solid oxide cells. J. Power Sources **196**, 8331–8339 (2011)
41. Lee, W., Yildiz, B.: Factors that influence cation segregation at the surfaces of perovskite oxides. ECS Trans. **57**, 2115–2123 (2013)
42. Abernathy, H., Finklea, H.O., Mebane, D.S., et al.: Examination of the mechanism for the reversible aging behavior at open circuit when changing the operating temperature of $(La_{0.8}Sr_{0.2})_{0.95}MnO_3$ electrodes. Solid State Ionics **272**, 144–154 (2015)
43. Pang, S., Yang, G., Jiang, X., et al.: Insight into tuning the surface and bulk microstructure of perovskite catalyst through control of cation non-stoichiometry. J. Catal. **381**, 408–414 (2020)
44. Xu, C., Du, H., Van der Torren, A.J.H., et al.: Formation mechanism of Ruddlesden–Popper-type antiphase boundaries during the kinetically limited growth of Sr rich $SrTiO_3$ thin films. Sci. Rep. **6**, 38296 (2016)
45. Tomkiewicz, A.C., Tamimi, M.A., Huq, A., et al.: Is the surface oxygen exchange rate linked to bulk ion diffusivity in mixed conducting Ruddlesden–Popper phases? Faraday Discuss. **182**, 113–127 (2015)
46. Wu, K.T., Téllez, H., Druce, J., et al.: Surface chemistry and restructuring in thin-film $La_{n+1}Ni_nO_{3n+1}$ (n = 1, 2 and 3) Ruddlesden–Popper oxides. J. Mater. Chem. A **5**, 9003–9013 (2017)
47. Siemons, W., Koster, G., Yamamoto, H., et al.: Origin of charge density at $LaAlO_3$ on $SrTiO_3$ heterointerfaces: possibility of intrinsic doping. Phys. Rev. Lett. **98**, 196802 (2007)
48. Hamada, I., Uozumi, A., Morikawa, Y., et al.: A density functional theory study of self-regenerating catalysts $LaFe_{1-x}M_xO_{3-y}$ (M = Pd, Rh, Pt). J. Am. Chem. Soc. **133**, 18506–18509 (2011)
49. Pişkin, F., Bliem, R., Yildiz, B.: Effect of crystal orientation on the segregation of aliovalent dopants at the surface of $La_{0.6}Sr_{0.4}CoO_3$. J. Mater. Chem. A **6**, 14136–14145 (2018)
50. Kim, K.J., Han, H., Defferriere, T., et al.: Facet-dependent in situ growth of nanoparticles in epitaxial thin films: the role of interfacial energy. J. Am. Chem. Soc. **141**, 7509–7517 (2019)
51. Van den Bosch, C.A.M., Cavallaro, A., Moreno, R., et al.: Revealing strain effects on the chemical composition of perovskite oxide thin films surface, bulk, and interfaces. Adv. Mater. Interfaces **7**, 1901440 (2020)
52. Cai, Z., Kuru, Y., Han, J.W., et al.: Surface electronic structure transitions at high temperature on perovskite oxides: the case of strained $La_{0.8}Sr_{0.2}CoO_3$ thin films. J. Am. Chem. Soc. **133**, 17696–17704 (2011)
53. Jalili, H., Han, J.W., Kuru, Y., et al.: New insights into the strain coupling to surface chemistry, electronic structure, and reactivity of $La_{0.7}Sr_{0.3}MnO_3$. J. Phys. Chem. Lett. **2**, 801–807 (2011)
54. Ding, H., Virkar, A.V., Liu, M., et al.: Suppression of Sr surface segregation in $La_{1-x}Sr_xCo_{1-y}Fe_yO_{3-\delta}$: a first principles study. Phys. Chem. Chem. Phys. **15**, 489–496 (2013)
55. Bachelet, R., Sánchez, F., Palomares, F.J., et al.: Atomically flat SrO-terminated $SrTiO_3$(001) substrate. Appl. Phys. Lett. **95**, 141915 (2009)
56. Crumlin, E.J., Mutoro, E., Hong, W.T., et al.: In situ ambient pressure X-ray photoelectron spectroscopy of cobalt perovskite surfaces under cathodic polarization at high temperatures. J. Phys. Chem. C **117**, 16087–16094 (2013)
57. Wen, Y., Yang, T., Lee, D., et al.: Temporal and thermal evolutions of surface Sr-segregation in pristine and atomic layer deposition modified $La_{0.6}Sr_{0.4}CoO_{3-\delta}$ epitaxial films. J. Mater. Chem. A **6**, 24378–24388 (2018)
58. Kubicek, M., Rupp, G.M., Huber, S., et al.: Cation diffusion in $La_{0.6}Sr_{0.4}CoO_{3-\delta}$ below 800 °C and its relevance for Sr segregation. Phys. Chem. Chem. Phys. **16**, 2715–2726 (2014)
59. Lai, K.Y., Manthiram, A.: Evolution of exsolved nanoparticles on a perovskite oxide surface during a redox process. Chem. Mater. **30**, 2838–2847 (2018)
60. Sharma, V., Mahapatra, M.K., Krishnan, S., et al.: Effects of moisture on (La, A)MnO_3 (A = Ca, Sr, and Ba) solid oxide fuel cell cathodes: a first-principles and experimental study. J. Mater. Chem. A **4**, 5605–5615 (2016)
61. Zhu, L., Wei, B., Lü, Z., et al.: Performance degradation of double-perovskite $PrBaCo_2O_{5+\delta}$ oxygen electrode in CO_2 containing atmospheres. Appl. Surf. Sci. **416**, 649–655 (2017)
62. Mutoro, E., Crumlin, E.J., Pöpke, H., et al.: Reversible compositional control of oxide surfaces by electrochemical potentials. J. Phys. Chem. Lett. **3**, 40–44 (2012)
63. Baumann, F.S., Fleig, J.R., Konuma, M., et al.: Strong performance improvement of $La_{0.6}Sr_{0.4}Co_{0.8}Fe0_2O_{3-\delta}$ SOFC cathodes by electrochemical activation. J. Electrochem. Soc. **152**, A2074 (2005)
64. Chen, K., Li, N., Ai, N., et al.: Polarization-induced interface and Sr segregation of in situ assembled $La_{0.6}Sr_{0.4}Co_{0.2}Fe_{0.8}O_{3-\delta}$ electrodes on Y_2O_3–ZrO_2 electrolyte of solid oxide fuel cells. ACS Appl. Mater. Inter. **8**, 31729–31737 (2016)
65. lao GJ, Savinell RF, Shao-Horn Y, : Activity enhancement of dense strontium-doped lanthanum manganite thin films under cathodic polarization: a combined AES and XPS study. J. Electrochem. Soc. **156**, B771 (2009)
66. Jiang, S.P.: Activation, microstructure, and polarization of solid oxide fuel cell cathodes. J. Solid State Electrochem. **11**, 93–102 (2007)
67. Huber, A.K., Falk, M., Rohnke, M., et al.: In situ study of activation and de-activation of LSM fuel cell cathodes-electrochemistry and surface analysis ofthin-film electrodes. J. Catal. **294**, 79–88 (2012)
68. Huber, A.K., Falk, M., Rohnke, M., et al.: In situ study of electrochemical activation and surface segregation of the SOFC electrode material $La_{0.75}Sr_{0.25}Cr_{0.5}Mn_{0.5}O_{3\pm\delta}$. Phys. Chem. Chem. Phys. **14**, 751–758 (2012)
69. Adler, S.B.: Factors governing oxygen reduction in solid oxide fuel cell cathodes. Chem. Rev. **104**, 4791–4844 (2004)
70. Wang, L., Merkle, R., Mastrikov, Y.A., et al.: Oxygen exchange kinetics on solid oxide fuel cell cathode materials-general trends and their mechanistic interpretation. J. Mater. Res. **27**, 2000–2008 (2012)
71. Mastrikov, Y.A., Merkle, R., Heifets, E., et al.: Pathways for oxygen incorporation in mixed conducting perovskites: a DFT-based mechanistic analysis for (La, Sr)$MnO_{3-\delta}$. J. Phys. Chem. C **114**, 3017–3027 (2010)
72. Nakamura, T., Oike, R., Ling, Y., et al.: The determining factor for interstitial oxygen formation in Ruddlesden–Popper type La_2NiO_4-based oxides. Phys. Chem. Chem. Phys. **18**, 1564–1569 (2016)
73. Xu, S., Jacobs, R., Morgan, D.: Factors controlling oxygen interstitial diffusion in the Ruddlesden–Popper oxide $La_{2-x}Sr_xNiO_{4+\delta}$. Chem. Mater. **30**, 7166–7177 (2018)
74. Tarasova, N., Animitsa, I., Galisheva, A., et al.: Protonic transport in the new phases $BaLaIn_{0.9}M_{0.1}O_{4.05}$ (M = Ti, Zr) with Ruddlesden–Popper structure. Solid State Sci. **101**, 106121 (2020)
75. Vielstich, W., Gasteiger, H.A., Yokokawa H.: Harumi Yokokawa: Handbook of Fuel Cells: Advances in Electrocatalysis, Materials, Diagnostics and Durability. Wiley, Hoboken (2009)
76. Chatzichristodoulou, C., Norby, P., Hendriksen, P.V., et al.: Size of oxide vacancies in fluorite and perovskite structured oxides. J. Electroceram. **34**, 100–107 (2015)
77. Joo, J.H., Merkle, R., Maier, J.: Effects of water on oxygen surface exchange and degradation of mixed conducting perovskites. J. Power Sources **196**, 7495–7499 (2011)

78. Zhang, Z., Xu, X., Zhang, J., et al.: Silver-doped strontium niobium cobaltite as a new perovskite-type ceramic membrane for oxygen separation. J. Membr. Sci. **563**, 617–624 (2018)
79. Zomorrodian, A., Salamati, H., Lu, Z., et al.: Electrical conductivity of epitaxial $La_{0.6}Sr_{0.4}Co_{0.2}Fe_{0.8}O_{3-\delta}$ thin films grown by pulsed laser deposition. Int. J. Hydrogen Energy **35**, 12443–12448 (2010)
80. Armstrong, E.N., Duncan, K.L., Wachsman, E.D.: Effect of A and B-site cations on surface exchange coefficient for ABO_3 perovskite materials. Phys. Chem. Chem. Phys. **15**, 2298–2308 (2013)
81. Ciucci, F.: Electrical conductivity relaxation measurements: Statistical investigations using sensitivity analysis, optimal experimental design and ECRTOOLS. Solid State Ionics **239**, 28–40 (2013)
82. Chen, D., Shao, Z.: Surface exchange and bulk diffusion properties of $Ba_{0.5}Sr_{0.5}Co_{0.8}Fe_{0.2}O_{3-\delta}$ mixed conductor. Int. J. Hydrogen Energy **36**, 6948–6956 (2011)
83. Ananyev, M.V., Porotnikova, N.M., Kurumchin, E.K.: Influence of strontium content on the oxygen surface exchange kinetics and oxygen diffusion in $La_{1-x}Sr_xCoO_{3-\delta}$ oxides. Solid State Ionics **341**, 115052 (2019)
84. Metlenko, V., Jung, W., Bishop, S.R., et al.: Oxygen diffusion and surface exchange in the mixed conducting oxides $SrTi_{1-y}FeyO_{3-\delta}$. Phys. Chem. Chem. Phys. **18**, 29495–29505 (2016)
85. Li, M., Niu, H., Druce, J., et al.: A CO_2-tolerant perovskite oxide with high oxide ion and electronic conductivity. Adv. Mater. **32**, 1905200 (2020)
86. Yang, T., Jin, X., Huang, K.: Transport properties of $SrCo_{0.9}Nb_{0.1}O_{3-\delta}$ and $SrCo_{0.9}Ta_{0.1}O_{3-\delta}$ mixed conductors determined by combined oxygen permeation measurement and phenomenological modeling. J. Membr. Sci. **568**, 47–54 (2018)
87. Zhang, J., Zhang, Z., Chen, Y., et al.: Materials design for ceramic oxygen permeation membranes: single perovskite vs. single/double perovskite composite, a case study of tungsten-doped barium strontium cobalt ferrite. J. Membr. Sci. **566**, 278–287 (2018)
88. Lu, Y., Zhao, H., Chang, X., et al.: Novel cobalt-free $BaFe_{1-x}Gd_xO_{3-\delta}$ perovskite membranes for oxygen separation. J. Mater. Chem. A **4**, 10454–10466 (2016)
89. Liu, B., Sunarso, J., Zhang, Y., et al.: Highly oxygen non-stoichiometric $BaSc_{0.25}Co_{0.75}O_{3-\delta}$ as a high-performance cathode for intermediate-temperature solid oxide fuel cells. ChemElectroChem **5**, 785–792 (2018)
90. Zhang, S., Wang, H., Lu, M.Y., et al.: Cobalt-substituted $SrTi_{0.3}Fe_{0.7}O_{3-\delta}$: a stable high-performance oxygen electrode material for intermediate-temperature solid oxide electrochemical cells. Eng. Environ. Sci. **11**, 1870–1879 (2018)
91. De Souza, R.A., Kilner, J.A.: Oxygen transport in $La_{1-x}Sr_xMn_{1-y}Co_yO_{3\pm\delta}$ perovskites: part II. Oxygen surface exchange. Solid State Ionics **126**, 153–161 (1999)
92. Bian, L., Wang, L., Duan, C., et al.: Co-free $La_{0.6}Sr_{0.4}Fe_{0.9}Nb_{0.1}O_{3-\delta}$ symmetric electrode for hydrogen and carbon monoxide solid oxide fuel cell. Int. J. Hydrogen Energy **44**, 32210–32218 (2019)
93. Zhou, N., Yin, Y., Li, J., et al.: A robust high performance cobalt-free oxygen electrode $La_{0.5}Sr_{0.5}Fe_{0.8}Cu_{0.15}Nb_{0.05}O_{3-\delta}$ for reversible solid oxide electrochemical cell. J. Power Sources **340**, 373–379 (2017)
94. He, G., Baumann, S., Liang, F., et al.: Phase stability and oxygen permeability of Fe-based $BaFe_{0.9}Mg_{0.05}X_{0.05}O_3$ (X = Zr, Ce, Ca) membranes for air separation. Sep. Purif. Technol. **220**, 176–182 (2019)
95. Gu, H., Zheng, Y., Ran, R., et al.: Synthesis and assessment of $La_{0.8}Sr_{0.2}ScyMn_{1-y}O_{3-\delta}$ as cathodes for solid-oxide fuel cells on scandium-stabilized zirconia electrolyte. J. Power Sources **183**, 471–478 (2008)
96. Gan, L., Ye, L., Liu, M., et al.: A scandium-doped manganate anode for a proton-conducting solid oxide steam electrolyzer. RSC Adv. **6**, 641–647 (2016)
97. Richter, J., Holtappels, P., Graule, T., et al.: Materials design for perovskite SOFC cathodes. Monatsh. Chem. **140**, 985–999 (2009)
98. Halder, S., Sheikh, M.S., Ghosh, B., et al.: Electronic structure and electrical conduction by polaron hopping mechanism in A_2LuTaO_6 (A = Ba, Sr, Ca) double perovskite oxides. Ceram. Int. **43**, 11097–11108 (2017)
99. Piao, J., Sun, K., Zhang, N., et al.: Preparation and characterization of $Pr_{1-x}Sr_xFeO_3$ cathode material for intermediate temperature solid oxide fuel cells. J. Power Sources **172**, 633–640 (2007)
100. Ding, X., Gao, X., Zhu, W., et al.: Electrode redox properties of $Ba_{1-x}La_xFeO_{3-\delta}$ as cobalt free cathode materials for intermediate-temperature SOFCs. Int. J. Hydrogen Energy **39**, 12092–12100 (2014)
101. Raccah, P.M., Goodenough, J.B.: First-order localized-electron ⇆ collective-electron transition in $LaCoO_3$. Phys. Rev. **155**, 932–943 (1967)
102. Zhou, S., Miao, X., Zhao, X., et al.: Engineering electrocatalytic activity in nanosized perovskite cobaltite through surface spin-state transition. Nat. Commun. **7**, 11510 (2016)
103. Altin, S., Aksan, M.A., Bayri, A.: High temperature spin state transitions in misfit-layered $Ca_3Co_4O_9$. J. Alloys Compd. **587**, 40–44 (2014)
104. Mahato, N., Banerjee, A., Gupta, A., et al.: Progress in material selection for solid oxide fuel cell technology: a review. Prog. Mater Sci. **72**, 141–337 (2015)
105. Patrakeev, M.V., Bahteeva, J.A., Mitberg, E.B., et al.: Electron/hole and ion transport in $La_{1-x}Sr_xFeO_{3-\delta}$. J. Solid State Chem. **172**, 219–231 (2003)
106. Mizusaki, J., Sasamoto, T., Cannon, W.R., et al.: Electronic conductivity, seebeck coefficient, and defect structure of $La_{1-x}Sr_xFeO_3$ (x = 0.l, 0.25). J. Am. Ceram. Soc. **66**, 247–252 (1983)
107. Orikasa, Y., Ina, T., Nakao, T., et al.: An X-ray absorption spectroscopic study on mixed conductive $La_{0.6}Sr_{0.4}Co_{0.8}Fe_{0.2}O_{3-\delta}$ cathodes. I. Electrical conductivity and electronic structure. Phys. Chem. Chem. Phys. **13**, 16637–16643 (2011)
108. Wærnhus, I., Grande, T., Wiik, K.: Surface exchange of oxygen in $La_{1-x}Sr_xFeO_{3-\delta}$ (x = 0, 0.1). Top. Catal. **54**, 1009 (2011)
109. Merkulov, O.V., Naumovich, E.N., Patrakeev, M.V., et al.: Defect formation, ordering, and transport in $SrFe_{1-x}Si_xO_{3-\delta}$ (x = 0.05–0.20). J. Solid State Electrochem. **22**, 727–737 (2018)
110. Olsson, E., Cottom, J., Aparicio-Anglès, X., et al.: Computational study of the mixed B-site perovskite $SmB_xCo_{1-x}O_{3-d}$ (B = Mn, Fe, Ni, Cu) for next generation solid oxide fuel cell cathodes. Phys. Chem. Chem. Phys. **21**, 9407–9418 (2019)
111. Li, Q., Deng, Y., Zhu, Y., et al.: Structural stability of Lanthanum-based oxygen-deficient perovskites in redox catalysis: a density functional theory study. Catal. Today **347**, 142–149 (2020)
112. Roohandeh, T., Saievar-Iranizad, E.: Ni- and Cu-doping effects on formation and migration energies of oxygen vacancies in $Ba_{0.5}Sr_{0.5}Fe_{1-x}(Cu/Ni)_xO_{3-\delta}$ perovskites: a DFT + U study. Appl. Phys. A **125**, 552 (2019)
113. Muñoz-García, A.B., Ritzmann, A.M., Pavone, M., et al.: Oxygen Transport in perovskite-type solid oxide fuel cell materials: insights from quantum mechanics. Acc. Chem. Res. **47**, 3340–3348 (2014)
114. Lee, D., Kim, D., Son, S.J., et al.: Simultaneous A- and B-site substituted double perovskite ($AA'B_2O_{5+\delta}$) as a new

high-performance and redox-stable anode material for solid oxide fuel cells. J. Power Sources **434**, 226743 (2019)
115. Merkle, R., Mastrikov, Y.A., Kotomin, E.A., et al.: First principles calculations of oxygen vacancy formation and migration in $Ba_{1-x}Sr_xCo_{1-y}Fe_yO_{3-\delta}$ perovskites. J. Electrochem. Soc. **159**, B219–B226 (2011)
116. Ji, Q., Bi, L., Zhang, J., et al.: The role of oxygen vacancies of ABO_3 perovskite oxides in the oxygen reduction reaction. Eng. Environ. Sci. **13**, 1408–1428 (2020)
117. Li, M., Zhou, W., Zhu, Z.: Comparative studies of $SrCo_{1-x}Ta_xO_{3-\delta}$ ($x = 0.05$–0.4) oxides as cathodes for low-temperature solid-oxide fuel cells. ChemElectroChem **2**, 1331–1338 (2015)
118. Li, M., Zhou, W., Peterson, V.K., et al.: A comparative study of $SrCo_{0.8}Nb_{0.2}O_{3-\delta}$ and $SrCo_{0.8}Ta_{0.2}O_{3-\delta}$ as low-temperature solid oxide fuel cell cathodes: effect of non-geometry factors on the oxygen reduction reaction. J. Mater. Chem. A **3**, 24064–24070 (2015)
119. Li, M., Zhou, W., Xu, X., et al.: $SrCo_{0.85}Fe_{0.1}P_{0.05}O_{3-\delta}$ perovskite as a cathode for intermediate-temperature solid oxide fuel cells. J. Mater. Chem. A **1**, 13632–13639 (2013)
120. Grunbaum, N., Mogni, L., Prado, F., et al.: Phase equilibrium and electrical conductivity of $SrCo_{0.8}Fe_{0.2}O_{3-\delta}$. J. Solid State Chem. **177**, 2350–2357 (2004)
121. Baijnath, T.P., Basu, S.: Cobalt and molybdenum co-doped $Ca_2Fe_2O_5$ cathode for solid oxide fuel cell. Int. J. Hydrogen Energy **44**, 10059–10070 (2019)
122. Jeen, H., Choi, W.S., Freeland, J.W., et al.: Topotactic phase transformation of the brownmillerite $SrCo_{0.25}$ to the perovskite $SrCoO_{3-\delta}$. Adv. Mater. **25**, 3651–3656 (2013)
123. Ding, X., Gao, Z., Ding, D., et al.: Cation deficiency enabled fast oxygen reduction reaction for a novel SOFC cathode with promoted CO_2 tolerance. Appl. Catal. **243**, 546–555 (2019)
124. Chen, T., Pang, S., Shen, X., et al.: Evaluation of Ba-deficient $PrBa_{1-x}Fe_2O_{5+\delta}$ oxides as cathode materials for intermediate-temperature solid oxide fuel cells. RSC Adv. **6**, 13829–13836 (2016)
125. Zhu, J., Liu, G., Liu, Z., et al.: Unprecedented perovskite oxyfluoride membranes with high-efficiency oxygen ion transport paths for low-temperature oxygen permeation. Adv. Mater. **28**, 3511–3515 (2016)
126. Mayeshiba, T.T., Morgan, D.D.: Factors controlling oxygen migration barriers in perovskites. Solid State Ionics **296**, 71–77 (2016)
127. Shaula, A.L., Pivak, Y.V., Waerenborgh, J.C., et al.: Ionic conductivity of brownmillerite-type calcium ferrite under oxidizing conditions. Solid State Ionics **177**, 2923–2930 (2006)
128. Kharton, V.V., Marozau, I.P., Vyshatko, N.P., et al.: Oxygen ionic conduction in brownmillerite $CaAl_{0.5}Fe_{0.5}O_{2.5+\delta}$. Mater. Res. Bull. **38**, 773–782 (2003)
129. Nikonov, A.V., Kuterbekov, K., Bekmyrza, K.Z., et al.: A brief review of conductivity and thermal expansion of perovskite-related oxides for SOFC cathode. EurAsian J. Phys. Funct. Mater. **2**, 274–292 (2018)
130. Kilner, J.A., Brook, R.J.: A study of oxygen ion conductivity in doped non-stoichiometric oxides. Solid State Ionics **6**, 237–252 (1982)
131. Xu, N., Zhao, H., Zhou, X., et al.: Dependence of critical radius of the cubic perovskite ABO_3 oxides on the radius of A- and B-site cations. Int. J. Hydrogen Energy **35**, 7295–7301 (2010)
132. Mogensen, M., Lybye, D., Bonanos, N., et al.: Factors controlling the oxide ion conductivity of fluorite and perovskite structured oxides. Solid State Ionics **174**, 279–286 (2004)
133. Dou, L., Wong, A.B., Yu, Y., et al.: Atomically thin two-dimensional organic-inorganic hybrid perovskites. Science **349**, 1518–1521 (2015)
134. Lu, Y., Zhao, H., Cheng, X., et al.: Investigation of In-doped $BaFeO_{3-\delta}$ perovskite-type oxygen permeable membranes. J. Mater. Chem. A **3**, 6202–6214 (2015)
135. Cook, R.L.: Investigations on $BaTh_{0.9}Gd_{0.1}O_3$ as an intermediate temperature fuel cell solid electrolyte. J. Electrochem. Soc. **139**, L19 (1992)
136. Chou, Y.S., Stevenson, J.W., Choi, J.P.: Long-term evaluation of solid oxide fuel cell candidate materials in a 3-cell generic short stack fixture, Part II: sealing glass stability, microstructure and interfacial reactions. J. Power Sources **250**, 166–173 (2014)
137. Aphale, A., Liang, C., Hu, B., et al.: Chapter 6-cathode degradation from airborne contaminants in solid oxide fuel cells: a review. In: Brandon, N.P., Ruiz-Trejo, E., Boldrin, P. (eds.) Solid Oxide Fuel Cell Lifetime Reliab, pp. 101–119. Academic Press, New York (2017)
138. Xu, X., Zhao, J., Li, M., et al.: Sc and Ta-doped $SrCoO_{3-\delta}$ perovskite as a high-performance cathode for solid oxide fuel cells. Compos. B **178**, 107491 (2019)
139. Zhu, Y., Zhou, W., Chen, Z., et al.: $SrNb_{0.1}Co_{0.7}Fe_{0.2}O_{3-\delta}$ Perovskite as a next-generation electrocatalyst for oxygen evolution in alkaline solution. Angew. Chem. Int. Ed. **54**, 3897–3901 (2015)
140. Goldschmidt, V.M.: Die Gesetze der Krystallochemie. Naturwissenschaften **14**, 477–485 (1926)
141. Bartel, C.J., Sutton, C., Goldsmith, B.R., et al.: New tolerance factor to predict the stability of perovskite oxides and halides. Sci. Adv. **5**, eaav0693 (2019)
142. Švarcová, S., Wiik, K., Tolchard, J., et al.: Structural instability of cubic perovskite $Ba_xSr_{1-x}Co_{1-y}Fe_yO_{3-\delta}$. Solid State Ionics **178**, 1787–1791 (2008)
143. Kruidhof, H., Bouwmeester, H.J.M., Doorn, R.H.E., et al.: Influence of order-disorder transitions on oxygen permeability through selected nonstoichiometric perovskite-type oxides. Solid State Ionics **63–65**, 816–822 (1993)
144. Kashyap, V.K., Jaiswal, S.K., Kumar, J.: Effect of Zr^{4+}on the phase stability and oxygen permeation characteristics of $SrCo_{0.8}Fe_{0.2-y}Zr_yO_{3-\delta}$ ($y \leqslant 0.1$) membranes. Ionics **26**, 1895–1911 (2020)
145. Kubicek, M., Limbeck, A., Frömling, T., et al.: Relationship between cation segregation and the electrochemical oxygen reduction kinetics of $La_{0.6}Sr_{0.4}CoO_{3-\delta}$ thin film electrodes. J. Electrochem. Soc. **158**, B727 (2011)
146. Rupp, G.M., Opitz, A.K., Nenning, A., et al.: Real-time impedance monitoring of oxygen reduction during surface modification of thin film cathodes. Nat. Mater. **16**, 640–645 (2017)
147. Patel, N.K., Utter, R.G., Das, D., et al.: Surface degradation of strontium-based perovskite electrodes of solid oxide fuel cells. J. Power Sources **438**, 227040 (2019)
148. Baqué, L.C., Soldati, A.L., Teixeira-Neto, E., et al.: Degradation of oxygen reduction reaction kinetics in porous $La_{0.6}Sr_{0.4}Co_{0.2}Fe_{0.8}O_{3-\delta}$ cathodes due to aging-induced changes in surface chemistry. J. Power Sources **337**, 166–172 (2017)
149. Yokokawa, H., Tu, H., Iwanschitz, B., et al.: Fundamental mechanisms limiting solid oxide fuel cell durability. J. Power Sources **182**, 400–412 (2008)
150. Konysheva, E., Penkalla, H., Wessel, E., et al.: Chromium poisoning of perovskite cathodes by the ODS alloy $Cr_5Fe_1Y_2O_3$ and the high chromium ferritic steel Crofer22APU. J. Electrochem. Soc. **153**, A765 (2006)
151. Wang, R., Würth, M., Pal, U.B., et al.: Roles of humidity and cathodic current in chromium poisoning of Sr-doped $LaMnO_3$-based cathodes in solid oxide fuel cells. J. Power Sources **360**, 87–97 (2017)
152. Sand, T., Geers, C., Cao, Y., et al.: Effective reduction of chromium-oxy-hydroxide evaporation from Ni-base alloy 690. Oxid. Met. **92**, 259–279 (2019)

153. Bucher, E., Sitte, W., Klauser, F., et al.: Impact of humid atmospheres on oxygen exchange properties, surface-near elemental composition, and surface morphology of $La_{0.6}Sr_{0.4}CoO_{3-\delta}$. Solid State Ionics **208**, 43–51 (2012)
154. Hagen, A., Neufeld, K., Liu, Y.L.: Effect of humidity in air on performance and long-term durability of SOFCs. J. Electrochem. Soc. **157**, B1343 (2010)
155. Nielsen, J., Hagen, A., Liu, Y.L.: Effect of cathode gas humidification on performance and durability of solid oxide fuel cells. Solid State Ionics **181**, 517–524 (2010)
156. Wachsman, E.D., Huang, Y.L., Pellegrinelli, C., et al.: (Invited) towards a fundamental understanding of the cathode degradation mechanisms. ECS Trans. **61**, 47–56 (2014)
157. Huang, Y., Pellegrinelli, C., Wachsman, E.D.: Fundamental impact of humidity on SOFC cathode ORR. J. Electrochem. Soc. **163**, F171–F182 (2015)
158. Huang, Y., Pellegrinelli, C., Wachsman, E.D.: Oxygen dissociation kinetics of concurrent heterogeneous reactions on metal oxides. ACS Catal. **7**, 5766–5772 (2017)
159. Zhang, D., Machala, M.L., Chen, D., et al.: Hydroxylation and cation segregation in $(La_{0.5}Sr_{0.5})FeO_{3-\delta}$ electrodes. Chem. Mater. **32**, 2926–2934 (2020)
160. Liu, R.R., Kim, S.H., Taniguchi, S., et al.: Influence of water vapor on long-term performance and accelerated degradation of solid oxide fuel cell cathodes. J. Power Sources **196**, 7090–7096 (2011)
161. Wang, J., Yang, Z., He, X., et al.: Effect of humidity on $La_{0.4}Sr_{0.6}Co_{0.2}Fe_{0.7}Nb_{0.1}O_{3-\delta}$ cathode of solid oxide fuel cells. Int. J. Hydrogen Energy **44**, 3055–3062 (2019)
162. Hammami, R., Batis, H., Minot, C.: Combined experimental and theoretical investigation of the CO_2 adsorption on $LaMnO_{3+y}$ perovskite oxide. Surf. Sci. **603**, 3057–3067 (2009)
163. Zhou, W., Zhu, Z.: The instability of solid oxide fuel cells in an intermediate temperature region. Asia-Pac. J. Chem. Eng. **6**, 199–203 (2011)
164. Chen, W., Chen, C.S., Winnubst, L.: Ta-doped $SrCo_{0.8}Fe_{0.2}O_{3-\delta}$ membranes: phase stability and oxygen permeation in CO_2 atmosphere. Solid State Ionics **196**, 30–33 (2011)
165. Zhu, Y., Sunarso, J., Zhou, W., et al.: Probing CO_2 reaction mechanisms and effects on the $SrNb_{0.1}Co_{0.9-x}Fe_xO_{3-\delta}$ cathodes for solid oxide fuel cells. Appl. Catal. B **172–173**, 52–57 (2015)
166. Cetin, D., Yu, Y., Luo, H., et al.: Effect of carbon dioxide on the cathodic performance of solid oxide fuel cells. ECS Trans. **61**, 131–137 (2014)
167. Yi, J., Feng, S., Zuo, Y., et al.: Oxygen permeability and stability of $Sr_{0.95}Co_{0.8}Fe_{0.2}O_{3-\delta}$ in a CO_2- and H_2O-containing atmosphere. Chem. Mater. **17**, 5856–5861 (2005)
168. Yáng, Z., Harvey, A.S., Gauckler, L.J.: Influence of CO_2 on $Ba_{0.2}Sr_{0.8}Co_{0.8}Fe_{0.2}O_{3-\delta}$ at elevated temperatures. Scr. Mater. **61**, 1083–1086 (2009)
169. Zhang, Y., Yang, G., Chen, G., et al.: Evaluation of the CO_2 poisoning effect on a highly active cathode $SrSc_{0.175}Nb_{0.025}Co_{0.8}O_{3-\delta}$ in the oxygen reduction reaction. ACS Appl. Mater. Inter. **8**, 3003–3011 (2016)
170. Stern, K.H., Weise, E.L.: High Temperature Properties and Decomposition of Inorganic Salts Part 1, Sulfates. pp. 1–38. U. S. Department of Commerce, United States (1966)
171. Lancashire, R.J.: Lecture 3. Polarizability (2015). http://wwwchem.uwimona.edu.jm/courses/CHEM1902/IC10K_MG_Fajans.html. Accessed 30 July 2020
172. Stern, K.H.: High temperature properties and decomposition of inorganic salts part 3, nitrates and nitrites. J. Phys. Chem. Ref. Data **1**, 747–772 (1972)
173. Li, K., Zhao, H., Lu, Y., et al.: High CO_2 tolerance oxygen permeation membranes $BaFe_{0.95-x}Ca_{0.05}Ti_xO_{3-\delta}$. J. Membr. Sci. **550**, 302–312 (2018)
174. Li, J., Hou, J., Lu, Y., et al.: Ca-containing $Ba_{0.95}Ca_{0.05}Co_{0.4}Fe_{0.4}Zr_{0.1}O_{3-\delta}$ cathode with high CO_2-poisoning tolerance for proton-conducting solid oxide fuel cells. J. Power Sources **453**, 227909 (2020)
175. Choi, S., Park, S., Shin, J., et al.: The effect of calcium doping on the improvement of performance and durability in a layered perovskite cathode for intermediate-temperature solid oxide fuel cells. J. Mater. Chem. A **3**, 6088–6095 (2015)
176. Chen, G., Widenmeyer, M., Tang, B., et al.: A CO and CO_2 tolerating $(La_{0.9}Ca_{0.1})_2(Ni_{0.75}Cu_{0.25})O_{4+\delta}$ Ruddlesden–Popper membrane for oxygen separation. Front. Chem. Sci. Eng. **14**, 405–414 (2020)
177. Yi, J., Schroeder, M., Martin, M.: CO_2-tolerant and cobalt-free $SrFe_{0.8}Nb_{0.2}O_{3-\delta}$ perovskite membrane for oxygen separation. Chem. Mater. **25**, 815–817 (2013)
178. Yi, J., Brendt, J., Schroeder, M., et al.: Oxygen permeation and oxidation states of transition metals in (Fe, Nb)-doped $BaCoO_{3-\delta}$ perovskites. J. Membr. Sci. **387–388**, 17–23 (2012)
179. Meng, Y., Sun, L., Gao, J., et al.: Insights into the CO_2 stability-performance trade-off of antimony-doped $SrFeO_{3-\delta}$ perovskite cathode for solid oxide fuel cells. ACS Appl. Mater. Inter. **11**, 11498–11506 (2019)
180. Zhang, J., Li, X., Zhang, Z., et al.: A new highly active and CO_2-stable perovskite-type cathode material for solid oxide fuel cells developed from A- and B-site cation synergy. J. Power Sources **457**, 227995 (2020)
181. Zhang, Y., Gao, X., Sunarso, J., et al.: Significantly Improving the durability of single-chamber solid oxide fuel cells: a highly active CO_2-resistant perovskite cathode. ACS Appl. Energy Mater. **1**, 1337–1343 (2018)
182. Zhu, J., Guo, S., Chu, Z., et al.: CO_2-tolerant oxygen-permeable perovskite-type membranes with high permeability. J. Mater. Chem. A **3**, 22564–22573 (2015)
183. Park, J.H., Kim, K.Y., Park, S.D.: Oxygen permeation and stability of $La_{0.6}Sr_{0.4}Ti_xFe_{1-x}O_{3-\delta}$ ($x = 0.2$ and 0.3) membrane. Desalination **245**, 559–569 (2009)
184. Zhang, Z., Chen, D., Dong, F., et al.: Understanding the doping effect toward the design of CO_2-tolerant perovskite membranes with enhanced oxygen permeability. J. Membr. Sci. **519**, 11–21 (2016)
185. Slater, J.C.: Atomic shielding constants. Phys. Rev. **36**, 57–64 (1930)
186. Sammells, A.F., Cook, R.L., White, J.H., et al.: Rational selection of advanced solid electrolytes for intermediate temperature fuel cells. Solid State Ionics **52**, 111–123 (1992)
187. Daio, T., Mitra, P., Lyth, S.M., et al.: Atomic-resolution analysis of degradation phenomena in SOFCS: a case study of SO_2 poisoning in LSM cathodes. Int. J. Hydrogen Energy **41**, 12214–12221 (2016)
188. Berger, C., Bucher, E., Gspan, C., et al.: Long-term stability of oxygen surface exchange kinetics of $Pr_{0.8}Ca_{0.2}FeO_{3-\delta}$ against SO_2-poisoning. Solid State Ionics **326**, 82–89 (2018)
189. Wang, F., Yamaji, K., Cho, D.H., et al.: Sulfur poisoning on $La_{0.6}Sr_{0.4}Co_{0.2}Fe_{0.8}O_3$ Cathode for SOFCs. J. Electrochem. Soc. **158**, B1391 (2011)
190. Wang, F., Yamaji, K., Cho, D.H., et al.: Effect of strontium concentration on sulfur poisoning of LSCF cathodes. Solid State Ionics **225**, 157–160 (2012)
191. De Vero, J.C., Yokokawa, H., Develos-Bagarinao, K., et al.: Influence of electrolyte substrates on the Sr-segregation and $SrSO_4$ formation in $La_{0.6}Sr_{0.4}Co_{0.2}Fe_{0.8}O_{3-\delta}$ thin films. MRS Commun. **9**, 236–244 (2019)
192. Kishimoto, H., Sakai, N., Horita, T., et al.: Cation transport behavior in SOFC cathode materials of $La_{0.8}Sr_{0.2}CoO_3$ and $La_{0.8}Sr_{0.2}FeO_3$ with perovskite structure. Solid State Ionics **178**, 1317–1325 (2007)

193. Eguchi, K., Akasaka, N., Mitsuyasu, H., et al.: Process of solid state reaction between doped ceria and zirconia. Solid State Ionics **135**, 589–594 (2000)
194. Horita, T., Yamaji, K., Sakai, N., et al.: Stability at $La_{0.6}Sr_{0.4}CoO_{3-d}$cathode/$La_{0.8}Sr_{0.2}Ga_{0.8}Mg_{0.2}O_{2.8}$ electrolyte interface under current flow for solid oxide fuel cells. Solid State Ionics **133**, 143–152 (2000)
195. Tsoga, A., Gupta, A., Naoumidis, A., et al.: Gadolinia-doped ceria and yttria stabilized zirconia interfaces: regarding their application for SOFC technology. Acta Mater. **48**, 4709–4714 (2000)
196. Gindorf, C., Singheiser, L., Hilpert, K.: Vaporisation of chromia in humid air. J. Phys. Chem. Solids **66**, 384–387 (2005)
197. Jiang, S.P., Chen, X.: Chromium deposition and poisoning of cathodes of solid oxide fuel cells: a review. Int. J. Hydrogen Energy **39**, 505–531 (2014)
198. Jiang, S.P., Zhang, J.P., Zheng, X.G.: A comparative investigation of chromium deposition at air electrodes of solid oxide fuel cells. J. Eur. Ceram. Soc. **22**, 361–373 (2002)
199. Yang, Z., Guo, M., Wang, N., et al.: A short review of cathode poisoning and corrosion in solid oxide fuel cell. Int. J. Hydrogen Energy **42**, 24948–24959 (2017)
200. Fergus, J.W.: Sealants for solid oxide fuel cells. J. Power Sources **147**, 46–57 (2005)
201. Stanislowski, M., Wessel, E., Hilpert, K., et al.: Chromium vaporization from high-temperature alloys. J. Electrochem. Soc. **154**, A295 (2007)
202. Schuler, J.A., Wuillemin, Z., Hessler-Wyser, A.C., et al.: Glass-forming exogenous silicon contamination in solid oxide fuel cell cathodes. Electrochem. Solid-State Lett. **14**, B20 (2011)
203. Jacobson, N.S., Opila, E.J., Myers, D.L., et al.: Thermodynamics of gas phase species in the Si-O-H system. J. Chem. Thermodyn. **37**, 1130–1137 (2005)
204. Perz, M., Bucher, E., Gspan, C., et al.: Long-term degradation of $La_{0.6}Sr_{0.4}Co_{0.2}Fe_{0.8}O_{3-\delta}$ IT-SOFC cathodes due to silicon poisoning. Solid State Ionics **288**, 22–27 (2016)
205. Schrödl, N., Bucher, E., Gspan, C., et al.: Phase decomposition in the chromium- and silicon-poisoned IT-SOFC cathode materials $La_{0.6}Sr_{0.4}CoO_{3-\delta}$ and $La_2NiO_{4+\delta}$. Solid State Ionics **288**, 14–21 (2016)
206. Bucher, E., Gspan, C., Höschen, T., et al.: Oxygen exchange kinetics of $La_{0.6}Sr_{0.4}CoO_{3-\delta}$ affected by changes of the surface composition due to chromium and silicon poisoning. Solid State Ionics **299**, 26–31 (2017)
207. Schrödl, N., Bucher, E., Egger, A., et al.: Long-term stability of the IT-SOFC cathode materials $La_{0.6}Sr_{0.4}CoO_{3-\delta}$ and $La_2NiO_{4+\delta}$ against combined chromium and silicon poisoning. Solid State Ionics **276**, 62–71 (2015)
208. Sohn, S.B., Choi, S.Y., Kim, G.H., et al.: Suitable glass-ceramic sealant for planar solid-oxide fuel cells. J. Am. Ceram. Soc. **87**, 254–260 (2004)
209. Sohn, S.B., Choi, S.Y., Kim, G.H., et al.: Stable sealing glass for planar solid oxide fuel cell. J. Non-Cryst. Solids **297**, 103–112 (2002)
210. Marzouk, S.Y.: The acoustic properties of borosilicate glass affected by oxide of rare earth gadolinium. Phys. B **405**, 3395–3400 (2010)
211. Snyder, M.J., Mesko, M.G., Shelby, J.E.: Volatilization of boron from E-glass melts. J. Non-Cryst. Solids **352**, 669–673 (2006)
212. Zhang, T., Fahrenholtz, W.G., Reis, S.T., et al.: Borate Volatility from SOFC sealing glasses. J. Am. Ceram. Soc. **91**, 2564–2569 (2008)
213. Chen, K., Ai, N., Zhao, L., et al.: Effect of volatile boron species on the electrocatalytic activity of cathodes of solid oxide fuel cells. J. Electrochem. Soc. **160**, F183–F190 (2012)
214. Chen, K., Ai, N., Zhao, L., et al.: Effect of volatile boron species on the electrocatalytic activity of cathodes of solid oxide fuel cells. J. Electrochem. Soc. **160**, F301–F308 (2013)
215. Chen, K., Hyodo, J., O'Donnell, K.M., et al.: Effect of volatile boron species on the electrocatalytic activity of cathodes of solid oxide fuel cells. J. Electrochem. Soc. **161**, F1163–F1170 (2014)
216. Chen, K., Ai, N., Lievens, C., et al.: Impact of volatile boron species on the microstructure and performance of nano-structured (Gd, Ce)O_2 infiltrated (La, Sr)MnO_3 cathodes of solid oxide fuel cells. Electrochem. Commun. **23**, 129–132 (2012)
217. Dimesso, L.: Pechini processes: an alternate approach of the sol-gel method, preparation, properties, and applications. In: Klein, L., Aparicio, M., Jitianu, A. (eds.) Handbook of Sol-Gel Science and Technology, pp. 1–22. Springer, Cham (2016)
218. Athayde, D.D., Souza, D.F., Silva, A.M.A., et al.: Review of perovskite ceramic synthesis and membrane preparation methods. Ceram. Int. **42**, 6555–6571 (2016)
219. Babindamana, D., Jia, C., Han, M.: Study of a promising co-doped double perovskite cathode material for IT-SOFCs. ECS Trans. **91**, 1437–1443 (2019)
220. Kumar, P., Presto, S., Sinha, A.S.K., et al.: Effect of samarium (Sm^{3+}) doping on structure and electrical conductivity of double perovskite Sr_2NiMoO_6 as anode material for SOFC. J. Alloys Compd. **725**, 1123–1129 (2017)
221. Niu, Y., Zhou, W., Sunarso, J., et al.: A single-step synthesized cobalt-free barium ferrites-based composite cathode for intermediate temperature solid oxide fuel cells. Electrochem. Commun. **13**, 1340–1343 (2011)
222. Gędziorowski, B., Świerczek, K., Molenda, J.: $La_{1-x}Ba_xCo_{0.2}Fe_{0.8}O_{3-\delta}$ perovskites for application in intermediate temperature SOFCs. Solid State Ionics **225**, 437–442 (2012)
223. Yoo, S., Jun, A., Ju, Y.W., et al.: Development of double-perovskite compounds as cathode materials for low-temperature solid oxide fuel cells. Angew. Chem. Int. Ed. **53**, 13064–13067 (2014)
224. Pang, S., Xu, J., Su, Y., et al.: The role of A-site cation size mismatch in tune the catalytic activity and durability of double perovskite oxides. Appl. Catal. B **270**, 118868 (2020)
225. Li, M., Zhou, W., Zhu, Z.: Recent development on perovskite-type cathode materials based on $SrCoO_{3-\delta}$ parent oxide for intermediate-temperature solid oxide fuel cells. Asia-Pac. J. Chem. Eng. **11**, 370–381 (2016)
226. Celikbilek, O., Thieu, C.A., Agnese, F., et al.: Enhanced catalytic activity of nanostructured, A-site deficient $(La_{0.7}Sr_{0.3})095(Co_{0.2}Fe_{0.8})O_{3-\delta}$ for SOFC cathodes. J. Mater. Chem. A **7**, 25102–25111 (2019)
227. Zhu, Y., Zhou, W., Ran, R., et al.: Promotion of oxygen reduction by exsolved silver nanoparticles on a perovskite scaffold for low-temperature solid oxide fuel cells. Nano Lett. **16**, 512–518 (2016)
228. Sažinas, R., Andersen, K.B., Simonsen, S.B., et al.: Silver modified cathodes for solid oxide fuel cells. J. Electrochem. Soc. **166**, F79–F88 (2019)
229. Chen, Y., Yoo, S., Choi, Y., et al.: A highly active, CO_2-tolerant electrode for the oxygen reduction reaction. Eng. Environ. Sci. **11**, 2458–2466 (2018)
230. Xing, L., Xia, T., Li, Q., et al.: High-performance and CO_2-durable composite cathodes toward electrocatalytic oxygen reduction: $Ce_{0.8}Sm_{0.2}O_{1.9}$ nanoparticle-decorated double perovskite $EuBa_{0.5}Sr_{0.5}Co_2O_{5+\delta}$. ACS Sustain. Chem. Eng. **7**, 17907–17918 (2019)
231. Subardi, A., Liao, K.Y., Fu, Y.P.: Oxygen transport, thermal and electrochemical properties of $NdBa_{0.5}Sr_{0.5}Co_2O_{5+\delta}$ cathode for SOFCs. J. Eur. Ceram. Soc. **39**, 30–40 (2019)
232. Yang, H., Gu, Y., Zhang, Y., et al.: Sr-substituted $SmBa_{0.75}Ca_{0.25}CoFeO_{5+\delta}$ as a cathode for intermediate-temperature solid oxide fuel cells. J. Alloys Compd. **770**, 616–624 (2019)

233. Wang, S., Meng, X., Yang, J., et al.: Performance assessment of $Pr_{1-x}Sr_xCo_{0.8}Cu_{0.2}O_{3-\delta}$ perovskite oxides as cathode material for solid oxide fuel cells with $Ce_{0.8}Sm_{0.2}O_{1.9}$ electrolyte. J. Mater. Sci.: Mater. Electron. **30**, 5881–5890 (2019)
234. Pang, S., Wang, W., Chen, T., et al.: The effect of potassium on the properties of $PrBa_{1-x}Co_2O_{5+\delta}$ ($x = 0.00$–0.10) cathodes for intermediate-temperature solid oxide fuel cells. Int. J. Hydrogen Energy **41**, 13705–13714 (2016)
235. Liu, X., Dong, W., Tong, Y., et al.: Li effects on layer-structured oxide $Li_xNi_{0.8}Co_{0.15}Al_{0.05}O_{2-\delta}$: improving cell performance via on-line reaction. Electrochim. Acta **295**, 325–332 (2019)
236. Choi, S., Sengodan, S., Park, S., et al.: A robust symmetrical electrode with layered perovskite structure for direct hydrocarbon solid oxide fuel cells: $PrBa_{0.8}Ca_{0.2}Mn_2O_{5+\delta}$. J. Mater. Chem. A **4**, 1747–1753 (2016)
237. Zhang, Y., Zhao, H., Du, Z., et al.: High-performance $SmBaMn_2O_{5+\delta}$ electrode for symmetrical solid oxide fuel cell. Chem. Mater. **31**, 3784–3793 (2019)
238. Dong, F., Chen, Y., Chen, D., et al.: Surprisingly high activity for oxygen reduction reaction of selected oxides lacking long oxygen-ion diffusion paths at intermediate temperatures: a case study of cobalt-free $BaFeO_{3-\delta}$. ACS Appl. Mater. Intern. **6**, 11180–11189 (2014)
239. Ren, R., Wang, Z., Meng, X., et al.: Boosting the electrochemical performance of Fe-based layered double perovskite cathodes by Zn^{2+} doping for solid oxide fuel cells. ACS Appl. Mater. Inter. **12**, 23959–23967 (2020)
240. Zhou, W., Ran, R., Shao, Z.: Progress in understanding and development of $Ba_{0.5}Sr_{0.5}Co_{0.8}Fe_{0.2}O_{3-\delta}$-based cathodes for intermediate-temperature solid-oxide fuel cells: a review. J. Power Sources **192**, 231–246 (2009)
241. Matar, S.F., Campet, G., Subramanian, M.A.: Electronic properties of oxides: chemical and theoretical approaches. Prog. Solid State Chem. **39**, 70–95 (2011)
242. Shimada, H., Yamaguchi, T., Sumi, H., et al.: Extremely fine structured cathode for solid oxide fuel cells using Sr-doped $LaMnO_3$ and Y_2O_3-stabilized ZrO_2 nano-composite powder synthesized by spray pyrolysis. J. Power Sources **341**, 280–284 (2017)
243. Shen, J., Yang, G., Zhang, Z., et al.: Tuning layer-structured $La_{0.6}Sr_{1.4}MnO_{4+\delta}$ into a promising electrode for intermediate-temperature symmetrical solid oxide fuel cells through surface modification. J. Mater. Chem. A **4**, 10641–10649 (2016)
244. Chen, C., Baiyee, Z.M., Ciucci, F.: Unraveling the effect of La A-site substitution on oxygen ion diffusion and oxygen catalysis in perovskite $BaFeO_3$ by data-mining molecular dynamics and density functional theory. Phys. Chem. Chem. Phys. **17**, 24011–24019 (2015)
245. Rehman, S.U., Shaur, A., Song, R.H., et al.: Nano-fabrication of a high-performance $LaNiO_3$ cathode for solid oxide fuel cells using an electrochemical route. J. Power Sources **429**, 97–104 (2019)
246. Rehman, S.U., Song, R.H., Lim, T.H., et al.: High-performance nanofibrous $LaCoO_3$ perovskite cathode for solid oxide fuel cells fabricated via chemically assisted electrodeposition. J. Mater. Chem. A **6**, 6987–6996 (2018)
247. Fu, D., Jin, F., He, T.: A-site calcium-doped $Pr_{1-x}Ca_xBaCo_2O_{5+\delta}$ double perovskites as cathodes for intermediate-temperature solid oxide fuel cells. J. Power Sources **313**, 134–141 (2016)
248. Ling, Y., Lu, X., Niu, J., et al.: Antimony doped barium strontium ferrite perovskites as novel cathodes for intermediate-temperature solid oxide fuel cells. J. Alloys Compd. **666**, 23–29 (2016)
249. Chan, J.Y., Zhang, K., Zhang, C., et al.: Novel tungsten stabilizing $SrCo_{1-x}W_xO_{3-\delta}$ membranes for oxygen production. Ceram. Int. **41**, 14935–14940 (2015)
250. Aguadero, A., Pérez-Coll, D., Alonso, J.A., et al.: A new family of Mo-doped $SrCoO_{3-\delta}$ perovskites for application in reversible solid state electrochemical cells. Chem. Mater. **24**, 2655–2663 (2012)
251. Aguadero, A., Alonso, J.A., Pérez-Coll, D., et al.: $SrCo_{0.95}Sb_{0.05}O_{3-\delta}$ as cathode material for high power density solid oxide fuel cells. Chem. Mater. **22**, 789–798 (2010)
252. Cascos, V., Martínez-Coronado, R., Alonso, J.A.: New Nb-doped $SrCo_{1-x}Nb_xO_{3-\delta}$ perovskites performing as cathodes in solid-oxide fuel cells. Int. J. Hydrogen Energy **39**, 14349–14354 (2014)
253. Fernández-Ropero, A.J., Porras-Vázquez, J.M., Cabeza, A., et al.: High valence transition metal doped strontium ferrites for electrode materials in symmetrical SOFCs. J. Power Sources **249**, 405–413 (2014)
254. Pauling, L.: The principles determining the structure of complex ionic crystals. J. Am. Chem. Soc. **51**, 1010–1026 (1929)
255. Nagai, T., Ito, W., Sakon, T.: Relationship between cation substitution and stability of perovskite structure in $SrCoO_{3-\delta}$-based mixed conductors. Solid State Ionics **177**, 3433–3444 (2007)
256. Li, Z., Lv, L., Wang, J., et al.: Engineering phosphorus-doped $LaFeO_{3-\delta}$ perovskite oxide as robust bifunctional oxygen electrocatalysts in alkaline solutions. Nano Energy **47**, 199–209 (2018)
257. Jarvis, A., Berry, F.J., Marco, J.F., et al.: Introduction of sulfate to stabilize the $n = 3$ Ruddlesden–Popper system $Sr_4Fe_3O_{10-\delta}$, as a potential SOFC cathode. ECS Trans. **91**, 1467–1476 (2019)
258. Liu, Y., Zhu, X., Yang, W.: Stability of sulfate doped $SrCoO_{3-\delta}$ MIEC membrane. J. Membr. Sci. **501**, 53–59 (2016)
259. Porras-Vazquez, J.M., Slater, P.R.: Synthesis and characterization of oxyanion-doped cobalt containing perovskites. Fuel Cells **12**, 1056–1063 (2012)
260. Xu, M., Wang, W., Liu, Y., et al.: An intrinsically conductive Phosphorus-Doped perovskite oxide as a new cathode for high-performance dye-sensitized solar cells by providing internal conducting pathways. Solar RRL **3**, 1900108 (2019)
261. Luo, Y., Zheng, Y., Feng, X., et al.: Controllable P doping of the $LaCoO_3$ catalyst for efficient propane oxidation: optimized surface Co distribution and enhanced oxygen vacancies. ACS Appl. Mater. Inter. **12**, 23789–23799 (2020)
262. Zhao, L., Cheng, Y., Jiang, S.P.: A new, high electrochemical activity and chromium tolerant cathode for solid oxide fuel cells. Int. J. Hydrogen Energy **40**, 15622–15631 (2015)
263. Porras-Vazquez, J.M., Smith, R.I., Slater, P.R.: Investigation into the effect of Si doping on the cell symmetry and performance of $Sr_{1-y}Ca_yFeO_{3-\delta}$ SOFC cathode materials. J. Solid State Chem. **213**, 132–137 (2014)
264. Gao, J., Li, Q., Xia, W., et al.: Advanced electrochemical performance and CO_2 tolerance of $Bi_{0.5}Sr_{0.5}Fe_{1-x}Ti_xO_{3-\delta}$ perovskite materials as oxygen reduction cathodes for intermediate-temperature solid oxide fuel cells. ACS Sustain. Chem. Eng. **7**, 18647–18656 (2019)
265. Jang, I., Lee, H., Tamarany, R., et al.: Tailoring the ratio of A-site cations in $Pr_{1-x}Nd_xBaCo_{1.6}Fe_{0.4}O_{5+\delta}$ to promote the higher oxygen reduction reaction activity for low-temperature solid oxide fuel cells. Chem. Mater. **32**, 3841–3849 (2020)
266. Zeng, P., Ran, R., Chen, Z., et al.: Efficient stabilization of cubic perovskite $SrCoO_{3-\delta}$ by B-site low concentration scandium doping combined with sol-gel synthesis. J. Alloys Compd. **455**, 465–470 (2008)
267. Zeng, Q., Zhang, X., Wang, W., et al.: A Zn-doped $Ba_{0.5}Sr_{0.5}Co_{0.8}Fe_{0.2}O_{3-\delta}$ perovskite cathode with enhanced ORR catalytic activity for SOFCs. Catalysts **10**, 12 (2020)
268. Park, B.K., Barnett, S.A.: Boosting solid oxide fuel cell performance via electrolyte thickness reduction and cathode infiltration. J. Mater. Chem. A **8**, 11626–11631 (2020)

269. Yang, T., Wen, Y., Wu, T., et al.: A highly active and Cr-resistant infiltrated cathode for practical solid oxide fuel cells. J. Mater. Chem. A **8**, 82–86 (2020)
270. Zhou, W., Liang, F., Shao, Z., et al.: Hierarchical CO_2-protective shell for highly efficient oxygen reduction reaction. Sci. Rep. **2**, 327 (2012)
271. Shaur, A., Rehman, S.U., Kim, H.S., et al.: Hybrid electrochemical deposition route for the facile nanofabrication of a Cr-poisoning-tolerant La(Ni, Fe)$O_{3-\delta}$ cathode for solid oxide fuel cells. ACS Appl. Mater. Inter. **12**, 5730–5738 (2020)
272. Zhou, W., Ge, L., Chen, Z.G., et al.: Amorphous iron oxide decorated 3D heterostructured electrode for highly efficient oxygen reduction. Chem. Mater. **23**, 4193–4198 (2011)
273. Gong, Y., Patel, R.L., Liang, X., et al.: Atomic Layer Deposition Functionalized Composite SOFC Cathode $La_{0.6}Sr_{0.4}Fe_{0.8}Co_{0.2}O_{3-\delta}$-$Gd_{0.2}Ce_{0.8}O_{1.9}$: enhanced long-term stability. Chem. Mater. **25**, 4224–4231 (2013)
274. Gong, Y., Palacio, D., Song, X., et al.: Stabilizing nanostructured solid oxide fuel cell cathode with atomic layer deposition. Nano Lett. **13**, 4340–4345 (2013)
275. Choi, H.J., Bae, K., Grieshammer, S., et al.: Surface tuning of solid oxide fuel cell cathode by atomic layer deposition. Adv. Energy Mater. **8**, 1802506 (2018)
276. Chen, Y., Gerdes, K., Song, X.: Nanoionics and nanocatalysts: conformal mesoporous surface scaffold for cathode of solid oxide fuel cells. Sci. Rep. **6**, 32997 (2016)
277. Zhang, Y., Wen, Y., Huang, K., et al.: Atomic layer deposited zirconia overcoats as on-board strontium getters for improved solid oxide fuel cell nanocomposite cathode durability. ACS Appl. Energy Mater. **3**, 4057–4067 (2020)
278. Zheng, Y., Li, Y., Wu, T., et al.: Controlling crystal orientation in multilayered heterostructures toward high electro-catalytic activity for oxygen reduction reaction. Nano Energy **62**, 521–529 (2019)
279. Ma, W., Kim, J.J., Tsvetkov, N., et al.: Vertically aligned nanocomposite $La_{0.8}Sr_{0.2}CoO_3$/$(La_{0.5}Sr_{0.5})_2CoO_4$ cathodes—electronic structure, surface chemistry and oxygen reduction kinetics. J. Mater. Chem. A **3**, 207–219 (2015)
280. Lee, Y.H., Ren, H., Wu, E.A., et al.: All-sputtered, superior power density thin-film solid oxide fuel cells with a novel nanofibrous ceramic cathode. Nano Lett. **20**, 2943–2949 (2020)
281. Yun, S.S., Jo, K., Ryu, J., et al.: Surface modification and electrochemical properties of cobalt-based layered perovskite cathodes for intermediate-temperature solid oxide fuel cells. Solid State Ionics **347**, 115268 (2020)
282. Ding, D., Li, X., Lai, S.Y., et al.: Enhancing SOFC cathode performance by surface modification through infiltration. Eng. Environ. Sci. **7**, 552–575 (2014)
283. Jiang, S.P.: A review of wet impregnation-An alternative method for the fabrication of high performance and nano-structured electrodes of solid oxide fuel cells. Mater. Sci. Eng. A **418**, 199–210 (2006)
284. Vohs, J.M., Gorte, R.J.: High-performance SOFC cathodes prepared by infiltration. Adv. Mater. **21**, 943–956 (2009)
285. Jiang, Z., Xia, C., Chen, F.: Nano-structured composite cathodes for intermediate-temperature solid oxide fuel cells via an infiltration/impregnation technique. Electrochim. Acta **55**, 3595–3605 (2010)
286. Nicollet, C., Flura, A., Vibhu, V., et al.: An innovative efficient oxygen electrode for SOFC: Pr_6O_{11} infiltrated into Gd-doped ceria backbone. Int. J. Hydrogen Energy **41**, 15538–15544 (2016)
287. Lee, S., Miller, N., Staruch, M., et al.: $Pr_{0.6}Sr_{0.4}CoO_{3-\delta}$ electrocatalyst for solid oxide fuel cell cathode introduced via infiltration. Electrochim. Acta **56**, 9904–9909 (2011)
288. Zhang, X., Liu, L., Zhao, Z., et al.: High performance solid oxide fuel cells with $Co_{1.5}Mn_{1.5}O_4$ infiltrated (La, Sr)MnO_3-yittria stabilized zirconia cathodes. Int. J. Hydrogen Energy **40**, 3332–3337 (2015)
289. Basu, R.N., Tietz, F., Wessel, E., et al.: Interface reactions during co-firing of solid oxide fuel cell components. J. Mater. Process. Technol. **147**, 85–89 (2004)
290. Bevilacqua, M., Montini, T., Tavagnacco, C., et al.: Preparation, characterization, and electrochemical properties of pure and composite $LaNi_{0.6}Fe_{0.4}O_3$-based cathodes for IT-SOFC. Chem. Mater. **19**, 5926–5936 (2007)
291. Schmauss, T.A., Railsback, J.G., Lu, M.Y., et al.: ZrO_2 atomic layer deposition into $Sr_{0.5}Sm_{0.5}CoO_{3-\delta}$-$Ce_{0.9}Gd_{0.1}O_{2-\delta}$ solid oxide fuel cell cathodes: mechanisms of stability enhancement. J. Mater. Chem. A **7**, 27585–27593 (2019)
292. Matsuda, J., Kanae, S., Kawabata, T., et al.: TEM and ETEM study on $SrZrO_3$ formation at the LSCF/GDC/YSZ interfaces. ECS Trans. **78**, 993–1001 (2017)
293. Ai, N., Chen, K., Jiang, S.P.: A $La_{0.8}Sr_{0.2}MnO_3$/$La_{0.6}Sr_{0.4}Co_{0.2}Fe_{0.8}O_{3-\delta}$ core-shell structured cathode by a rapid sintering process for solid oxide fuel cells. Int. J. Hydrogen Energy **42**, 7246–7251 (2017)
294. Bishop, C.A.: 19-atomic layer deposition. In: Bishop, C.A. (ed.) Vacuum Deposition onto Webs, Films and Foils, 2nd edn., pp. 331–336. William Andrew Publishing, Oxford (2011)
295. Chen, Y., Hinerman, A., Liang, L., et al.: Conformal coating of cobalt oxide on solid oxide fuel cell cathode and resultant continuously increased oxygen reduction reaction kinetics upon operation. J. Power Sources **405**, 45–50 (2018)
296. Rahmanipour, M., Cheng, Y., Onn, T.M., et al.: Modification of LSF-YSZ composite cathodes by atomic layer deposition. J. Electrochem. Soc. **164**, F879–F884 (2017)
297. Choi, H.J., Bae, K., Jang, D.Y., et al.: Performance degradation of lanthanum strontium cobaltite after surface modification. J. Electrochem. Soc. **162**, F622–F626 (2015)
298. Yu, A.S., Küngas, R., Vohs, J.M., et al.: Modification of SOFC cathodes by atomic layer deposition. J. Electrochem. Soc. **160**, F1225–F1231 (2013)
299. Paige, J.M., Cheng, Y., Pepin, P.A., et al.: Surface modification of SOFC cathodes by Co, Ni, and Pd oxides. Solid State Ionics **341**, 115051 (2019)
300. Küngas, R., Yu, A.S., Levine, J., et al.: An investigation of oxygen reduction kinetics in LSF electrodes. J. Electrochem. Soc. **160**, F205–F211 (2012)
301. Sumi, H., Ohshiro, T., Nakayama, M., et al.: Prevention of reaction between (Ba, Sr)(Co, Fe)O_3 cathodes and yttria-stabilized zirconica electrolytes for intermediate-temperature solid oxide fuel cells. Electrochim. Acta **184**, 403–409 (2015)
302. Martín-Palma, R.J., Lakhtakia, A.: Chapter 15—vapor-deposition techniques. In: Lakhtakia, A., Martín-Palma, R.J. (eds.) Engineered Biomimicry, pp. 383–398. Elsevier, Boston (2013)
303. Fujioka, H.: 8-pulsed laser deposition (PLD). In: Kuech, T.F. (ed.) Handbook of Crystal Growth, 2nd edn., pp. 365–397. North-Holland, Boston (2015)
304. Mukherjee, K., Hayamizu, Y., Kim, C.S., et al.: Praseodymium cuprate thin film cathodes for intermediate temperature solid oxide fuel cells: roles of doping, orientation, and crystal structure. ACS Appl. Mater. Interfaces **8**, 34295–34302 (2016)
305. Zhu, Z., Zhou, C., Zhou, W., et al.: Textured $Sr_2Sc_{0.1}Nb_{0.1}Co_{1.5}Fe_{0.3}O_{6-2\delta}$ thin film cathodes for IT-SOFCs. Materials **12**, 777 (2019)
306. Chen, Y., Cai, Z., Kuru, Y., et al.: Electronic activation of cathode superlattices at elevated temperatures: source of markedly accelerated oxygen reduction kinetics. Adv. Energy Mater. **3**, 1221–1229 (2013)
307. Feng, Z., Yacoby, Y., Gadre, M.J., et al.: Anomalous interface and surface strontium segregation in $(La_{1-y}Sr_y)_2CoO_{4\pm\delta}$/

$La_{1-x}Sr_xCoO_{3-\delta}$ heterostructured thin films. J. Phys. Chem. Lett. **5**, 1027–1034 (2014)
308. Stämmler, S., Merkle, R., Stuhlhofer, B., et al.: Phase constitution, Sr distribution and morphology of self-assembled La–Sr–Co–O composite films prepared by PLD. Solid State Ionics **303**, 172–180 (2017)
309. Develos-Bagarinao, K., Budiman, R.A., Liu, S.S., et al.: Evolution of cathode-interlayer interfaces and its effect on long-term degradation. J. Power Sources **453**, 227894 (2020)
310. Choi, H.J., Kim, M., Neoh, K.C., et al.: High-performance silver cathode surface treated with scandia-stabilized zirconia nanoparticles for intermediate temperature solid oxide fuel cells. Adv. Energy Mater. **7**, 1601956 (2017)

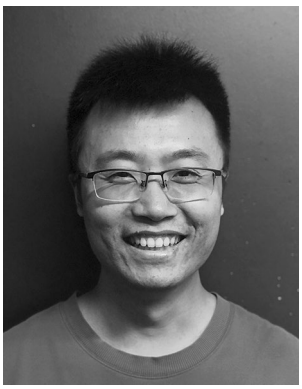

Zhiheng Li Zhiheng Li is pursuing his Ph.D. degree at the China University of Petroleum. He is currently working at the University of Queensland as a visiting student. His research interest mainly focuses on energy conversion related materials and systems such as bio-oil production, deep eutectic solvents and perovskite cathodes for solid oxide fuel cells.

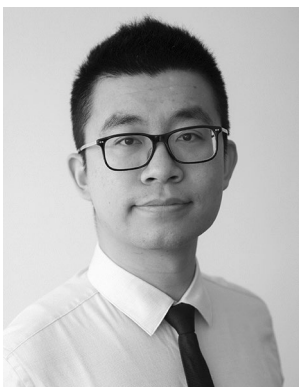

Dr Mengran Li is a postdoctoral research fellow in the School of Chemical Engineering and UQ-HBIS Innovation Centre for Sustainable Steel at the University of Queensland, Australia. Mengran completed his Bachelor of Engineering in chemical engineering at Tianjin University, China (2008), and Ph.D. from the University of Queensland in Australia (2012). His current research focuses on the development of electrode materials and electrochemical process for energy conversion and carbon mitigation.

Prof. Zhonghua Zhu is a Professor in the School of Chemical Engineering, at the University of Queensland (UQ). He received his Ph.D. in chemical engineering, from UQ in 2002 and then worked as a Lecturer at Curtin University of Technology from 2002 to 2004. He moved back to UQ at the end of 2004 and has been working in the same school until now. His research interests and expertise are advanced catalysis, gas/liquid and separation, direct carbon fuel cells, and solid-oxide fuel cells with strong application focus on clean energy and environment.